STUDIA UNIVERSITATIS
BABEŞ-BOLYAI

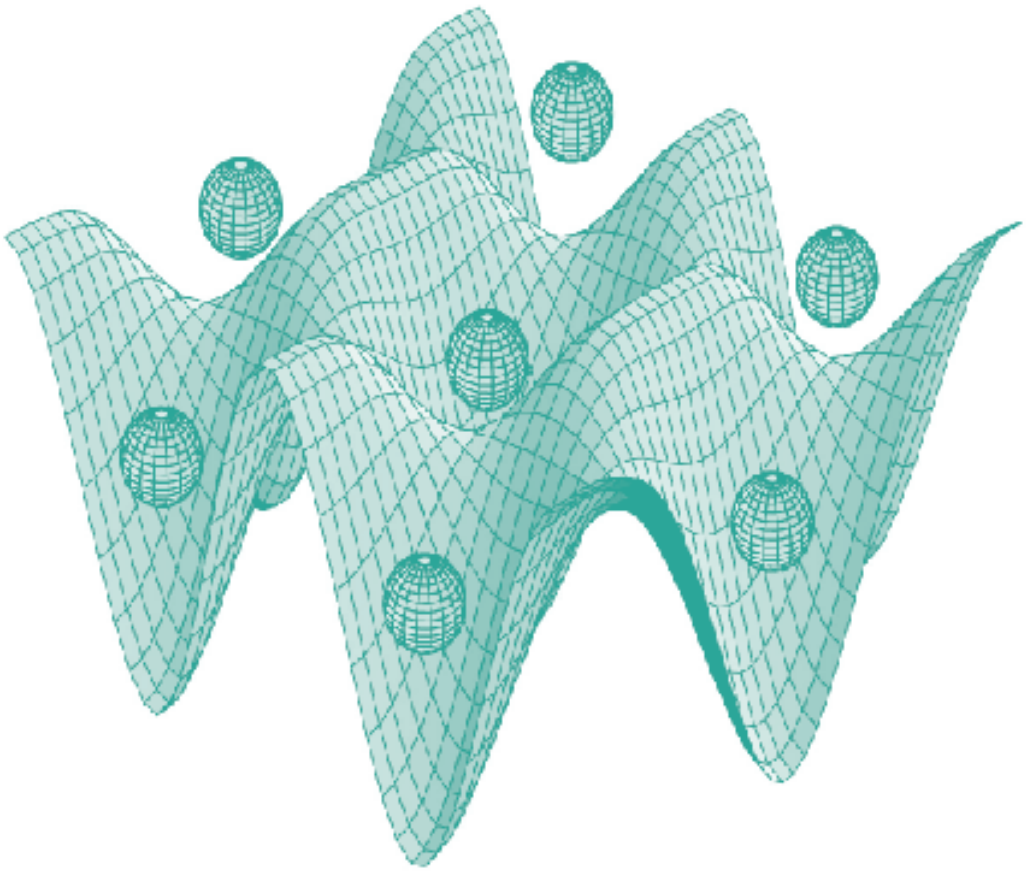

PHYSICA

1/2008

ANUL LIII **2008**

S T U D I A

UNIVERSITATIS BABEŞ–BOLYAI

PHYSICA

1

Desktop Editing Office: 51st B.P.Hasdeu Street, Cluj-Napoca, Romania, phone + 40 264 405352

SUMAR - SOMMAIRE - CONTENTS - INHALT

STUDIA UNIVERSITATIS BABEŞ-BOLYAI, PHYSICA, LIII, 1, 2008

CELLULAR NEURAL NETWORK COMPUTERS AND THEIR APPLICATIONS IN PHYSICS

MÁRIA ERCSEY-RAVASZ*

ABSTRACT. The computational paradigm represented by Cellular Neural/Nonlinear Networks (CNN) and the CNN Universal Machine (CNN-UM) as a Cellular Wave Computer, gives new perspectives for computational physics. Many numerical problems and simulations can be elegantly addressed on this fully parallelized and analogic architecture: solving partial differential equations and implementing cellular automata models are just some basic examples. We also study the possibility of performing stochastic simulations on this chip. First a realistic random number generator is implemented on the CNN-UM, then as an example the site-percolation problem and the two-dimensional Ising model are studied by Monte Carlo type simulations. The results obtained on an experimental version of the CNN-UM with 128×128 cells (ACE16K) are in good agreement with the results obtained on digital computers. Computational time measurements suggest that the developing trend of the CNN-UM chips - increasing the lattice size and the number of local logic memories - will assure an important advantage for the CNN-UM in the near future.

Keywords. Computer modeling and simulation, Statistical physics and nonlinear dynamics, Computer science and technology

PACS: 07.05.Tp, 05.10.Ln, 89.20.Ff

1. Introduction

Many areas of science and especially physics are prefacing serious problems concerning the computing power of the presently available computers. Solving more and more complex problems, simulating large systems, analyzing huge datasets are just a few examples which remind us that computing power needs to keep up with its exponential growth, as expressed by Moore's law [1]. We know however that this process can not continue much further solely with classical digital computers and new computational paradigms are necessary. In the light of the presently emerging quantitative neuroscience, it becomes possible to understand the signal representation and processing in some parts of our nervous system and this is gradually leading to a new and revolutionary different way of computing. Nowadays the technology developed so far that it is possible to imitate some basic principles of our nervous system. Several thousands of microprocessors (cells, neurons) can be placed on a single chip locally interacting with each other similar to a layer of neurons. One suggested prototype architecture for this unconventional computation is the Cellular Wave Computer [2,3], a special case of it being the Cellular Neural Network Universal Machine (CNN-UM) [4].

* *Babeş-Bolyai University, Department of Physics, RO-400084 Cluj-Napoca, Romania*
Pázmány Péter Catholic University, Department of Information Technology, HU-1083 Budapest, Hungary

The history of CNN computing starts in 1988 when the theory of cellular neural/nonlinear networks (CNN) was presented [5]. Few years later a detailed plan for a computer using cellular neural networks was developed. This is called CNN Universal Machine (CNN-UM) [4] and is an analogic (analog+logic) computer which has on its main processor several thousands of interconnected computational units (cells), working in parallel. Since then many experimental hardwares were developed and tested. These chips can be easily connected to digital computers and programmed with special languages. Although the CNN computer is proved to be a universal Turing machine its structure and properties make it suitable for some special complex problems and it is complementing not replacing digital computers. CNN chips are generally used and developed for fast image processing applications. The reason for this is that the cells can be used as sensors (visual or tactile) as well. CNN computers can work thus as a fast and "smart" camera, on which the capturing of the image is followed in real time by analysis [6].

The aim of this article is to present the broad class of applications related to physics which can be effectively realized on CNN computers. First we will briefly summarize some basic applications already studied, like solving in an elegant manner partial differential equations [7,8] or studying cellular automata models [9,10]. These applications result straightforward from the appropriate structure of the CNN chips. After that we argue that CNN-UM can be effectively used also for Monte Carlo type simulations. We will present a realistic random number generator which can use the natural noise of the chip, than we study the site-percolation problem and the two-dimensional Ising model. The results that are presented here were obtained on an experimental version of CNN-UM: the ACE16K chip [11] which has *128*128* cells. After discussing in a critical manner the obtained results and the developing trend of the CNN computers we argue that CNN-UM could represent a useful computational alternative for the near future.

2. Cellular Neural Networks and the CNN Universal Machine

The standard Cellular Neural Network (CNN) [5] is composed by *L*L* cells placed on a square lattice and interconnected through *8* nearest neighbors. Each cell is an electronic circuit in which the most important element is a capacitor. The voltage of this capacitor is called the state value of the cell $x_{i,j}(t)$. The cell has also an input value (voltage) $u_{i,j}$, which is constant in time and can be defined at the beginning of an operation. The third characteristic of the cell is the output value $y_{i,j}(t)$. This is equivalent with the $x_{i,j}$ state value in a given range. More specifically it is a piece-wise linear function, bounded between *-1* (white) and *1* (black):

$$y_{ij} = f(x_{ij}) = \tfrac{1}{2}(|x_{ij}+1| - |x_{ij}-1|) . \qquad (1)$$

The connections between the cells are realized with voltage-controlled resistors which implies that the state value of each cell depends on the input and output

values of the connected neighbors. The state equation of the CNN cells results from the time-evolution of the equivalent circuit. Assuming the *8* neighbor interactions it will be the following [5]:

$$\frac{dx_{ij}(t)}{dt} = -x_{ij}(t) + \sum_{k=-1}^{1}\sum_{l=-1}^{1} A_{kl}\, y_{i+k,\,j+l}(t) + \sum_{k=-1}^{1}\sum_{l=-1}^{1} B_{kl}\, u_{i+k,\,j+l} + z_{ij} \qquad (2)$$

The coupling between neighbors can be controlled with the matrices *A* and *B*. Within the standard CNN (and on the hardwares realized up to the present days) *A* and *B* are the same for all cells. Parameters $z_{i,j}$ are constants which can be changed from cell to cell. The set of parameters *{A,B,z}* is called a template. An operation is performed by giving the initial states of the cells, the input image (the input values of all cells) and by defining a template. The states of all cells will vary in parallel and the result of the operation will be the final steady state of the CNN. Each operation is equivalent with solving a differential equation defined by the template itself, with the extra condition that the state of a cell remains bounded in the *[-1,1]* region [12].

The CNN-UM [4] is a programmable cellular wave computer in which each cell contains additionally a local analog and a logic unit, local analog and logic memories and a local communication and control unit. Beside these local units, the CNN-UM has also a global analog programming unit which controls the whole system, making it a programmable computer. It can be easily connected to PC type computers and programmed with special languages, for example the Analogic Macro Code (AMC). The physical implementations of these computers are numerous and widely different: mixed-mode CMOS, emulated digital CMOS, FPGA, and also optical. In the following we will usually refer to mixed-mode implementations.

For practical purposes the most promising applications are for image processing, robotics or sensory computing purposes [13], so the main practical drive in the mixed-mode implementations was to build a visual microprocessor [3]. The cells of the computer are additionally equipped with sensors (usually visual sensors, but in special applications these can be tactile or of other type). By this way optical sensing and computing are inherently topographically coupled and implemented on the surface of a silicon chip. The first self-contained camera-computer, containing a CNN-UM type visual microprocessor (ACE16K), was built recently, as the Bi-i camera-computer [6]. Its input flow speed achieves *20000* frames/s including sensing and processing. On *Table 1*. we can see the size of some CNN chips realized in the last decade. It is important to mention that parallel with increasing the lattice size of the chips engineers are focusing on developing multi-layered, *3* dimensional chips as well. This trend opens again new and fascinating application possibilities.

Table 1.
Evolution of the CNN-UM chip, different physical realizations. From these chips only the ACE16K [11] and the Q-Eye [14] are commercially available, mass production began with the Q-Eye at the end of 2006.

Name	***Year***	***Size***
---	1993	12*12
ACE440	1995	20*22
POS48	1997	48*48
ACE4k	1998	64*64
CACE1K	2001	32*32*2
ACE16K	2002	128*128
XENON	2004	128*96*2
Q-EYE	2006	176*144

3. Applications of CNN Computers in Physics

There are many applications related to physics ideal for the analogic (analog & logic) architecture of the CNN-UM. Solving partial differential equations is relatively easy and offers the advantage of continuity in time [7,8]. Deterministic cellular automata [9] with simple nearest-neighbor rules are also straightforward to implement on the CNN architecture. The natural noise of the chip can be used to generate realistic random numbers, which can be used in many different kind of stochastic simulations. As examples the site-percolation problem and the two-dimensional Ising model will be presented here.

3.1. Solving partial differential equations on CNN-UM

There are many papers dealing with partial differential equations on CNN [7,8,15], here we will present a typical example: solving the equation of heat propagation. We saw in section 2 that the state equation of the CNN is a system of Ordinary Differential Equations (ODE). It can be rigorously shown that the state values of the cells always tend to a final steady state. This final equilibrium state of the system (the output) is the numerical solution of this ODE system. Whenever one wants to obtain the non-analytic solution of a partial differential equation with different kind of algorithms implemented on digital computers, spatial discretization is performed. This procedure transforms the PDE in a system of ordinary differential equations (ODE's), so from the spatially continuous system we obtain an array of small, discrete interacting systems. This system of ODE's can be solved on the CNN by choosing the appropriate interacting parameters, and the appropriate template: *{A,B,z}*. On digital computers, not only the space-like but the time-like variables and the interaction parameters are all taken as discrete. In contrast with this CNN works with continuous time, continuous values, and continuous interaction parameters.

With the CNN architecture presented in the previous section only linear partial differential equations can be solved, because the state equation contains only linear functions of the input and output values. Theoretically we could build

an appropriate cellular neural network for any kind of nonlinear PDE introducing other connecting parameters, but in practice only the already presented structure was realized. We will present the method of finding the appropriate CNN template for a PDE on the well-known heat propagation equation. The two-dimensional form of this equation writes as:

$$\frac{\partial u(x, y, t)}{\partial t} = c\nabla^2 u(x, y, t), \tag{3}$$

where *u(x,y,t)* is the intensity (when talking about thermodynamic problems: the temperature, at time *t* and at coordinates *x,y*) and *c* is a constant. First a spatial discretization should be performed, for transforming the PDE in a system of ODE's, which will be than compared with the state equations of the cellular neural network. We make this discretization in equidistant steps in both directions: $\Delta x = \Delta y = h$. We will map the temperature *u(x,y,t)* into a CNN layer, so the state value of a cell: x_{ij} will be equal with *u(ih,jh,t).* The derivatives should also be approximated based on the Taylor-series expansion. The first derivative would be:

$$\frac{\partial u}{\partial x} \cong \frac{1}{2h}\left[u(x+h, y) - u(x-h, y)\right] = \frac{1}{2h}\left[u_{i+1,j} - u_{i-1,j}\right] \tag{4}$$

and the second derivative:

$$\frac{\partial^2 u}{\partial x^2} \cong \frac{1}{h^2}\left[u(x+h, y) - u(x, y) - u(x, y) + u(x-h, y)\right] = \frac{1}{h^2}\left[u_{i+1,j} - 2u_{i,j} + u_{i-1,j}\right] \tag{5}$$

Using this approach the heat propagation equation will look like:

$$\frac{\partial u_{i,j}}{\partial t} = \frac{c}{h^2}\left(u_{i+1,j} + u_{i,j+1} + u_{i-1,j} + u_{i,j-1} - 4u_{i,j}\right). \tag{6}$$

Comparing this equation with the state equation (2) we can identify now the templates. Giving the matrix form of the templates we can write:

$$A = \begin{pmatrix} 0 & \frac{c}{h^2} & 0 \\ \frac{c}{h^2} & 1-4\frac{c}{h^2} & \frac{c}{h^2} \\ 0 & \frac{c}{h^2} & 0 \end{pmatrix}, \text{ B=0, z=0.} \tag{7}$$

As an example the solution obtained with the ACE16K CNN chip, with 128*128 cells is presented on Fig.1. The initial state was an image with patches, the final state is a much smoother image as expected for the heat propagation equation. The solution can be obtained on this CNN chip in approximately 20 ns.

Here we have to mention that this method of solving PDE's with CNN is valid only if the state values remains bounded between (-1,1), so the output values will always be equal to the state-values. This is what we assumed when we identified the templates comparing the equations (6) and (2). Choosing appropriate initial conditions we can use this approach and the partial differential equation can be solved efficiently.

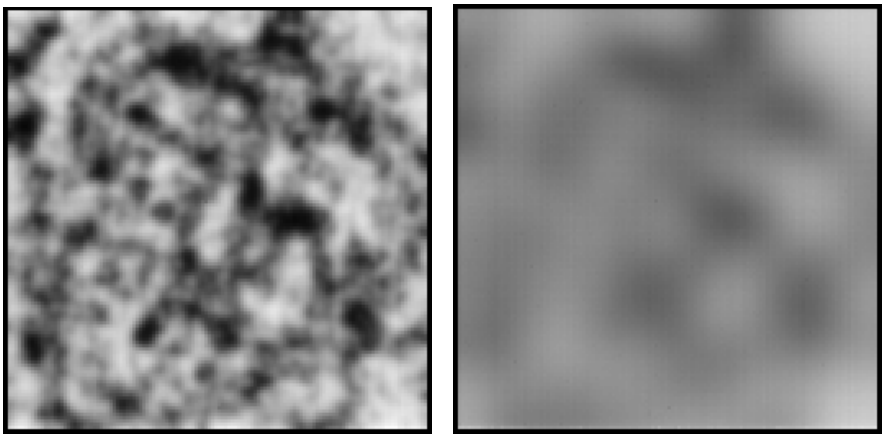

Fig. 1. Heat propagation equation solved with the ACE16K CNN chip with 128*128 cells. The initial condition and the final solution is presented.

3.2. Cellular automaton on CNN

The cellular structure makes CNN appropriate also for implementing cellular automata (CA) models. Depending on the basic rule of the CA it can be implemented on the CNN with one or sometimes more consecutive templates. The effectiveness of CNN in handling CA models consists in parallel processing: the rule is performed in each cell at the same time-moment.

Some basic examples are the dilation (and erosion) processes, where all cells having one defined neighbor black (white) will become black (white). For ex. *dilation to the left side* is represented by the template: *A={0}, B={0,0,0,1,1,0,0,0,0}, z=1*. The e*rosion from left and down* will look like: *A={0}, B={0,0,0,1,1,0,1,0,0}, z=-2*. Many other templates used in image processing are also cellular automata models: finding the edges, contours, corners; finding local maxima or minima on grayscale images; shadowing etc.

More complicated CA models can be implemented with several consecutive templates. For example one of the most used pseudo-random number generators on CNN, presented by Crounse *et al.*[10] and Yalcin *et al.* [16] is a simple but effective chaotic cellular automaton, called the PNP2D. This chaotic CA is based on the following update rule:

$$x_{t+1}(i,j) = (x_t(i+1,j) \vee x_t(i,j+1)) \oplus x_t(i-1,j) \oplus x_t(i,j-1) \oplus x_t(i,j), \quad (8)$$

where *i*,*j* are the coordinates of the pixels, the index *t* denotes the time-step, and *x* is a logic value *0* or *1* representing white and black pixels, respectively. Symbols $\vee$ and $\oplus$ represent the logical operations or and exclusive-or (XOR), respectively. This CA can be implemented with *4* consecutive templates performing the logic operations.

3.3. Generating realistic random numbers on CNN

It is well known that for a successful stochastic simulation the crucial starting point is a good random number generator. While computing with digital processors, the "world" is deterministic and discretized, so in principle there is no possibility to generate random events and thus really random numbers. The implemented random number generators are in fact pseudo-random number generators working with some deterministic algorithm, and it is believed that their statistics approximates well real random numbers. Our goal is to take advantage on the fact that the CNN-UM chip is an analog device, and to use its natural noise for generating more realistic random numbers. This would assure an important advantage in Monte Carlo type simulations, relative to digital computers. The natural noise of the CNN-UM chip is usually highly correlated in space and time, so it can not be used directly to obtain random binary images. Our method is based thus on a chaotic cellular automaton perturbed with the natural noise of the chip after each time step. Due to the used chaotic cellular automaton the correlations in the noise will not induce correlations in the generated random black and white pixels and the real randomness of the noise will kill the deterministic properties of the chaotic cellular automaton [17].

As starting point a good pseudo-random number generator, the chaotic CA presented in the previous section, called PNP2D was chosen [10]. As described by the authors this chaotic CA is relatively simple and fast, it passed all important RNG tests and shows very small correlations. It generates binary values *0* and *1* with the same *1/2* probability independently of the starting condition. Our method for transforming this into a realistic RNG is relatively simple. After each time step the *P(t)* result of the chaotic CA is perturbed with a noisy *N(t)* binary picture (array) so that the final output is given as:

$$P'(t) = P(t) \oplus N(t) \quad (9)$$

The symbol $\oplus$ stands again for the logical operation XOR, i.e. pixels which are different on the two pictures will become black (logic value *1*). This operation assures that no matter how *N(t)* looks like, the density of black pixels remains the same *1/2*. Because the used noisy images contain only very few black pixels (logic values *1*) we just slightly sidetrack the chaotic CA from the original deterministic path and all the good properties of the pseudo-random number generator will be preserved.

The *N(t)* noisy picture is obtained by the following simple algorithm. All pixels of a gray-scale image are filled up with a constant value *a* and a cut is

realized at a threshold $a+z$, where z is a relatively small value. In this manner all pixels which have smaller value than $a+z$ will become white (logic value *0*) and the others black (logic value *1*). Like all the logic operations this operation can be also easily realized on the CNN-UM. Due to the fact that the used CNN-UM chip is an analog device, there always will be natural noise on the gray-scale image. Choosing thus a proper z value one can generate a random binary picture with few black pixels. Since the noise is time dependent and generally correlated in time and space, the $N(t)$ pictures might be strongly correlated but will definitely fluctuate in time. These time-like fluctuations can not be controlled, these are caused by real stochastic processes in the transistor circuits of the chip and are the source of a convenient random perturbation for the RNG based on a chaotic CA.

Using now n independent random binary images, all with $1/2$ density of the black pixels, it is possible to generate pictures with any p probability of the black pixels (p being a number represented by n -bits, when expressed as a power of $1/2$). For more details see [17].

This RNG and the described algorithms were tested and are properly working on an ACE16K chip which is an experimental version of the CNN-UM with *128*128* cells. It is found that the RNG with $p=0.5$ is almost *5* times faster on the ACE16K than on modern PC type digital computers. Generating images with other p probabilities is of course slower, depending on n (see [17]). Taking into account thus the natural trend that the lattice size of CNN-UM chips will be growing and that calculations on this chip are totally parallel, these results predict a promising trend. Some codes and movies about the RNGs on the ACE16K chip are available on the home-page dedicated to this study [18].

3.4. Monte Carlo type simulations on the CNN-UM

The realistic binary random number (image) generator developed in the previous section can be used with success for Monte Carlo type simulations on the CNN-UM chip. As an example in this sense, here we study two classical problems: the site-percolation problem and the two-dimensional Ising model.

3.4.1. The site-percolation problem on the CNN-UM

Percolation type problems are very common in many areas of sciences like physics, biology, sociology and chemistry (for a review see e.g. [19]). Different variants of the problem (site percolation, bond percolation, directed percolation, continuum percolation etc.) are used for modeling various natural phenomena [20]. As an example, the simple site percolation problem is widely used for studying the conductivity or mechanical properties of composite materials, the magnetization of dilute magnets at low temperatures, fluid passing through porous materials, forest fires or propagation of diseases in plantations etc. The site-percolation model exhibits a second order geometrical phase transition and it is important also as a model system for studying critical behavior [21].

On implementing the site-percolation problem on the CNN-UM the array of cells will represent the square lattice on which percolation is studied. In the following the state of the lattice will be referred as a binary picture, black pixels pointing for activated and white pixels for non-activated sites. In the classical site-percolation problem one is interested whether it is possible or not to go from one side of the picture to the opposite side through activated and neighboring pixels (here we are considering *8* nearest neighbors for each cell). If there is a path that satisfies this condition, it is considered that the black (activated) pixels percolate through the lattice.

Finding the complicated connected path through neighboring black pixels takes only a single operation on the CNN chip. We are using a template (the parameters in eq. 2.), called "*figure reconstruction*" with parameters: *A={0.5,0.5,0.5,0.5,4,0.5,0.5,0.5,0.5}, B={0,0,0,0,4,0,0,0,0},z=3.* The input picture of the template is the actual random image and the initial state will contain only the first row of the image. Analyzing the template one can easily realize that pixels which have an input value equal to *1* (are black) and have at least one neighbor with state value *1* will become black. In this manner a flow starts from the first row making black all the pixels which were black on the input picture and are connected through neighbors to the first row. If on the final output will remain black pixels in the last row, then percolation exists. This simple template is a function in the image processing library of the Bi-i v2 [22]. It is immediate to realize that by using a locally variant CNN in which these *A* and *B* matrices can vary from cell to cell also bond-percolation and directed percolation problems would be solvable with the same simple algorithm.

Applying this template on many random images and by changing also the *p* activation probabilities it is possible to study the phase-transition in the classical site-percolation problem. After a good statistics it is possible to determine how the probability of percolation ρ depends on the density of activated pixels, and consequently where the critical density p_c is. The CNN code written for this application can be downloaded from [18].

Results for the $\rho(p)$ curve obtained on the ACE16K chip are plotted with circles in Fig.2. On the same graph it is also sketched with square symbols the MC simulation results obtained on a digital Pentium 4, *2.8* GHz computer, using a recursion-type algorithm for detecting percolation. The lattice size in both cases is *128×128* and the results are averaged for *10000* different random images for each activation probability values. The two curves show a pretty good agreement. The percolation threshold resulting from the simulated $\rho(p)$ curves are in good agreement with the accepted p_c critical value for this case (site-percolation on a square lattice with *8* neighbors): $p_c=0.407$.

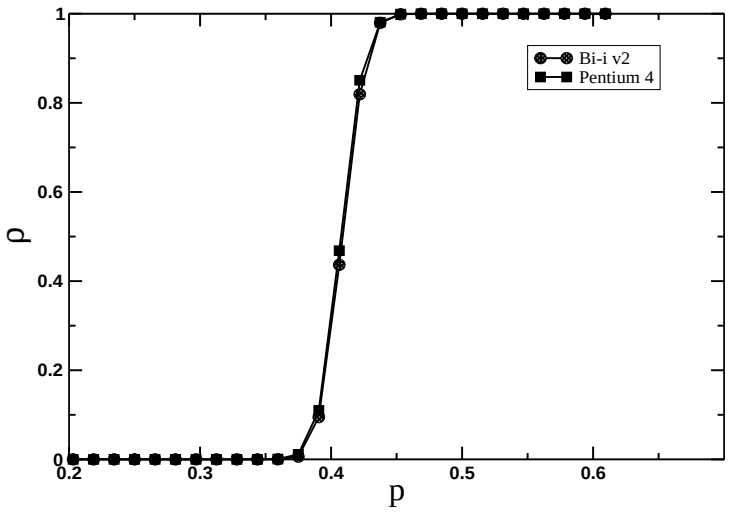

Fig.2. Simulated site-percolation probability as a function of the density of black pixels. Circles are results obtained on the CNN-UM chip, squares are simulation results on a normal PC type digital computer

Comparing the speed of the Monte Carlo type simulations performed on digital computers and on the ACE16K chip the following observations can be summarized: (i) with the presently available chip size (*L=128*) and the experimental version of the CNN-UM the simulation is almost *10* times slower than on a digital computer with a *2.8* GHz Pentium 4 processor, (ii) on the CNN-UM the time needed for detecting percolation grows linearly with the linear size of the respective image, while on digital computers it scales with the square of the linear size of the lattice. Increasing thus the size of the chip will definitely favor the CNN-UM architecture for such Monte Carlo type simulations.

Since the ACE16K chip was developed mainly for image processing on analog images, the number of local logic memories is small. Due to the fact that for the site-percolation problem binary images are used the absence of enough number of local logic memories slowed down the implementation of the algorithm considerably. We have to mention also that some of the CNN instructions are not efficient on the present chip. The new chips (presently under fabrication) are capable of performing these operation much more efficiently, increasing further the computational speed on the CNN-UM.

3.4.2. *The Ising model on the CNN-UM*

As a second specific problem in statistical physics we now consider the well-known two-dimensional Ising model. Implementing an MC study for this model on the CNN-UM is however not trivial. As it will be argued later a straightforward application of the usual Glauber [23] or Metropolis [24] algorithms could lead to unexpected problems due to the completely parallel architecture of the dynamics.

In the Ising model the spins can have two possible states $\sigma = \pm 1$. On the CNN-UM these spin states can be mapped as "black" or "white" states of the cells. Without an external magnetic field the Hamiltonian of the system is:

$$H = -J \sum_{<i,j>} \sigma_i \sigma_j \tag{10}$$

<i,j> representing nearest neighbors. There are many different MC type methods for studying this basic lattice model. Most of them like the Metropolis [24] or the Glauber [23] algorithm are of serial nature, meaning that in each step we update one single spin. Working however in parallel with all spins, could create some unexpected problems since nearest neighbors are updated simultaneously. Imagine for instance an initial state where the spin-values are assigned following a chessboard pattern. This state will have a zero total magnetization. Let us consider now the zero-temperature ferromagnetic case and the Glauber or Metropolis algorithm. Contrary to what is expected, this system will not order in a pure "black" or "white" ferromagnetic phase but it will continuously switch between the two complementary chessboard patterns. For eliminating the parallel update of the neighbors that causes such problems, and still taking advantage of the parallel nature of the computer, we impose an extra chessboard mask on the array. In each odd (even) step we update simultaneously the spins corresponding to the black (white) cells of the chessboard mask. For updating the chosen spins the Metropolis algorithm is then used. It is simple to realize that our method is equivalent with the classical serial Metropolis dynamics in which the spins are updated in a well-defined order. Detailed balance and ergodicity are satisfied, so the obtained equilibrium statistics should be the right one.

Implementing the above scheme on the CNN-UM is realized as follows [25]. In each step we first build three additional masks: the first marks the spins with *4* similar neighbors ($\Delta E=8J$), the second one marks the spins with *3* similar neighbors ($\Delta E=4J$), and the third represents all the other spins for which $\Delta E \leq 0$. Separating these cells is relatively easy using logic operations and some special templates which can shift the images in different directions. We generate two random images with probability $exp(-8J/kT)$ and $exp(-4J/kT)$ and we perform an AND operation between the random image and the corresponding mask. After uniting the results of these two and the third mask $(\Delta E \leq 0)$ we get a new mask which marks all spins which have to be flipped. Finally we use the chessboard mask and allow only those spins to flip which correspond to black (white) pixels if the time-step is odd (even). The CNN code developed for studying this problem can be also downloaded from the home-page dedicated to this study [18].

Simulation results obtained with a Metropolis type algorithm are presented on fig. 3. On this figure we compare results of (i) the classical Metropolis algorithm on a digital computer, (ii) the results of our parallel algorithm simulated on a digital computer and (iii) the results obtained on the ACE16K chip. By plotting the average magnetization, the specific heat and the susceptibility as a function of the temperature

one can conclude that different results are in good agreement with each other. All simulations were performed on a *128*128* lattice using free boundary conditions.

Fig.3.d. shows the time needed for *1* MC step as a function of the lattice size *L*. While on a PC type computer this scales as L^2, on the CNN-UM the time does not depend on the lattice size (each command is executed in a fully parallel manner on the whole lattice). The time measured on the ACE16K chip with *L=128* was *4.8* ms , while on a Pentium 4 PC working at *2.8* GHz under Linux operating system the time needed for *1* MC step was *2* ms. For this lattice size the simulations are still faster on the classical digital computers however the difference is again caused by the low number of local binary memories, which results in time-consuming extra operations in our algorithms. Taking into account the trend that the size of the CNN chip (Table 1) and the number of local memories will increase in the near future these results are also promising.

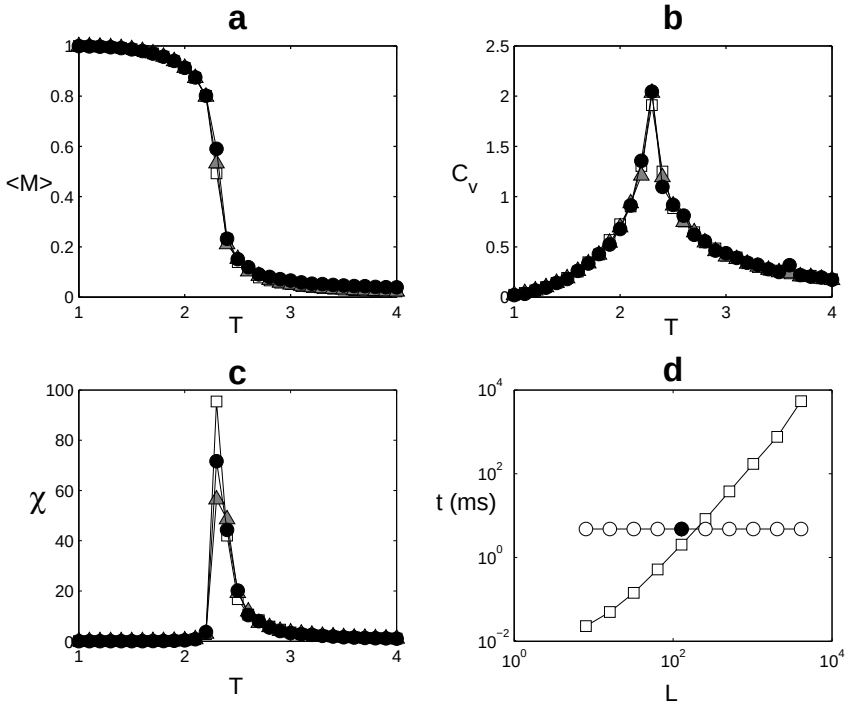

Fig. 3. Average magnetization M (a), specific heat C_v (b) and susceptibility χ (c) are plotted as a function of the temperature T for the classical Metropolis algorithm on a digital computer (squares), our parallel algorithm simulated on a digital computer (triangles) and the algorithm simulated on the ACE16K CNN-UM chip (circles). Figure (d) compares the simulation time t (in ms) needed for 1 MC step on a Pentium 4 PC with 2.8 GHz (squares) and the CNN-UM (circles) as a function of the lattice size L . The filled circle marks the simulation time obtained on the ACE16K chip (L=128).

4. Conclusions

Cellular wave computers [2,3] and as a special case the Cellular Neural Network Universal Machine [4] represents a new computation paradigm. They are inspired upon some basic principles of our nervous system (specially the retina): (i) several thousands of cells (neurons) locally interconnected with each other and working totally in parallel; (ii) the states are described with analog values; and (iii) the evolution of the system is continuous in time. The system is mainly used for developing visual microprocessors [6,11,14]. In the present work we have shown that the CNN-UM chips can be also useful in applications related to physics. Continuity in time and it's parallel structure is useful for solving partial differential equations and implementing cellular automata models. The natural noise of the chip can be effectively used in stochastic simulations, and the parallel nature is very appropriate when simulating lattice models. Experimental results are promising. By increasing the lattice size of the chips and the number of local memories in the near future, will definitely favor such kind of computational approaches. Quasi three-dimensional chips with several layers of cells are already appearing, introducing a new level of complexity and many new possibilities for its applications.

BIBLIOGRAPHY

1. G. Moore, *Electronics* **38**, 114 (1965)
2. T. Roska, *Journal of Circuits, Systems and Computers*, **5**, No.2, 539 (2003)
3. T. Roska, *Electronics Letters* **43**, No.8 (2007)
4. T.Roska, L.O. Chua, *IEEE Transactions on Circuits and Systems - II* **40**, 163 (1993)
5. L.O. Chua, L. Yang, *IEEE Transactions on Circuits and Systems* **35**, 1257 (1988)
6. Á. Zarándy, C. Rekeczky, *IEEE Circuits and Systems Magazine* **5**, 36 (2005)
7. T. Roska, L.O. Chua, D. Wolf, T. Kozek, R. Tetzlaff, F. Puffer, *IEEE Transactions on Circuits and Systems - I: Fundamental Theory and Applications* **42**, 807 (1995)
8. T. Kozek, L.O. Chua, T. Roska, D. Wolf, R. Tetzlaff, F. Puffer, K. Lotz, *IEEE Transactions on Circuits and Systems - I: Fundamental Theory and Applications* **42**, 816 (1995)
9. J.M. Cruz, L.O. Chua, *IEEE Transactions on Circuits and Systems I: Fundamental Theory and Applications* **42**, 715 (1995)
10. K.R. Crounse, T. Yang, L.O. Chua, *Fourth IEEE International Workshop on Cellular Neural Networks and their Applications*, Seville, Spain (1996)
11. A. Rodriguez-Vázquez, G. Linan Cembrano, *IEEE Transactions on Circuits and Systems I.* **51**, 851 (2004)
12. L.O. Chua, T. Roska, *Cellular Neural Networks and Visual Computing* (Cambridge University Press, 2002)
13. K.R. Crounse, L.O. Chua, *IEEE Trans. on Circuits and Systems* **42**, 583 (1995)
14. www.anafocus.com
15. T. Kozek, T. Roska, *International Journal of Theory and Applications* **24**, 49 (1996)

16. M.E. Yalcin, J. Vandewalle, P. Arena, A. Basile, L. Fortuna, *International Journal of Circuit Theory and Applications* **32**, 591 (2004)
17. M. Ercsey-Ravasz, T. Roska, Z. Néda, *International Journal of Modern Physics C* **17**, No. 6, 903 (2006)
18. M. Ercsey-Ravasz, T. Roska, Z. Néda, http://www.phys.ubbcluj.ro/~zneda/cnn.html (2005)
19. D. Stauffer, A. Aharony, *Introduction to Percolation Theory*, (London, second edition, Taylor and Francis, 1992)
20. M. Sahimi, *Application of Percolation Theory*, (London, Taylor and Francis, 1994)
21. D. Stauffer, *American Journal of Physics* **45** (10), 1001 (1977)
22. I. Szatmári, P Földesy, C. Rekeczky, Á Zarándy, *Proceedings of the CNNA-2002* Frankfurt, Germany (2002)
23. J. Glauber, *J. Math. Physics* **4**, 194 (1963)
24. N. Metropolis, A. Rosenbluth, M. Rosenbluth, A. Teller, E. Teller, *J. Chem. Phys.* **21**, 1087 (1953)
25. M. Ercsey-Ravasz, T. Roska, Z. Néda, *European Physical Journal B* **51,** 407 (2006)

STUDIA UNIVERSITATIS BABEŞ-BOLYAI, PHYSICA, LIII, 1, 2008

STRUCTURE AND THERMAL BEHAVIOUR OF APATITIC CALCIUM PHOSPHATES: GLASS MELTING VERSUS SOL-GEL SYNTHESIS

S. SIMON, D. LAZĂR, H. MOCUȚA*

ABSTRACT. Apatitic calcium phosphate samples were synthesised by glass melting and sol-gel methods. Hydroxyapatite crystalline phase was developed in the heat treated glass sample. A nanostructured hydroxyapatite was obtained following the sol-gel synthesis route after drying at 110°C. The structure and thermal behaviour were investigated by X-ray diffraction, thermogravimetric and differential thermal analyses.

Keywords. Structure, Thermal behaviour, Sol-gel synthesis

Introduction

Hydroxyapatite, HA ($Ca_{10}(PO_4)_6(OH)_2$), is an important biomaterial because it is the principal inorganic constituent of bones and teeth. The bone inorganic part consists in an amorphous phase of tricalcium phosphate and a crystalline phase of HA with nanometric crystal sizes. In the enamel of teeth, containing about 95% of HA, the crystals are bigger but still with submicrometric sizes. HA coatings on metallic substrates offer great improvement in orthopaedic and dental applications and are successfully used in clinical practice due to the chemical and biological similarity of HA to the human hard tissues and also direct bonding capability to the surrounding tissues [1 - 3]. It has been established that HA coatings promote early bone apposition and fixation for HA-coated implants by encouraging chemical bonding between new bone and the surface of HA [4]. HA coating is also believed to protect the metallic substrate from corrosion in the biological environment, as well as serving as an effective barrier against the release of toxic metal ions from the metallic substrates into the living body [5]. There is a great demand of this material in odontology and traumatology. Due to the biocompatibility of synthetic HA [1, 6], it is used in the reconstruction of damaged bones or teeth. To produce a material with similar microstructure to HA is of great interest in the areas of biomedicine linked to the development of prostheses for bone reconstitution or substitution. This is due to the unique property of bone tissue to regenerate, forming new healthy tissue that grows in the direction of the damaged area, filling in with functional bone.

HA also finds applications in others fields of industrial or technological interest as catalyst, in chromatography or gas sensor, in water purification, fertilizers production or manufacturing of biocompatible ceramics [7].

* *Faculty of Physics, Babes-Bolyai University, Cluj-Napoca 400084, Romania*

A number of methods have been used for HA powder synthesis. Sol-gel synthesis of HA ceramics has attracted much attention [8 – 13]. The sol-gel method offers a molecular-level mixing of the calcium and phosphorus precursors, implying advantages in comparison with the conventional methods. Besides, the sol-gel approach provides more convenient conditions for the synthesis of HA powders and films. Sol-gel method is an easy way to produce high purity glass systems at room temperature and is frequently used for preparing glasses and glassceramic powders [14]. Glass samples obtained by sol-gel route offer the advantage of high chemical homogeneity and lower preparation temperature, especially as compared with the glasses of the same composition obtained by melting method. Some of the most interesting applications of the sol–gel method include the synthesis of fine nanoparticles [15].

The sol-gel preparation involves first the formation of a sol, which is a suspension of solid particles in a liquid, then of a gel, which is a diphasic material with a solid encapsulating a liquid. The liquid can be removed from the gel by either conventional drying to obtain a product known as a xerogel, or by drying with supercritical extraction to give an aerogel. Preparing materials with the sol-gel method has received increasing attention in recent years because of its versatility and excellent control over the properties of the prepared materials. There are several experimental variables, generally referred to as the sol-gel parameters, like the gel time, the starting precursors, and the drying conditions, which can impact on the physical and chemical characteristics of a sample. The subsequent processing steps - aging, drying and heat treatment - are often interrelated and all of them have to be considered in the synthesis of a sol-gel material [16].

This work is focussed on a comparative study of structure and thermal properties of a hydroxyapatite type sample obtained by glass melting method and a hydroxyapatite synthesised following the sol-gel route.

Experimental

Glass samples belonging to $20Na_2O \cdot 30CaO \cdot 50P_2O_5$ system were prepared using as start materials $Na_2CO_3 \cdot 10H_2O$, $CaCO_3$ and $NH_4H_2PO_4$ reagents of p.a. purity. The addition of sodium oxide is very convenient for diminishing the melting temperature of calcium-phosphate glass systems. On the other hand, the mineral phase of the human bones also contains a biologically significant amount of Na^+ and K^+ ions [17].

The mixtures corresponding to the desired composition was melted at 1200^oC in air at atmospheric pressure for 15 minutes and quickly undercooled at room temperature by pouring and pressing between two stainless steel plates.

In order to prepare hydroxyapatite by sol-gel method we used as precursor reagents $Ca(NO_3)_2$ and $(NH_4)_2HPO_4$. The Ca/P molar ratio in precursors was 1.67 like in the natural hydroxyapatite contained in the bone.

$Ca(NO_3)_2$ and $(NH_4)_2HPO_4$ were independently dissolved in distilled water, in two vessels, with the assistance of a magnetic stirrer. The $(NH_4)_2HPO_4$ solution was progressively added to the calcium containing solution and the mixture was stirred at a temperature close to 90°C. This mixed solution was allowed to age up to sol-gel formation and then sol-gel was washed in distilled water at ambient temperature and dried in an electric oven, in air under normal pressure, at 110°C for 2 hours.

The samples were crushed in an agate mortar and analysed by X-ray diffraction, thermo-gravimetric and differential thermal analysis. The X-ray diffraction analysis was carried out on a Shimatzu diffractometer using CuK_α radiation. For thermal investigation the thermogravimetric (TG), differential thermogravimetric (DTG) and differential thermal analysis (DTA) curves were recorded with a heating rate of 10 °C/min on a MOM type derivatograph in a stationary air atmosphere.

Results and discussion

The sample obtained by undercooling from melting to room temperature is in vitreous state as indicate the X-ray powder diffraction pattern (Fig. 1a) which consist of a single broad peak and do not reveal any crystalline phase in the as prepared sample.

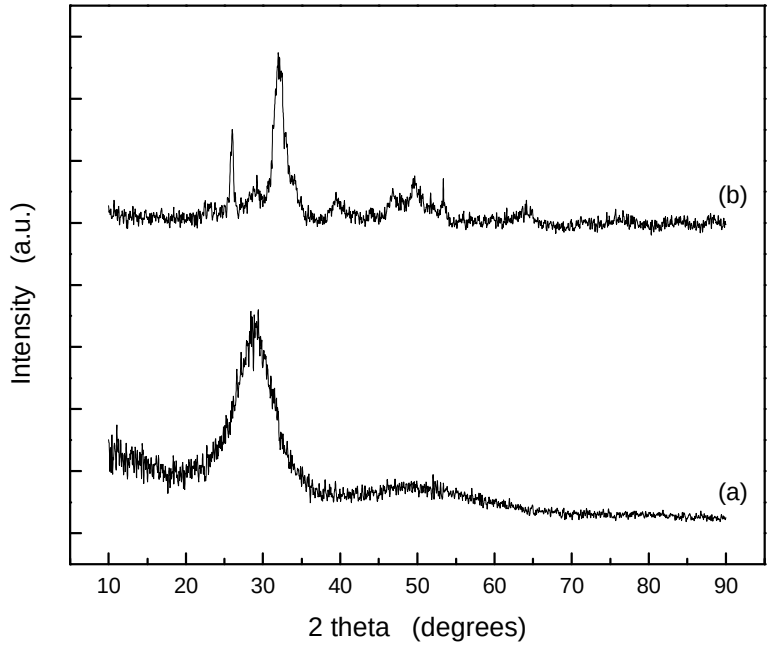

Fig. 1. XRD patterns of apatitic samples synthesised by (a) glass melting and (b) sol-gel method.

The differential thermal analysis confirms the vitreous state of the investigated sample and evidences (Fig. 2) a glass transition temperature close to 425°C and an exothermic event related to the crystallisation process with a maximum at 591°C. The large range between the temperature of the crystallisation peak maximum and the glass transition temperature points out that this sample has a good glass stability [18]. An endothermic event related to the melting process starts about 700°C and the maximum of the corresponding peak is recorded at 772°C. According to the information taken from the DTA run, a heat treatment temperature of 650°C was chosen for the purpose of sample crystallisation. The heat treatment was applied for 2 hours and the sample was then slowly cooled in the furnace to room temperature.

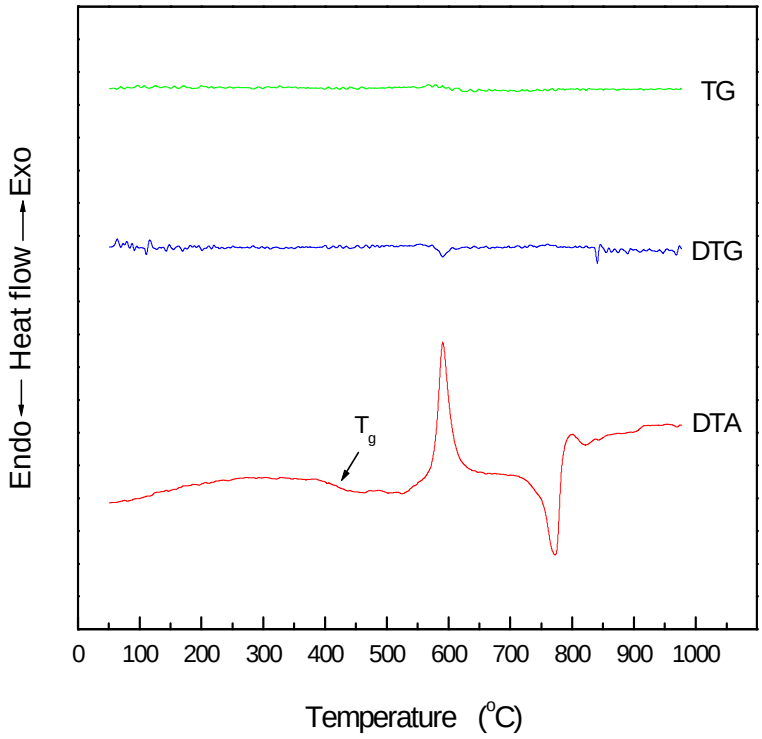

Fig. 2. Thermal analysis curves of the sample obtained by glass melting method.

The X-ray diffraction pattern recorded from the heat treated sample (Fig. 3) shows the development of crystalline hydroxyapatite. Diffraction lines occurring close to 2θ values reported in literature for hydroxyapatite [19 - 22], at 22.9° for reflection (111), at 24.2° for reflection (002), at 30.8° (triplet) for reflections (211), (112) and (300), and at 34.0° for reflection (200) are present in this diffractogram.

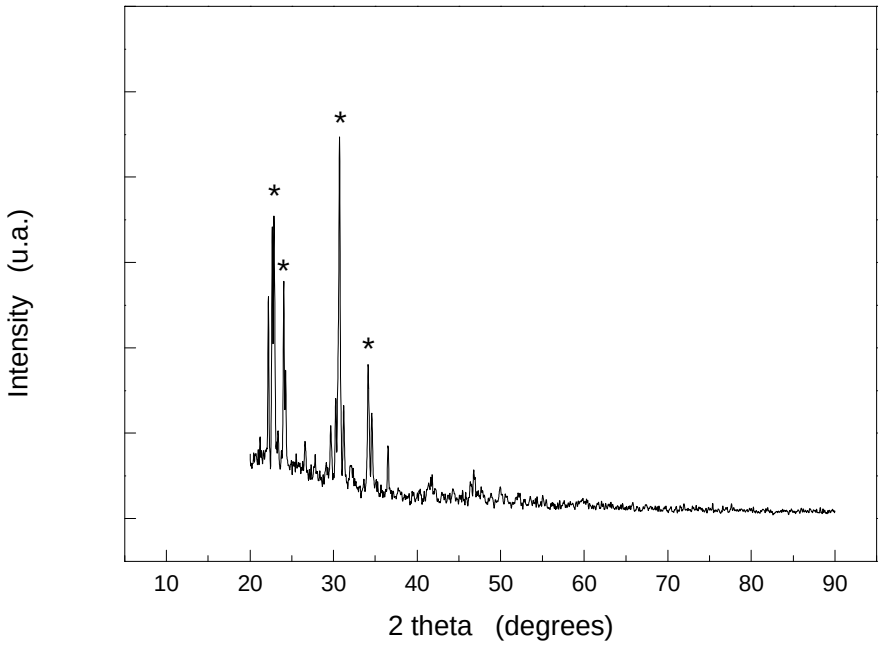

Fig. 3. XRD pattern of the sample obtained by glass melting method after heat treatment at 650°C.

The X-ray diffraction pattern of the as prepared sol-gel sample (Fig. 1b) reveals features of hydroxyapatite crystallites and is almost identical with the XRD patterns for in situ and ex situ mineralized HA [23]. The diffraction lines at 2θ angles of 25.8, 29, 32, 34.1, 39.7, 46.7, 49.6, 53.3 and 64° are arising from the reflection planes 002, 210, (211, 112, 300), 200, 310, 222, 213, 004 and 323, respectively [21]. The results obtained for our sol-gel sample from line broadening analysis of the diffraction lines, according to Scherrer equation [24], indicate that the sizes of HA crystallites are ranged from bellow 10 nm up to 20 nm.

The thermal analysis on sol-gel sample (Fig. 4) shows that all the weight loss take place in two steps below 300°C and above this temperature no more significant weight loss occurs. The first weight loss, well evidenced in DTG curve, is related to an endothermic peak observed in the DTA curve around 270°C and is attributed to the removal of physically adsorbed water. For the next weight loss step, in the DTA curve is revealed an exothermic peak around 320°C that may represent a dehydroxylation reaction [25]. A further inspection of the DTA run shows two other thermal events signalised by a weak exothermic peak around 550°C and a weak endothermic peak around 770°C. They correspond to the similar events observed in the

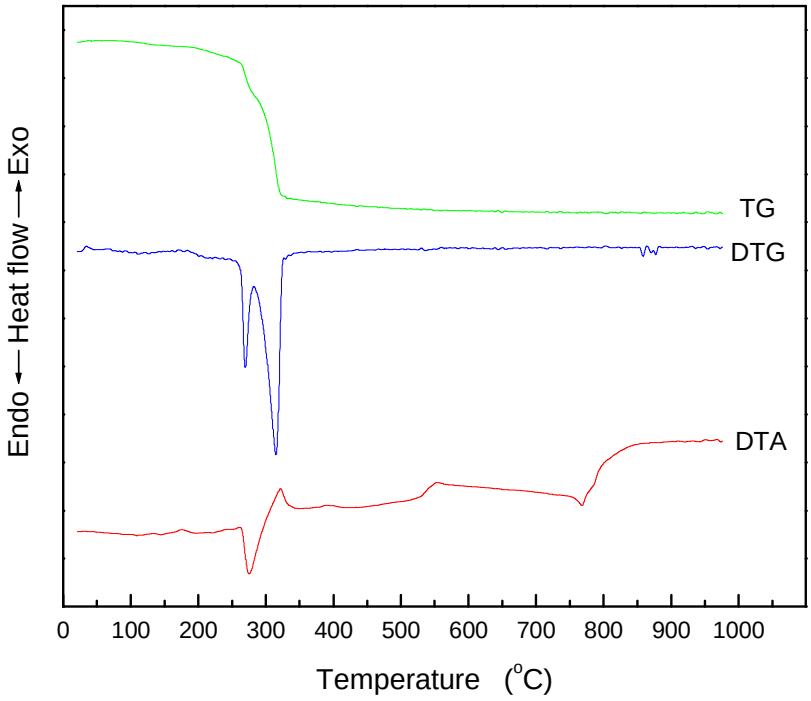

Fig. 4. Thermal analysis curves of the sample prepared by sol-gel method.

hydroxyapatite type sample obtained by melting method (Fig. 2), but in this case the sample prepared by sol-gel method is a nanostructured HA sample in which at the crystallisation temperature the release of heat on crystallisation is small, suggesting that small atomic arrangements of the calcium and phosphate species are required for the achievement of an advanced crystalline structure.

Conclusions

Apatitic calcium phosphates were obtained by heat treatment of a glass precursor and by sol-gel method. The sol-gel route leads to a nanostructured sample with hydroxyapatite nanocrystals sized under 20 nm. DTA analysis indicates that in the sodium-calcium-phosphate glass a crystalline phase of hydroxyapatite type is developed. Similar thermal events are evidenced for the sample prepared by sol-gel method, but in this case the heat release in the thermal region corresponding to crystallisation is much lower because the analysed sample is a nanocrystallised hydroxyapatite.

REFERENCES

1. Y. Wang, S. Zhang, X. Zeng, K. Cheng, M. Qian, We. Weng, Mat. Sci. Eng. C, **27**, 2, 244 (2007)
2. M. Sivakumar, Mater. Lett. 50, 199 (2001)
3. R. Roop Kumar, M. Wang, Mater. Lett. 55, 133 (2002)
4. A. Aoki, Medical Applications of Hydroxyapatite, Ishiyaku Euroamerica Press, Toyoko, 1994.
5. M. Cavalli, G. Gnappi, D. Montenero, P. Bersani, P. Lottici, S. Kaciulis, G. Mattogno, M. Fini, J. Mater. Sci. 36, 3253 (2001)
6. Y. Wang, S. Zhang, X. Zeng, L. L. Ma, W. Weng, W. Yan, M. Qian, Acta Biomaterialia 3, 191 (2007)
7. J. Torrent-Burgues, R. Rodriguez-Clemente, Cryst. Res. Technol., 36, 1075 (2001)
8. P. Layrolle, P. Ito, T. Tateishi, J. Am. Cer. Soc., 81, 1421 (1998)
9. W. Weng, J.L. Babtista, Biomaterials, 19, 125 (1998)
10. A. Lillavenkatesa, R.A. Condrate, J. Mat. Sci., 32, 4111 (1998)
11. D. M. Liu, T. Trosczynski, W.J. Tseng, Biomaterials, 22, 1721 (2001)
12. M. Hsieh, L. Perng, T. Chin, H. Perng, Biomaterials, 22, 2601 (2001)
13. A. Milev, G.S. Kannangara, B. Ben-Nissan, Mat. Lett., 57, 1960 (2002)
14. C.J. Brinker, G.W. Scherer, Sol-Gel Science - The Physics and Chemistry of Sol-Gel Processing, Academic Press, New York, 1990, 2-4.
15. G. Encheva, B. Samuneva, P. Djambaski, E. Kashchieva, D. Paneva, I. Mitov, J. Non-Cryst. Solids, 345&346, 615 (2004)
16. D.A Ward, E.I. Ko, Ind. Eng. Chem. Res., 34, 421 (1996)
17. L.L. Hench, J . Wilson (eds.), An Introduction to Bioceramics, World Scientific, Singapore, 1993, p.142.
18. V.Simon, D. Muresan, S. Simon, Eur. Phys. J. AP, 37, 2, 219-223 (2007)
19. R. Z. LeGeros, in Calcium Phosphates in Oral Biology and Medicine (H. M. Myers, Karger, Basel, 1991) p. 4.
20. S . Q. Wang, L. H. Allen, J. Appl. Phys., 79, 2446 (1996)
21. A.C. Tas, Powder Diffr., 16, 102 (2001)
22. A. C. Tas, F. Aldinger, J. Mat. Sci.: Mat. in Med., 16 167 (2005)
23. K. Katti, P. Gujjula, 15-th ASCE Engineering Mechanics Conference Proceedings, June 2-5, 2002, Columbia University, New York
24. H.P. Klug, L.E. Alexander, X-ray Diffraction Procedures. John Wiley, New York 1954
25. B. Hoghooghi, J. McKittrick, C. Butler, P. Desch, J. Non-Cryst. Solids, 170, 303 (1994)

STUDIA UNIVERSITATIS BABEŞ-BOLYAI, PHYSICA, LIII, 1, 2008

SYNTHESIS AND SURFACE CHARACTERISATION OF BIOMATERIALS FUNCTIONALISED IN PROTEIN ENRICHED SIMULATED BODY FLUIDS

V. SIMON[1], S. SIMON[1], H. MOCUTA[1], E. VANEA[1], M. PRINZ[2], M. NEUMANN[2],

ABSTRACT. Iron containing alumino-silicate systems are investigated as potential biomaterials for hyperthermia. The samples were obtained following a sol-gel route. The X-ray diffraction data show for the heat treated samples the crystallisation of both hematite and magnetite crystals. The Fe 2p core level photoelectron spectrum confirmed the occurrence of iron ions both in Fe^{2+} and Fe^{3+} valence states. The sample surface was functionalised in Kokubo simulated body fluid enriched with bovine serum albumin. The attachment of the protein was proved by X-ray photoelectron spectroscopy.

Keywords. Biomaterials, Synthesis, Body fluid

Introduction

Hyperthermia received renewed interest as non-invasive protocols for cancer treatment and is considered a promising therapy for tumor eradication [1, 2]. Ferrimagnetic biocompatible systems were identified as suitable candidates for hysteresis heating [3, 4]. Having in view that aluminosilicate glass ceramics are highly stable in the body [5], by addition of iron oxide they could be considered for hysteresis heating.

Biocompatibility of a material depends on the manner in which the biomaterial surface interacts with blood components and proteins and on the way in which proteins adsorb on the its surface, because the protein adsorption is the first event happening on the surface of any system implanted in biological environment [6, 7].

The functional properties are mainly determined by the outermost layers of the material [8] and therefore the X-ray photoelectron spectroscopy, as exclusively surface sensitive investigation technique, is a very useful analysis tool for characterisation of materials functionalisation.

This study is focussed on synthesis and surface characterisation of iron containing aluminosilicate samples with respect to proteins uptake from simulated body fluids enriched with bovine serum albumin.

Experimental

Aluminosilicate samples containing iron oxide with $60SiO_2 \cdot 20Al_2O_3 \cdot 20Fe_2O_3$ (mol %) composition were synthesised using as precursors silicic acid, aluminum and iron nitrates of analytical grade purity. The reagents were independently dissolved in distilled water with the assistance of a magnetic stirrer, then they were mixed

[1] *Babes-Bolyai University, Faculty of Physics & Institute for Interdisciplinary Experimental Research, 400084 Cluj-Napoca, Romania*
[2] *University of Osnabrück, Physics Department, 49069 Osnabrück, Germany*

and stirred at a temperature close to 90°C. The mixed solution was allowed to age up to sol-gel formation. After repeated washing and filtering the gel was dried at 110°C and then heat treated at 1200°C in an electric oven.

After fine grinding the powder samples were immersed in simulated body fluid (SBF) prepared according to Kokubo composition [9] and in simulated body fluid enriched with bovine serum albumin (BSA) in two concentrations obtained by adding 0.1 and 0.2 g lyophilised SBA to 30 ml SBF. The samples immersed in simulated biologic media were kept at 37°C in Incutherm RAYPA type incubator for up to seven days, under static conditions.

The X-ray diffraction analysis was carried out on a Shimadzu XRD-6000 diffractometer using CuK_α radiation. Fourier Transform Infrared (FTIR) spectroscopic analysis was conducted with attenuated total reflectance using Equinox 55 Bruker instrument with a resolution of 2 cm^{-1}. X-ray Photoelectron Spectroscopy (XPS) measurements were performed using a PHI 5600ci Multi Technique system with monochromatised Al K_α radiation from a 250 W X-ray source (hν = 1486.6 eV). During the measurements the pressure in the analysis chamber was in the 10^{-9} Torr range. The position and full width at half maximum of photoelectron peaks were determined using spectrum simulation based on summation of Lorentzian and Gaussian functions.

Results and discussion

The X-ray diffraction pattern of the dried sample (Fig. 1a) reveals no crystalline peaks and the large features support a disordered structure. For the heat treated sample (Fig. 1b) both tridymite (SiO_2), aluminosilicate of mullite ($Al_6Si_2O_{13}$) type [10], hematite and magnetite crystals are identified. The mullite structure confers to samples a high structural stability. In the Fe 2p core level spectrum of crystalline sample (Fig. 2) the main peak Fe $2p_{3/2}$ is recorded at an energy of 711.3 eV and the spin-orbit splitting is of 13.6 eV. The broad peaks can be explained by referring to the different valence states, Fe^{2+} and Fe^{3+}, of iron cations in the sample [11].

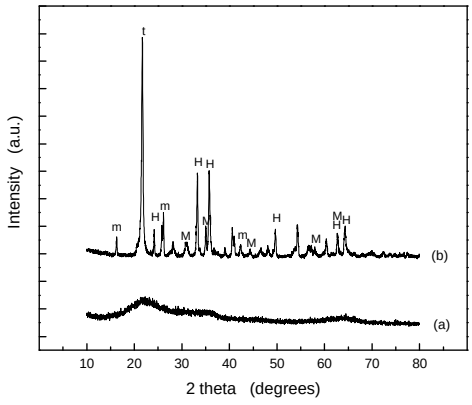

Fig. 1. XRD patterns of (a) as prepared and (b) heat treated samples (t - tridymite, m – mullite, H – hematite and M – magnetite)

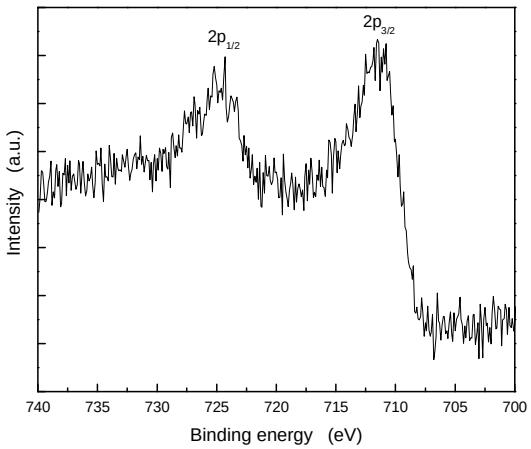

Fig. 2. Fe 2p core level photoelectron spectrum.

The surface functionalisation of the samples after immersion in simulated body fluid was proved by XPS spectroscopy. XPS spectra of lyophilised BSA were also recorded for reference. The presence of carbon is evidenced in all samples (Fig. 3), but carbon adsorption occurs on all surfaces exposed to the atmosphere and is detected by the XPS technique [12, 13]. The occurrence of nitrogen species is clearly evidenced only after immersion in SBF with BSA. In order to evaluate the uptake of protein on samples surface both survey and the C 1s, N 1s and O 1s core level spectra were examed.

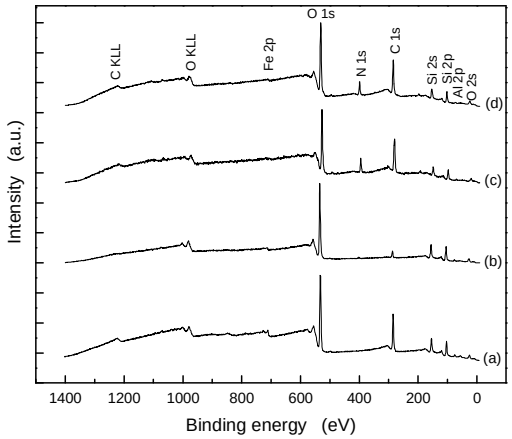

Fig. 3. Widescan XPS spectra before immersion (a), and after one day immersion in SBF (b), SBF enriched with BSA (c) and SBF twice enriched with BSA (d).

The relative content of C, N and O after immersion in SBF solutions, determined from survey XPS spectra (Table 1) points out very close values for both concentrations of BSA in SBF, denoting that the attachment of the protein on the surface of the aluminosilicate sample is saturated even by immersion in the solution with lower BSA content.

Table 1.

Relative percentage of C, N and O after imersion in SBF solutions, determed from survey XPS spectra

BSA concentration in SBF (mg/ml)	%		
	C	N	O
0	19	-	81
3.33	52	11	37
6.67	51	10	39

The C 1s core level spectra recorded from the samples immersed in BSA-SBF solution (Fig. 4) contain the BSA signature even after one day soaking in the SBF solution with low BSA content. The deconvoluted C 1s photoelectron peaks provide more information. From the non-immersed sample only one single C 1s peak at 285.5 eV is recorded. Also after one day immersion in SBF the C 1s photoelectron peak is well fitted with a single line centered at 285.5 eV, but the peak is broadened, with 2.9 eV full width at half maximum (Fig. 4b), while the full width at half maximum for the non-immersed sample (Fig. 4a) is only 2.3 eV. The deconvolution of C 1s photoelectron peaks for the samples immersed in SBF solution enriched with BSA leads beside the peak at 285.5 eV to other two components centered at 286.7 and 288.6 eV, but their relative peak areas are notably different (Table 2). It is beyond doubt that the increased contribution of higher binding energy components is arising from the BSA adhered to the surface of aluminosilicate samples.

Table 2.

Percental distribution of differently binded carbons to C 1s photoelectron peaks according to peak deconvolution.

BSA concentration in SBF (mg/ml)	Binding energy (eV)		
	285.5	286.7	288.6
	Relative peak areas (%)		
3.33	82	13	7
6.67	51	42	5

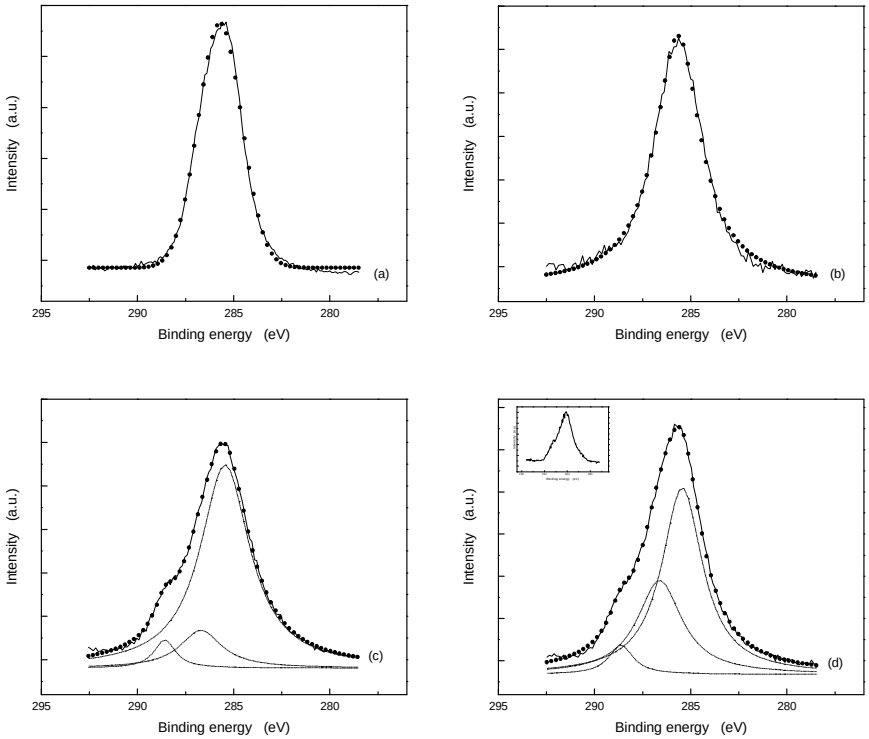

Fig. 4. C 1s corelevel XPS spectra before immersion (a), and after one day immersion in SBF (b), SBF enriched with BSA (c) and SBF twice enriched with BSA (d). In inlay is shown the spectrum recorded from lyophilised SBA.

In a study concerning the adsorption of albumin on prosthetic materials, Serro et al. [14] report that the deconvolution of the C 1s peaks shows three contributions from C-H at 284.7 eV, C-O at 286.0 eV, and C=O at 288.6 eV, before adsorption, while a new contribution attributed to the peptide bond (-CONH-) at 288.1 eV appears after adsorption.

The N 1s photoelectron peak were recoded only for the samples immersed in solutions of SBF with BSA (Fig. 5). The deconvolution of the peaks leads to different contributions for the two components centered at 400.3 eV and 399.1 eV. The binding energies of N 1s typical for organic matrices are close to 400 eV, related to C-N bonds [15]. The atomic percent estimated for nitrogen (8.6 %) is in good agreement with the values reported on the surface of silicon wafers after BSA adsorption [16].

With respect to the evolution of O 1s core level spectra (Fig. 6) one remarks symmetric peaks that are well fitted with a single line, that overlaps the contributions due to the oxygen atoms from the aluminosilicate sample surface,

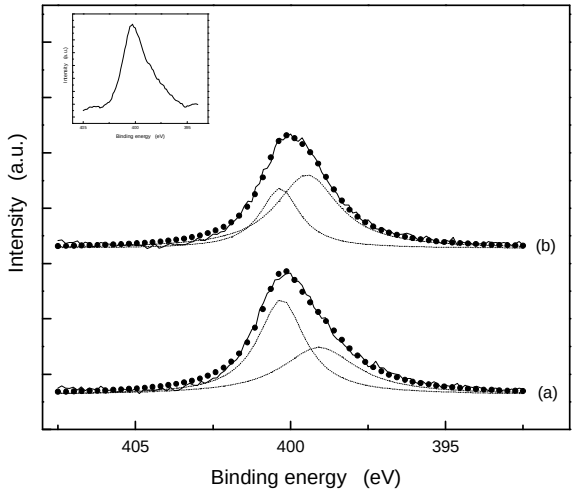

Fig. 5. N 1s corelevel XPS spectra after one day immersion in SBF enriched with BSA (a) and SBF twice enriched with BSA (b). In inlay is shown the spectrum recorded from lyophilised SBA.

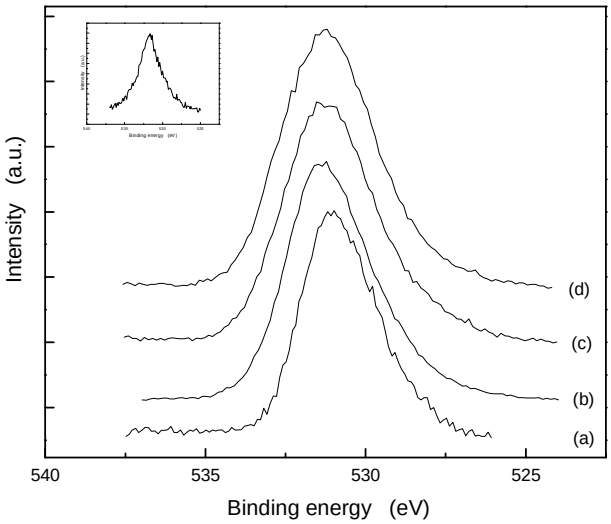

Fig. 6. O 1s corelevel XPS spectra before immersion (a), and after one day immersion in SBF (b), SBF enriched with BSA (c) and SBF twice enriched with BSA (d). In inlay is shown the spectrum recorded from lyophilised SBA.

adsorbed –OH groups and peptidic oxygens of BSA [17]. The full width at half maximum of O 1s photoelectron peak recorded from the non-immersed sample is 2.3 eV and increases to 2.7 eV after immersion in pure SBF and to 2.9 eV after immersion in BSA-SBF, as well in 3.33 and 6.67 mg BSA /1 ml SBF solution. The full width at half maximum determined for the lyophilised BSA used for protein solution preparation is 3.0 eV. One also remarks a shift of O 1s photoelectron peak from 530.8 eV to higher binding energies, 531.1 eV, after immersion in simulated body fluids. The trend in core level binding energy shift for O 1s photoelectrons can be explained by a slight deficiency in electron density around the oxygen atoms by surface functionalisation with protein [18], while the broadening of the full width at half maximum points out a larger distribution of the oxygen sites.

The data obtained from the surface of the samples immersed for longer time in BSA-SBF solutions essentially keep the features recorded after the first day of immersion. BSA adsorption was confirmed by infrared data only for the samples immersed for few days in BSA enriched simulated body fluid, while the XPS results evidences the protein adsorption already after the first day of immersion. This fact was also reported for BSA adsorption on the surface of polymer samples [17]. XPS spectroscopy clearly appears more sensitive than FTIR performed in reflectance mode to the changes occurred on the sample surface after immersion in simulated body fluids.

Conclusions

XRD and XPS data were used to analyse the structure and attachment of BSA on iron containing aluminosilicate samples. The development of ferrimagnetic phase evidenced in XRD pattern by magnetit crystals is correlated with the presence of Fe^{2+} and Fe^{3+} ions in the heat treated sample. The relative atomic concentrations of C, N and O identified after immersion in BSA solutions suggests that the surface is nearly saturated in taking up BSA functional groups regardless of BSA concentration in SBF. The evolution of the C 1s and N 1s core level XPS spectra, appreciated from the contributions of different components to the deconvoluted peaks, shows that the protein concentration in SBF influences the building up of the BSA layer. Surface functionalisation with protein leads to a larger distribution of the oxygen sites and a slight deficiency in electron density around the oxygen atoms.

Acknowledgment

The authors from Babes-Bolyai University acknowledge support from the Romanian Excellence Research Program for research project CEEX 100/2006 – MATNANTECH.

REFERENCES

1. H. Gu, K. Xu, Z. Yang, C.K. Chang , B. Xu, Chem. Commun., 34, 4270 (2005)
2. K.A. Gross, R. Jackson, J.D. Cashion, L.M. Rodriguez-Lorenzo, Eur. Cell Mater., 3S2, 114 (2002)
3. M. Kawashita, H. Takaoka, T. Kokubo, T. Yao, S. Hamada, T. Shinjo, J. Ceram. Soc. Jpn., 109, 39 (2001)
4. Y. Ebisawa, V. Miyaji, T. Kokubo, K. Ohura, T. Nakamura, Biomaterials, 18, 1277 (1997)
5. G.J. Ehrhardt, D.E. Day, Nucl. Med. Biol., 14, 233 (1987)
6. K. Vijayanand, D.K. Pattanayak, T.R. Rama Mohan, R. Banerjee, Trends Biomater. Artif. Organs, 18, 73 (2005)
7. F. Rossi, A. Valsesia, M. Manso, G. Ceccone, P. Colpo, Micro- and Nano-Structured Thin Films for Biological Interfaces. NATO Science Series, 155, 285 (2006)
8. A. Rossi, B. Elsener, N.D. Spencer, Spectr. Eur., 6, 14 (2004)
9. T. Kokubo, H. Kushitani, S. Sakka, T. Kitsugi, T. Yamamuro, J. Biomed. Mater. Res., 24, 721 (1990)
10. P. Hou, S.N. Basu, V.K. Sarin, J. Mater. Res., 14, 2952 (1999)
11. Y.X. Lu, J.S. Claydon, E. Ahmad, Y.B. Xu, M. Ali, B.J. Hickey, S.M. Thompson, J.A.D. Matthew, K. Wilson, J. Appl. Phys., 97, 10C313 (2005)
12. T. Taylor Eighmy, A.E. Kinner, E.L. Shaw, J. Jr. Dykstra Eusden, C.A. Francis, Surf. Sci. Spectra, 6, 193 (1999)
13. M.H. Prado da Silva, G.A. Soares, C.N. Elias, J.H.C. Lima, H. Schechtman, I.R. Gibson, S.M. Best, Mat. Res., 3, 61 (2000)
14. A.P. Serro, M.P. Gispert, M.C.L. Martins, P. Brogueira, R. Colaco, B. Saramago, J. Biomed. Mater. Res., 78A, 581 (2006)
15. M. Advincula, X. Fan, J. Lemons, R. Advincula, Colloid Surface B: Biointerfaces, 42, 29 (2005)
16. F. Zhang, R.J. Gates, V.S. Smentkowski, S. Natarajan, B.K. Gale, R.K. Watt, M.C. Asplund, M.R. Linford, J. Am. Chem. Soc., 129, 9252 (2007)
17. G. Iucci, G. Polzonetti, G. Infante, L. Rossi, Surf. Interface Anal., 36, 724 (2004)
18. V. Simon, D. Muresan, A.F. Takács, M. Neumann, S. Simon, Solid State Ionics, 178, 221 (2007).

STUDIA UNIVERSITATIS BABEŞ-BOLYAI, PHYSICA, LIII, 1, 2008

FRIEDEL OSCILLATIONS IN ONE-DIMENSION: MANY IMPURITIES AND BIAS VOLTAGE EFFECTS

L. TUGULAN*

ABSTRACT. Using the linear response theory we studied the Friedel oscillations in a one-dimensional noninteracting electron gas in the presence of impurities. The impurities potential is assumed to have periodic delta-function and square-well form. The particular cases of a single impurity, two and three impurities are also analyzed. The oscillations are strongly affected by the distance between impurities. The effect of the bias voltage on the Friedel oscillations in a wire with one impurity, coupled to macroscopic electrodes, is also analyzed.

Keywords: One-dimensional electron gas, Many impurities, Short-range interactions, Friedel oscillations, Single impurity, Two impurities, Three impurities, Bias voltage effects.

1. Introduction

The problem of the Friedel oscillations in a one-dimensional noninteracting gas, in the presence of a static impurity, was recently analyzed by Giuliani et al. [1] in order to give a correct analytical description of the induced density modulation. They pointed out that the original calculation [2] gave an incorrect answer. The model adopted in Ref.1 is based on the theory of linear response [3], and the impurity potential is assumed to be of the delta-function form. However, the simple delta-function potential (zero range potential) lacks one important feature that characterizes potentials, namely, the characteristic range and, as a consequence, the possibility of resonances [4]. A simple modification which introduces a finite range is a two-delta functions potential (two delta functions separated by a finite distance), which will be considered in this paper. This case will be a particular situation of the general result for the n-impurities case. Another modification is the periodic square-well model we will also consider in this paper. The importance of the Friedel oscillations was pointed out by Simon and Giuliani [5] in connection between their theoretical results and the scanning tunneling microscopy measurements. A two dimensional model, with inelastic scattering centers, was proposed by Fransson and Balatsky [6], in connection to the scanning technique, in order to visualize the oscillations in the inelastic scattering produced by the local vibrational modes of the molecules on the surface. Another important effect of the Friedel oscillations was discussed by Zhitomirsky and Walker [7] in connection to the transition temperature in impure superconductors. More recently, the problem of the Friedel oscillations was discussed in nanostructures [8], and for the case of a quantum dot coupled to an edge of a disordered one dimensional wire [9]. Often, the models proposed to study various

* *Department of Theoretical Physics, University of Cluj, 3400 Cluj, Romania*

properties of the quantum dots systems does not take into consideration the density oscillations effects. Recently, the problem of the Friedel oscillations in the presence of the transport currents was considered by Gorczyca et. al. [10].Other important aspects of the Friedel oscillations, in the Kondo model, were pointed by Affleck et.al. [11], and for nanotubes systems, by Chaplik et.al. [12]. Motivated by these important aspects, we will analyze the problem of the Friedel oscillations in one dimension in the presence of the impurities and the bias voltage. The obtained results are an extension and generalization of the results obtained in Refs. [13, 14].

2. Model

2.1. Periodic delta-function model

In the following, we will consider the problem of the Friedel oscillations in the one-dimensional noninteracting electron gas and in the presence of the impurities. The impurities potential will be assumed of the form:

$$V_{ext}(x) = C\left[\delta(x) + \delta(x-a) + \delta(x-2a) + ... + \delta(x-na)\right] \tag{1}$$

where C is a constant that measures the strength of the potential, and a is the distance between the adjacent impurities. In order to find the dependence of the distance of the density, we will use the linear response theory (as in Refs.[1,3]). This dependence is given by:

$$n(x) = \int_0^\infty \frac{dq}{\pi} \chi(q) V_{ext}(q) \cos(qx) \tag{2}$$

Here $\chi(q)$ is the static Lindhard function in one dimension ($\hbar$=1):

$$\chi(q) = \frac{2m}{\pi \cdot q} \ln\left|\frac{2k_F + q}{2k_F - q}\right| \tag{3}$$

(m-is the electron mass, and k_F - the Fermi wavevector). $V_{ext}(q)$ is the Fourier transform of the impurities potential:

$$V_{ext}(q) = C\sum_{k=0}^{n} cos(k \cdot qa) \tag{4}$$

Using Eqs.(3) and (4) in Eq.(2), and the new variable, $y = q/2k_F$, we find:

$$n(x) = \frac{2mC}{\pi^2} \sum_{k=0}^{n} \int_0^\infty \frac{dy}{y} \cdot \ln\left|\frac{1+y}{1-y}\right| \cdot \cos(2k_F xy) \cdot \cos(k \cdot 2k_F ay) \tag{5}$$

With the help of the integral [15]:

$$\int_0^\infty \frac{dy}{y}\cdot \ln\left(\frac{b+y}{b-y}\right)^2 \cdot \cos(ay) = -2\pi \cdot si(ab), a>0, b>0 \tag{6}$$

(where *si(x)* is the shifted sine-integral function), we obtain the following result:

$$n(x) = -\frac{mC}{\pi}\sum_{k=0}^{n}\{si[2k_F(x+ka)]+si[2k_F(x-ka]\}, x>ka \tag{7}$$

In the case of a single impurity, with $V_{ext}(x) = C\delta(x)$, the result is given by [1] (or by Eq.(7) with *k=0*) :

$$n(x) = -\frac{2mC}{\pi}\cdot si(2k_F x) \tag{8}$$

The large distance behavior in Eq.(7) can be obtained using the asymptotic behavior:

$$si(x) \sim -\frac{\cos(x)}{x} \tag{9}$$

and we have:

$$n(x) \cong \frac{mC}{\pi\cdot k_F x}\left[\cos(2k_F x)\cdot S_1 + \frac{a}{x}\cdot\sin(2k_F x)\cdot S_2\right] \tag{10}$$

where:

$$S_1 = \sum_{k=0}^{n}\cos(k\cdot 2k_F a) \tag{11}$$

and:

$$S_2 = \sum_{k=0}^{n} k\cdot\sin(k\cdot 2k_F a) \tag{12}$$

For *k=0*, we have the case of a single impurity in the origin, for which we have: $S_1 = 1$ and $S_2 = 0$, and:

$$n(x) \cong \frac{mC}{\pi\cdot k_F x}\cdot\cos(2k_F x) \tag{13}$$

For a chain of impurities, S_1 and S_2 are given by (see Ref.[15]):

$$S_1 = 1 + \cos\left[(n+1)k_F a\right] \cdot \sin\left(nk_F a\right) \cdot \cos ec\left(k_F a\right) \tag{14}$$

and:

$$S_2 = \frac{\sin\left[(n+1)\cdot 2k_F a\right]}{4\cdot \sin^2(k_F a)} - \frac{(n+1)\cdot \cos\left[(2n+1)\cdot k_F a\right]}{2\cdot \sin\left(k_F a\right)} \tag{15}$$

Several transparent results can be obtained for the case of two impurities, when *k=0, 1* (and *n=1*). In this case, S_1 and S_2 are easy evaluated and given by:

$$S_1 = 1 + \cos\left(2k_F a\right) \tag{16}$$

and:

$$S_2 = \sin\left(2k_F a\right) \tag{17}$$

The distance dependence of the density will be:

$$n(x) \cong \frac{mC}{\pi \cdot k_F}\left\{\left[1+\cos\left(2k_F a\right)\right]\cdot \frac{\cos\left(2k_F x\right)}{x} + a\cdot \sin\left(2k_F a\right)\cdot \frac{\sin\left(2k_F x\right)}{x^2}\right\} \tag{18}$$

In Figs.1-2 we plot the large distances dependence of the normalized density $R = n(x)/(mC/\pi k_F)$ for both (single and two impurities) cases, for different values of the product $2k_F a$ (we take $2k_F = 1$). The presence of the second impurity can affect drastically the density oscillations (changing the positions and the amplitudes of the maxima and the minima, depending on the distance between impurities, see Fig.2).

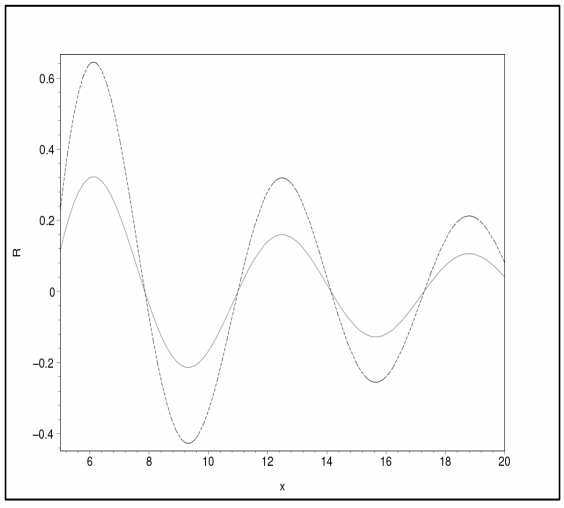

Fig.1. Distance dependence of the normalized density *R* for $2k_F a = 0$, ($2k_F = 1$) , and for: a) one impurity (solid line), b) two impurities (dashed line)

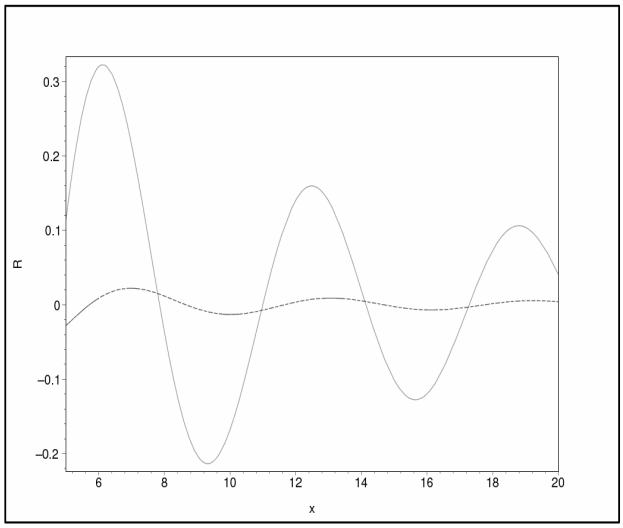

Fig.2. Distance dependence of the normalized density *R* for $2k_F a = 0.9 \cdot \pi$, ($2k_F = 1$), and for: a) one impurity (solid line), b) two impurities (dashed line)

This behavior is due to the interference effects induced by impurities. For very large distances, and for $2k_F a = (2m+1)\pi$, (*m* – integer) there are no density oscillations in the system.

2.2. Periodic square-well potential

In this case we assume a periodic square-well potential. The length and the distance between the adjacent square-wells is considered to be *l*. The model potential is given by:

$$V_{ext}(x) = \begin{cases} C_1; x \in [0,l] \cup [2l,3l] \cup ... \\ 0; otherwise \end{cases} \tag{19}$$

The Fourier transform of the potential is:

$$V_{ext}(q) = \frac{C_1}{q} \sum_{k=1}^{n} \{\sin[(2k-1)ql] - \sin[2(k-1)ql]\} \tag{20}$$

where n – is the number of the square-wells. Using the Eqs.(2-3) and (20), the distance dependence of the density, for large distances, will be:

$$n(x) \cong \frac{mC_1}{\pi \cdot k_F} \cdot \frac{\cos(2k_F x)}{2k_F x} \left\{ 2\left[1 + \frac{\tan(2k_F x)}{2k_F x} \right] \sin(k_F l) \cdot S_3 - \frac{l}{x} \tan(2k_F x) \cdot S_4 \right\} \tag{21}$$

where:

$$S_3 = \sum_{k=1}^{n} f_1(k) \tag{22}$$

$$S_4 = \sum_{k=1}^{n} f_2(k) \tag{23}$$

and:

$$f_1(k) = \cos\left[(4k-3)k_F l\right] \tag{24}$$

$$f_2(k) = 2\cdot\cos\left[(2k-2)2k_F l\right] - \cos\left[(2k-1)2k_F l\right] - 4k\cdot\sin(k_F l)\cdot\sin\left[(4k-3)k_F l\right] \tag{25}$$

In Fig.3 we plot the large distance behavior of the normalized density $R1 = n(x)/(mC_1/\pi\cdot k_F)$, for the square-well model, for two and for three impurities (for $k_F l = 2$ and $2k_F = 1$).

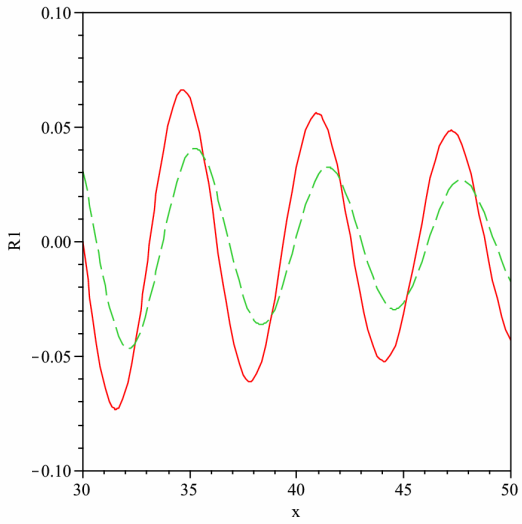

Fig.3. Distance dependence of the normalized density R1, for the square-well model, for $k_F l = 2$ and $2k_F = 1$, and for: a) two impurities (solid line), b) three impurities (dashed line)

2.3. The bias voltage effect

In this section we will analyze the electron density oscillations in a wire coupled to two electrodes at different potentials, in the presence of one impurity. The impurity potential is considered to have a non-Coulomb form:

$$V_{ext} \propto \frac{1}{x^{1+\alpha}}, 0 < \alpha < 1 \tag{26}$$

with the Fourier transform given by:

$$V_{ext}(q) = C \cdot q^{\alpha} \tag{27}$$

where C – is a constant. In the presence of a small bias voltage V the form of the Lindhard function (3) changes, due to the shift of the Fermi wave-vector, to:

$$\chi(q,V) = \frac{2m}{\pi q} \cdot \ln\left|\frac{1+q/2k_F - bV}{1-q/2k_F + bV}\right| \tag{28}$$

(b – is a constant). Using Eq.(2), and $y = q/2k_F$, we find:

$$\frac{n(x,V)}{(mC/\pi^2(2k_F)^{-\alpha})} = \int_0^{\infty} \frac{dy}{y^{1-\alpha}} \cdot \ln\left(\frac{1+y-bV}{1-y+bV}\right)^2 \cdot \cos(2k_F x \cdot y) \tag{29}$$

In Fig. 4 we plot the distance dependence of the ratio from Eq.(29), for $V = 0$, and for small V.

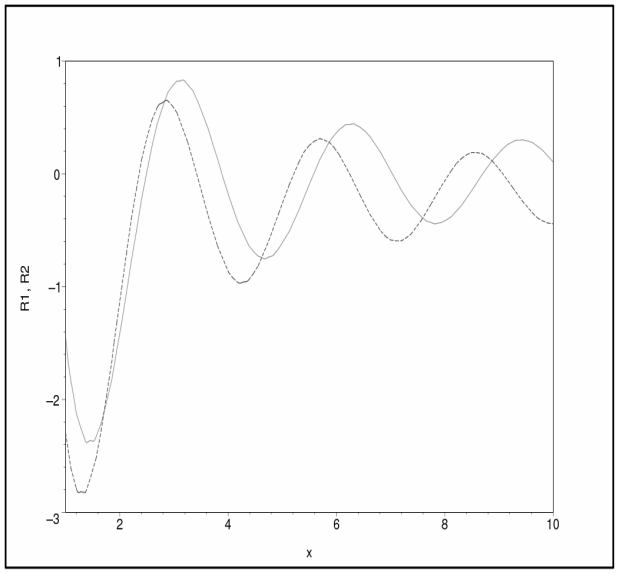

Fig.4. Distance dependence of the ratio from Eq.(29), for $V = 0$, (R1 – solid line), and for small V (R2 – dashed line) . The parameters we used here are: $k_F = 1$, $bV = 0.1$, $\alpha = 0.5$

We see that the bias voltage affect the electron density oscillations . The wave-length of the density oscillations changes with the bias voltage, whereas the amplitude and the spatial decay exponent of the oscillations seems to remain unchanged.

3. Conclusions

In conclusion, we studied the problem of the Friedel oscillations in one dimension and in the presence of the localized static impurities and the bias voltage. Due to the interference effects, the intermediate and large distance oscillations are strongly affected by the distance between impurities. A similar result was reported by Liu [16] for the case of two impurities in an interacting one-dimensional system. The electron-electron interaction and the impurity strength also affect the oscillations decay. For an arbitrary impurity strength, in the Luttinger liquid model, it was shown, [17], that the oscillations decay as x^{-g} (away from the impurity), where g is the interaction constant. The behavior of the Friedel oscillations could be of interest in the study of the transition temperatures of some superconductors [18]. For the low dimensional superconductors, in the presence of the impurities, it was pointed out that the density variations near the impurity sites becomes important, for short coherence length superconductors, and can increase the transition temperature in the case of the s-wave superconductors [7]. The model we study here, even for the simple periodic delta-function and square-well structure, reveal the importance of the effect of the density oscillations (through the distance dependence and the interference effects), that could affect the physical properties of the quantum dots systems. For this case, a more realistic treatment should include the bias voltage effect. We showed that the bias voltage affect the density oscillations. Even for a very simple model we obtained , analytically, several results that are in agreement with the results obtained in Ref.[10], where the non-equilibrium Keldysh-Green functions method is used.

REFERENCES

1. G.F.Giuliani, G.Vignale, T.Datta, Phys.Rev.B 72, 033411, (2005)
2. C.Kittel, "Solid State Physics", vol.22, edited by F.Seitz, D.Turnbull and H. Ehreinreich, Academic Press, New York, (1968)
3. G.E.Giuliani, G.Vignale, "Quantum Theory of the Electron Liquid", Cambridge University Press, Cambridge, (2005)
4. H.J.Lipkin, "Quantum mechanics", North-Holland, (1973)
5. G.E.Simon, G.F.Giuliani, Phys.Rev.B 72, 045127, (2005)
6. J.Fransson, A.V.Balatsky, Phys.Rev.B 75, 195337, (2007)
7. M.E.Zhitomirsky, M.B.Walker, Phys.Rev.Lett.80, 5413, (1998)

8. Y.Hasegawa, M.Ono, Y.Nishigata, T.Nishio, T.Eguchi, J.Phys: Conf. Series 61, 399, (2007)
9. Y.Weiss, M.Goldstein, R.Berkovits, arXiv: 0704.1386 (cond-mat.)
10. A. Gorczyca, M.M.Maska, M.Mierzejewski, Phys.Rev.B 76, 165419, (2007)
11. I.Affleck, L.Borda, H.Saleur, Phys.Rev.B 77, 180404(R), (2008)
12. A.V.Chaplik, L.I. Magarill, R.Z. Vitlina, arXiv: 0712.0878 (cond-mat.)
13. I.Grosu, L.Tugulan, J.Supercond.Nov.Magn. 21, 65, (2008)
14. I.Grosu, L.Tugulan, Studia-Physica LII, 2, 79, (2007)
15. I.S.Gradshteyn, I.M.Ryzhik, "Table of integrals, series, and products", Academic Press, (1980)
16. Y.L.Liu, Phys.Rev.B 68, 155116, (2003)
17. R.Egger, H.Grabert, Phys.Rev.Lett. 75, 3505, (1995)
18. A.L.Fetter, Phys.Rev.140, A1921, (1965)

STUDIA UNIVERSITATIS BABEŞ-BOLYAI, PHYSICA, LIII, 1, 2008

AUTOMATION OF PLASMA DIAGNOSTICS MEASUREMENTS PERFORMED IN A NON-ISOTHERM PLASMA REACTOR

KENÉZ L., ZSAKÓ Z., FILEP E.*

ABSTRACT. At the basis of this work stands an issue demanded by physicists working in ion source research, namely the diagnostics research of the plasmas of different ion sources. Plasmas are difficult to study, but knowledge regarding the parameters of plasmas and their evolution during operation is important to understand and amend the ion source and ion beam parameters. The aim of this work was to design a fully automated local plasma diagnostics system to measure the voltage-current characteristics of a Langmuir-probe.

Keywords. Ion plasma, Plasma diagnostics, Voltage-current characteristics

1. Introduction

Plasma nitriding is an environment friendly technology, which increases the surface hardness, wear resistance and sliding properties of machinery components in such manner that it must be considered as value increasing technology.

The treated component as a matter of fact is the cathode of a gas discharge, while the anode is the recipient where the discharge takes place. The treatment of alloyed steel components can take place in 100-200 Pa pressure nitrogen-hydrogen gas mixture, at maximum 800 K temperature. The treatment period normally spans from 2 to 24 hours. During treatment, on the surface of the steel component a 4-5 micron thick Fe_4N, γ' crystal structure chemical compound layer grows. Beneath this layer there is a diffusion layer, in which the nitrogen density exponentially decreases. The thickness of the chemical compound layer doesn't depend on the treatment time, but it can be influenced controlling the discharge parameters. The thickness of the diffusion layer (in concordance to the theory) increases exponentially increasing the temperature and by the by square of the treatment time.

In contrast to the laboratory equipment, in case of industrial apparatus the anode surface is much larger than the cathode surface, thus the current density is much lower by the anode surface and, according to the observation of the emitted visible light, it is inhomogeneous.

From technical point of view, plasma nitriding therein differs from nitriding in normal pressure gaseous ammonia that nitrogen exploitation is at least two magnitudes higher, which cannot be explained without taking into account the processes going on in the gas discharge. Although processes taking place in the gas discharge have been studied by numerous authors [1,14], there is no solid explanation of the nitriding mechanism. This is the motivation for the further investigations.

* *Sapientia Hungarian University of Transylvania, Târgu-Mureş / Corunca, RO-540485, Şos. Sighişoarei Nr. 1C, Romania*

The first model (1965) is based on cathode sputtering [1,2]. It was observed that any solid surface near the cathode (2-5 cm range) is covered with FeN during the nitriding process (e.g. the surface aluminum-oxide insulation of the thermocouple. It was assumed that the FeN molecule is formed in the Aston dark space region close to the negative glow region. The FeN molecules with 50-50% probability diffuse from this region toward the treated surface or the anode, condense than decay according to the process below:

$$FeN \rightarrow Fe_{2-3}N \rightarrow Fe_4N \,.$$

In this process the disengaged nitrogen is transmitted to the treated surface.

The model based on ion bombardment [3], (Hudis, 1973) assumes, the NH^+ and NH_2^+ ions formed in the discharge area transport the nitrogen from the plasma to the treated surface. After colliding with the surface these molecules dissociate. Although, there are proves that presence of hydrogen in the nitriding process is very useful, it was shown that nitriding can be carried out also in hydrogen free N_2 - A_r environment [14,20]. On the other hand an other author showed [4], (Tibbets, 1974) that plasma nitriding is also possible when positive ions are reflected using a biased grid. Hence, Tibbets assumed that nitrogen carriers could be the fast, neutral atoms formed by resonant charge transfer.

Raman spectroscopy investigations showed, that N and N_2 molecules excited to low energy levels are the most active form nitrogen transfer point of view. Hence, Michel (1995) [11], propose to reject the cathode sputtering based model proposed by Kölbel in 1965.

In 1999 J. Georges patented the TC (through cage) or AS (active screen) method. In this method the treated components are on floating potential (or only slightly biased to prevent discharges on the component's surface). Inside the vacuum recipient there is a cathode made of a net or a pitted slab placed parallel to the recipient wall. The components to be treated are placed in the center of the recipient, properly insulated both from the cathode and the anode (recipient) of the discharge. Heating of the components is assured by radiation heat transfer. In such conditions ion bombardment can be excluded, and the movement of the excited neutrals is also inadequate for nitriding. Hence Li and Bell in return to the cathode sputtering model in 2000.

It is known, that due to collision of positive ions and fast neutral atom into the cathode of the gas discharge, primary electrons (with energies exceeding 100 eV-s) are released from the cathode. The primary electrons colliding with ions or neutral atoms, give birth to secondary electrons (with 10 eV magnitude energies) than to 1 eV magnitude energy residual electrons in the negative glow region. We assume that the energy of the residual electrons is enough to give birth to the nitrogen transporter molecules which present N and N_2 in excited to some vibration levels. The aim of this paper is to investigate the energy (electron temperature) and density of the residual electrons in the discharge region of an industrial plasma-nitriding apparatus.

Due to the numerous parameter which characterize the process, it is important to analyze the theoretical models [10] taking into account the electron temperature and charge carrier density. These quantities are related and dependent on the specific aspects of gas mixture, pressure conditions and electrical parameters of the different apparatus.

2. The NITRION-10M plasma nitriding equipment

We studied the negative glow region of the glow discharge in industrial conditions using the NITRION-10 M plasma nitriding equipment described in [5]. The dimensions of the cylindrical discharge chamber: $\Phi 500\, x 2000\ mm$. The discharge is sustained by a full-wave rectified, not smoothened power supply. The discharge voltage can be continuously controlled between 500 and 1000 V. The chamber wall and the double screening cylinder mounted inside the chamber was grounded, these are the anode of the discharge, while the cathode was mounted axially in vertical position on top of the discharge chamber. The top of the chamber was provided with gas inlet, quick refill inlet and three symmetrically positioned feedthrouh for usable for different purposes. Through one of these was introduced the Langmuir-probe.

3. Local diagnostics of the non-isotherm plasma

3.1. The Langmuir-probe

As Langmuir-probe we used a cylindrical cromel-alumel thermocouple, mounted in a quartz insulator tube so the active collector region was a 25 mm long and 3 mm diameter cylinder (active surface of the probe $2\ cm^2$). The thermocouple rod was properly insulated from electrical point of view and introduced in a fixed position in the vacuum chamber through a vacuum using a vacuum feedthrough. The probe and the feedthrough are presented in Fig. 1.

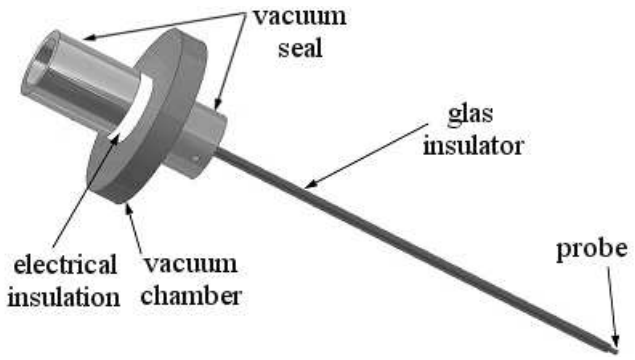

Fig. 1. Probe assembly with electrical insulation and vacuum seal

To prevent electrical conduction between the probe and the insulator tube due to contamination with material sputtered from the cathode, there was a 0,5 mm distance between the thermocouple (probe rod) surface and the quartz insulator tube [15,18]. The outer wall of the thermocouple was stainless steel, which was in contact with the plasma. The probe was in vertical position, mounted parallel to the cylindrical symmetry cathode mounted on the symmetry axis of the discharge chamber (which is the anode of the discharge). Before measurements, the probe was properly degreased than cleaned using high electron and ion currents collected from the plasma. The probe bias voltage could be manually varied between +100 and -100 V with respect to the anode potential [18] (the anode of the discharge was grounded). Data analysis was carried out using models described in [15,18].

3.2. Measurements and results

A typical probe voltage-current curve is presented in Fig. 2. The shape of the curve is identical to ones presented in numerous places in the literature. Difference can be observed in the high positive potential region where the probe is glowing due to electron bombardment (15,40 V region). However, this region cannot be used to plasma parameter calculation, it is important from plasma nitriding point of view.

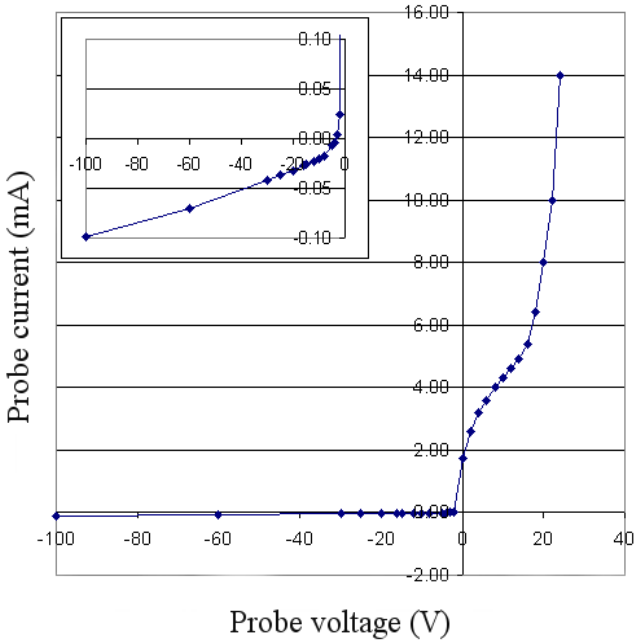

Fig. 2. Probe voltage current curve: probe dimensions $\Phi 3x25\ mm$, (-100,-30 V): ion current region, (-30, 0 V): retarding potential region, (0, 15 V): saturation electron current region, (15,40 V): glowing probe.

The probe curves were analyzed using a traditional method. The curve in the ion current region is linear. In the transition region the probe collects both ions and electrons. In order to calculate the electron component of the current in the transition region, the ion current region is fitted using a linear function, then it is extrapolated to the transition region and it is extracted from the total current. Than the natural logarithm of the electron current is calculated. The obtained result is presented in Fig. 3.

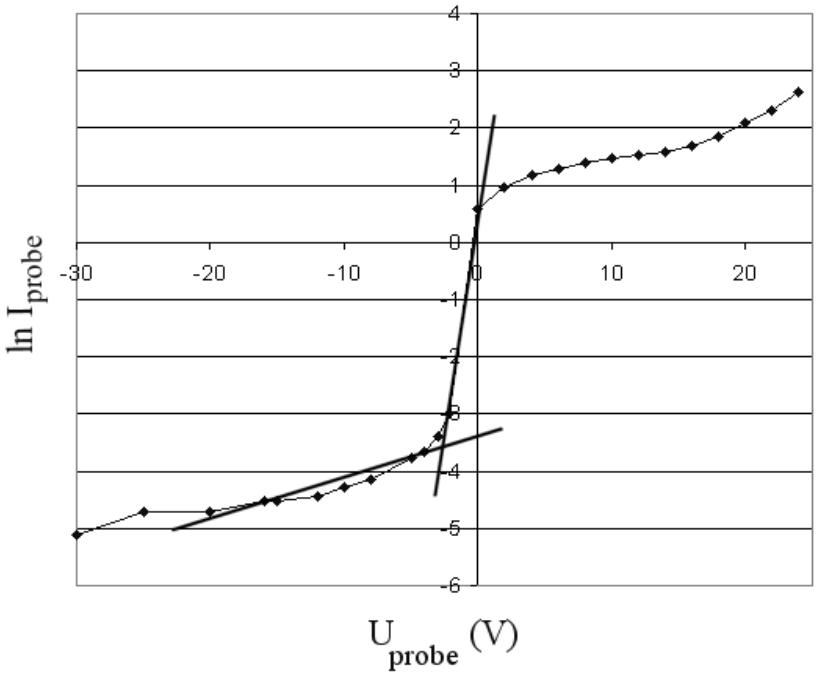

Fig. 3. Logarithm of the electron current and linear fit of the retarding potential region

According to the shape of the curves presented in Fig. 2 and 6., the velocity distribution of the electrons in the studied gas-mixture – pressure – current density region are Maxwell-Boltzmann type. One can see in Fig. 6, that the curve presents two different slope linear region in the retarding potential region. This means that there are two electron populations with different electron temperatures. This type of two different average temperature electron distribution is characteristic to the anomalous DC gas discharge [15,18], but it is not present in case of arc discharge [19]. Fitting the linear regions of the curves, the plasma potential, electron density, electron temperature as well as the floating potential can be determined. The results are presented in Table 1.

Table 1.

p	torr	0,05	0,1	0,1	0,1	0,1	0,5
$T_{cathode}$	K	293	303	353	400	400	543
V_{plasma}	V	0	0	0	0	0	0
$V_{floating}$	V	-3	-3	-4.9	-5	-5	-11
I_{e_0}	mA	0,087	0,152	1,724	2,353	2,64	4,25
j_{e_0}	A/m^2	0,43	0,751	8,62	11,78	13,2	21,25
$c_{e_0}({}^1T_e)$	m/s	5,23*10^5	4,48*10^5	7,45*10^5	6,89*10^5	6,24*10^5	9,21*10^5
${}^1T_e$	K	7,0*10^3	5,2*10^3	14,4*10^3	12,3*10^3	10,1*10^3	22*10^3
${}^2T_e$	K	32,5*10^3	72,3*10^3	48*10^3	141*10^3	33,1*10^3	310*10^3
n_{e_0}	10^{14}/m^3	0,21	0,42	2,9	4,27	5,29	5,77

The plasma potential near the probe irrespectively to the discharge parameters was practically zero. The positive glow region in the N_2 + H_2 gas mixture used for plasma nitriding was missing [2]. Decreasing the current density the floating potential, the electron density (n_{e_0}) and the electron temperature also decreased. The obtained $5 * 10^{14}$ *electron / cm*^{3} density corresponds to a low 10^{-7} ionization grade. Increasing the pressure and the current density this value can be further increased, while the cathode can reach *800 K* temperature. These are relative data, because at constant pressure, the density distribution depends on the temperature distribution.

The density of the lower energy (${}^1T_e$) electron population is at least on magnitude higher (Fig. 3). Hence, only this electron population was considered at the calculations of the electron density. Due to the obtained electron temperature, the energy of the electrons is one magnitude higher than the thermal energy. From chemical reaction point of view, the lower density ${}^2T_e$ electron temperature population, this has important role in the negative glow region of the discharge. The energy of these electrons exceeds the ionization energy. Although the pressure is relative high, according to the measurements they can get in the anode region too.

We could not reveal the presence of the primary electrons which gain in the cathode dark space of the glow discharge more than *100 eV* energy.

4. Automated measurements of the non-isotherm plasma

4.1. The experimental setup

We used the same probe setup described in Section 3.1. (Fig. 1), but instead of the cromel-alumel thermocouple, we used a stainless steel rod, and the active collector region of the probe was 3 mm long and 1,5 mm diameter.

Fig. 4. presents the block diagram of the automated plasma diagnostics data acquisition system. The cathode is on the symmetry axis of the reactor. The cylindrical plasma reactor body is grounded, and the cathode is biased to negative voltages with respect to the body. The probe inside the non-isotherm plasma reactor is positioned off-axis, parallel to the cathode. The positioning of the probe is important. Due to the cylindrical symmetry of the electrical field inside the chamber, an off-axis probe positioned parallel to the cathode surface is in homogeneous field. The automated measuring system contained: a so-called VS-100 unit to bias the probe, a so-called CM-10 unit to measure the probe current (both designed and built in the university), an Advantech multifunction data acquisition board and a personal computer.

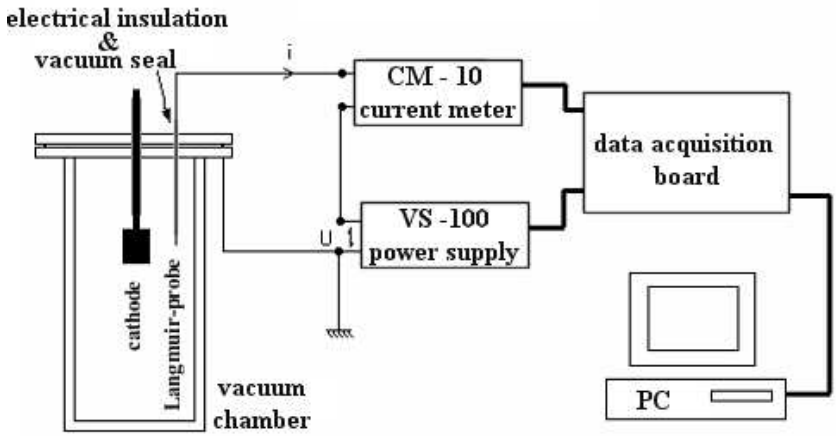

Fig. 4. Block diagram of the data acquisition system

4.2. The VS-100 power supply

There are some requirements regarding the power supply that must be fulfilled. To measure the whole voltage-current curve of the Langmuir-probe, the power supply must be capable to bias the probe both to the negative and positive voltages with respect to the grounded body of the plasma reactor. Hence the data collection is PC-controlled, the power supply must be capable to switch automatically the polarity when reaching the ground potential. Due to the specific behavior of a probe voltage-current curve, the power supply must be capable of working as a load when current flows from the probe to the power supply (probe voltage in the f (floating potential), 0V range) assuring correct bias voltage for the probe.

The output voltage of the VS-100 power supply is designed to be variable in the -100 and 100 V range, it is properly stabilized, with a maximum output current up to 10 mA. The controlling of the power supply is done using a 0-5 V range analog signal and a 0/5 V digital signal. The first one controls the output voltage, the second one the polarity of the output voltage.

4.3. The CM-10 current meter.

The current measurement is difficult due to the wide range of the collected current, and the specific features of the plasma discharge. The CM-10 current meter assures automatic current measurement (using micro-controller built in the current measurement unit) switching over four magnitude range of the 0-10 mA current range as follows: 0 ÷ 10μA; 0 ÷ 100μA; 0 ÷ 1mA; 0 ÷ 10mA. Due to the pulsating semi-sine form DC voltage used to plasma ignition and to sustain the discharge, the plasma and the probe current has the same pulsation. Therefore a filter has been implemented in the micro-controller to calculate the average value of the current over 10 periods of the plasma discharge (the frequency of the plasma discharge is 100 Hz). Because there are often sparks inside the plasma, the computer and the data acquisition board must be separated using optocouplers. Fig. 5 presents the block diagram of the current measurement unit. There are four range selector switches and shunt resistors included for the four current ranges. The voltage measured on the different resistors, using amplifier and scaling circuits are modified to be suitable input signal for the micro-controller. This signal is measured by the micro-controller which makes the switching when they are needed, and also sends the data to the data acquisition board. Communication is realized by the channels, DATA link, CLK (clock) signal and an INT (interrupt) signal.

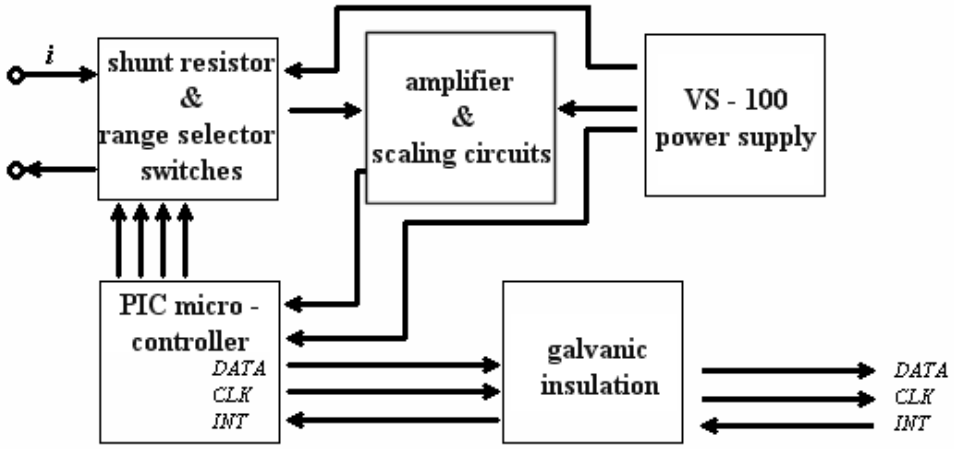

Fig. 5. Block diagram of the current measurement unit

4.4. The PlasDiag data acquisition application.

The power supply and the current meter are PC-controlled using an Advantech PCI-1711 data acquisition board. To perform the measurements an application has been wrote in Visual C++ language. The application called PlasDiag, executes the next functions: measures the voltage-current curve of the probe, saves the

data in a *.pld format; can export the data into an *.m file which can be run under MatLab and shows the curve on a graphics; during measurements the actual values of the voltage current are shown on the screen; presents the voltage and current values in a list; the voltage range and the accuracy of the bias voltage can be set.

4.5. Measurement and results

After assembling the new automated local plasma diagnostics system was tested. We measured probe voltage-current curves in different plasma conditions. The measurements were identical with the ones we measured by setting the probe voltage by the hand, but we obtained improved accuracy and gained speed in the measurements. Fig. 6 shows three curves measured in the same position inside the plasma reactor in different plasma conditions. The pressure inside the reactor was, no working gas was used, the residual gas pressure was 10^{-1} mbar. The cathode bias voltages and currents were: curve I. $U_C = -680\ V$, $I = 15\ mA$; curve II. $U_C = -520\ V$, $I = 10\ mA$; curve III. $U_C = -480\ V$, $I = 5\ mA$.

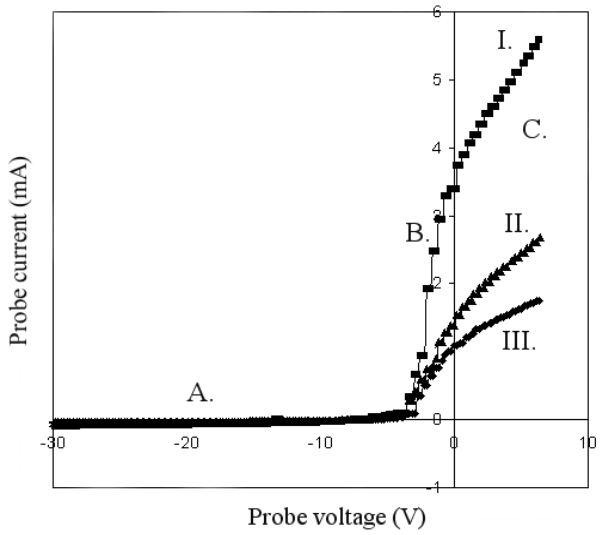

Fig. 6. Probe voltage-current curves: $\Phi 1{,}5 x 3\ mm$

There are three different regions of the probe voltage-current curve: A. ion current region, B. transition region and C. electron current region. Region C. is not suitable for plasma parameter calculations because electrons are moving in an accelerating field. The region between high negative potential and the plasma potential is suitable for this purpose, because electrons feel retarding field in this region. The curves were analyzed using the method presented in Section 3.2. Fig. 7 presented the analysis of Curve II, Fig.6.

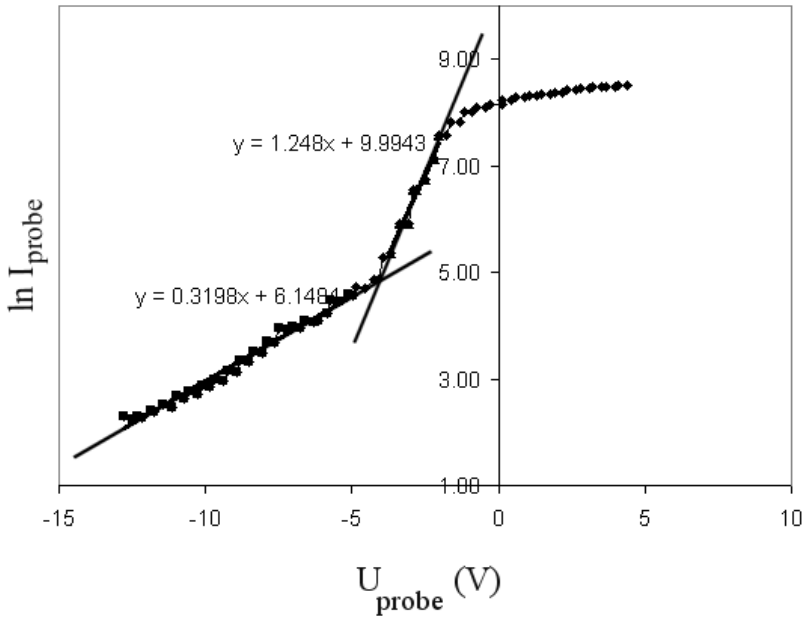

Fig.7. Natural logarithm of the electron current

It can be seen on the figure, that the curve presents two linear regions with different slopes. In this case the slope of the lines can be expressed using the formula below,

$$T_e = \frac{e}{tg(\alpha)\cdot k}$$

where, *e* is the elementary charge of the electron, *k* is the Boltzmann-factor and $tg(\alpha)$ is the slope of the line and T_e is the electron temperature. According to Fig. 7 (and all other voltage-current we studied) there are two electron population in the plasma, one with higher (10^4 K) energy (called primary electrons) and one with a magnitude lower (10^3 K) energy (called secondary electrons). For the three curves presented in Fig. 4, the energies of the electron populations are presented in Table 2.

Table 2.

Curve	T_{e_1} (K) (primary electrons)	T_{e_2} (K) (secondary electrons)
I	$3{,}17 \cdot 10^4$	$6{,}97 \cdot 10^3$
II	$3{,}63 \cdot 10^4$	$9{,}29 \cdot 10^3$
III	$3{,}76 \cdot 10^4$	$6{,}9 \cdot 10^3$

5. Conclusions

We used two methods, different probe configurations to investigate the plasma of an industrial plasma nitriding apparatus. In on of the methods we used manual data collection and a relatively long (large collector surface) probe, while in the other one we used automated data collection and a much smaller probe. Both methods and probe configuration provided the same plasma parameter values. We observed two electron populations and calculated the electron temperatures which correspond to the theory. Using the automated data collection setup we gained speed in data collection and more accurate measurement of the probe voltage-current curve. The next challenge will be the establishment of a measurement configuration where the probe can be moved in radial direction (perpendicular to the symmetry axis of the plasma recipient). Such experimental setup will provide information o radial distribution of the electron temperature and density which could be very useful in adjudging the debate going on the regarding the different theoretical model dealing with the plasma nitriding process.

5. Acknowledgement

The authors wish to thank IPC (Institute for Research Programs of the Sapientia Foundation) for the given support.

REFERENCES

1. J.Kölbel, Forschungsber. Landes Nordrhein-Westfalen, 1965 (1555).
2. B.Edenhofer, HTM 29 (1974) 2 p.105-112.
3. M.Hudis, J.Appl.Phys. vol.44. No.4. April 1973. p.1489-1496.
4. G.G.Tibbets, J.of Appl.Phys. vol.45. No.11. November 1974. p.5072-5073.
5. Farkas, Sz.; Filep, E.; Kolozsváry, Z.: Plasma Nitriding Improves Service Behaviour of Textile Machine Components,. Proc. of 18th Int.Cong on HTM, Detroit, Michigan, 1980, p 296-311.
6. T.Wierzchon, S.Pokrasen, T.Karpinski: HTM 38 (1983) p.57-62.
7. A.Szabo, H.Wilhelmi, HTM. 39 (1984) 148-151.
8. H.Michel, M.Foos, M.Gantois, Proc.1st Int.Conf.on Ion Nitriding.Cleveland, OH. ASM. Metals Park OH, 1987, p 117
9. T.Lampe, S.Eisenberg, G.Laudien, Surf.Eng. 1993. Vol.9. No.1. p.69-76.
10. H.Michel, T.Czerwiec, M.Gantois, D.Ablitzer, A.Ricard, Surf.and Coat.Techn. 72 (1995) p.103-111.
11. T.Czerwiec, H.Michel, E.Bergmann, Surf and Coat Techn, 108-109 (1998) p182-190.
12. T.Belmonte, S.Bockel, H.Michel, D.Ablitzer, Surf and Coat Techn. 112 (1999) p.5-9.
13. T.Belmonte, T.Czerwiec, H.Michel, Surf and Coat Techn.142-144 (2001) p.306-313.
14. J.A.Thornton, J.Vac.Sci.Technol. Vol. 15, No 2, March/April 1978, p.188-192.

15. R.M. Clements, J.Vac.Sci.Technol. Vol. 15, No 2, March/April 1978, p 193-198.
16. E.Eser, R.E. Oglivie, J.Vac.Sci.Technol. Vol. 15, No 2, March/April 1978. p.199-202.
17. D.J. Ball, J.Appl.Phys. Vol.43, No.7,July 1972. p 3047-3056.
18. G.J.H.Brussaard, M. Van der Steen, M.Carrère, M.C.M.van de Sanden, D.C.Schram, Surf and Coat Techn. 98 (1998) p 1416-1419.
19. C.X.Li, T.Bell, H.Dong, Surf.Eng. 2002 Vol 18 No 3 p,174 – 181.

STUDIA UNIVERSITATIS BABEŞ-BOLYAI, PHYSICA, LIII, 1, 2008

PHYSICAL CHARACTERIZATION OF SOME MUCOADHESIVE GELS FOR ORAL CAVITY APPLICATIONS

ELENA DINTE[1*], M. TODICA[2], C. V. POP[2], S. E. LEUCUTA[1]

ABSTRACT. The influence of formulation on rheological characteristics of bioadhesive buccal gels based on polyacrilic acid (Carbopol 940) and carboxymethylcellulose sodium (CMCNa) was investigated. The flow behaviour, the consistency and the spreading capacity of these gels were evaluated. The rheograms obtained corresponded to some tixotropic gels with pseudo plastic or plastic behavior. The increase of the polymer ratio in the gel content led to the increase of the yield stress and the decrease of the maximum penetration degree and of the spreading surface. The results obtained showed that Carbopol 940 had a predominant effect on the rheologic characteristics of these gels.

Keywords: bioadhesive buccal gels hydrophil polymers metronidazole rheology

1. Introduction

Bioadhesion is an important way to improve drug delivery sytems. The potential advantages that bioadhesion can offer include prolonged drug delivery, localization of the therapy, targeting of the specific tissues and an intimate contact with the substrate (1).

Mucoadhesive polymers are essential in the development of buccal delivery systems. The polymeric matrix ensure long time retention of active substance on the buccal mucosal surface and provide an intimate contact between the dosage form and the absorbtion tissue. The retention time of the dosage form depends on the mucoadhesivity of the system (2).

A high mucoadhesivity of these systems and the possibility to controlle the release of the drug from the dosage form are important goal in the development of prolonged drug delivery systems (3).

More formulations of bioadhesive preparations with metronidazole have been reported in the literature. In these formulations the polymeric matrix is represented by various types and mixtures in different ratios of some polymers recognized for their bioadhesive properties and for their controlled release properties (4,5). Metronidazole is a chemotherapeutic agent used in the treatment of the infections with anaerobic agents frequently populating the buccal mucosa (6,7,8,9).

[1] *"Iuliu Hatieganu" University of Medicine and Pharmacy, Faculty of Pharmacy, Department of Pharmaceutical Technology and Biopharmaceutics*
[2] *"Babes-Bolyai" University, Faculty of Physics, Cluj-Napoca, Romania*
* *edinte@umfcluj.ro*

The rheologic investigation of the semisolid preparations provide useful information required for the preparation and for the assessment of some of the final properties of the product, e.g. consistency, spreadability on the skin, stability, storage, etc. (10-12).

The aim of the study was the formulation and physical characterization of a bioadhesive gel with metronidazole intended to be used for the topical treatment of certain diseases of the buccal mucosa.

2. Materials and methods

The materials used were polyacrillic acid (Carbopol 940, B.F. Goodrich), sodium carboxymethylcellulose (NaCMC forte, Loba Chemie-Wien-Fischamend), glycerol, triethanolamine (Merk), metronidazole (USP).

Methods

Preparation of bioadhesive gels

We prepared two kind of samples: simple and mixed gels. The simple gels (formulations 1-3) were obtained by dispersion of the Carbopol 940, in different concentrations (according to the Table 1), in distilled water (heated at 70^{o}C); as umectant we used the glycerol in the same ratio. The dispersions were neutralized with triethanolamine. The formulation 4 was obtained using only NaCMC dispersed in water and glycerol.

The mixed gels were obtained by mixing simple gels, based on Carbopol 940 and NaCMC, respectively, separately prepared, using a homogeniser. In the mixed gels, Carbopol 940 was combined with NaCMC in a 1:1, 3:1 and 1:3 ratio, the total concentration of the polymers in the gels being 2%. Metronidazole was incorporated by suspending it in a ratio of 1% in the gel. Table I shows the composition of the studied formulations.

Table I.

Composition of bioadhesive buccal gels

Formulation	Carbopol 940 (%)	CMCNa (%)	Glycerol (%)	Tryethanol-amină (%)	Metronidazole (%)	Distilled water
1	0.5	-	10	0.5	1	ad 100 g
2	1	-	10	0.9	1	ad 100 g
3	1.5	-	10	1.3	1	ad 100 g
4	-	3	10	-	1	ad 100 g
5	1	1	10	0.85	1	ad 100 g
6	1.5	0.5	10	1.25	1	ad 100 g
7	0.5	1.5	10	0.45	1	ad 100 g

Determination of gel viscosity

The viscosity was measured with Rheotest viscosimeter type RV (Medingen). The determinations were made at 37ºC. The rheograms of the studied formulations were obtained by measuring the shear stress for different shear rate; the areas of the histeresis loop between the up and down curves were calculated. For the gels with plastic behavior the values of the yield stress were calculated.

Study of gel consistency

Penetrometric determinations were carried out using a cone penetrometer (aluminium cone with a height of 4 cm, base diameter of 3 cm and a weight of 30g). The determinations were made at 20ºC (±0.5ºC) and the maximum penetration degree was evaluated after a fixed time (5 min). The statistic interpretation of the data was made using Student t test (11).

Study of spreading capacity

The determinations were made with a Pozo Ojeda and Sûne Arbussa extensometer (11). It was used a 1g sample, and the weight applied was increased by a 100g at 1 minute intervals. The spreading surfaces (mm^2) were calculated and the extensometric curves were drawn; these represent the surface (S) occupied by the gel depending on the weight (W) applied.

3. Results and discussion

a. Evaluation of the viscosity

The rheological behaviour was plotted in shear stress diagrams as function of shear rate (Fig. 1-4). It was observed that the shear stress presented a nonlinear dependance on shear rate. This behaviour is characteristic for non-Newtonian fluids. For a given shear rate we observed an increasing of the shear stress with the increasing of Carbopol 940 concentration. For the analyze of rheological data, a Herschel-Bulkley model was used:

$$\tau = \tau_0 + K \cdot \gamma^n$$

where, τ = shear stress (Pa), γ = shear rate (s^{-1}), K and n are consistency and plasticity descriptors, respectively. The term τ_o is the yield stress and represents the shear stress necessary the flow to begin. For $n<1$, the samples are supposed to have a pseudoplastic behaviour and for $n>1$ the plastic, respectively (11).

In our case, the 0.5% Carbopol 940 gel (formulation 1), the 3% NaCMC gel (formulation 4) and the mixed gel containing 0.5% Carbopol 940 mixed with 1.5% NaCMC (formulation 7) presented a pseudoplastic behaviour.

The formulations 2,3,5 and 6 of gels (see table I) presented a plastic behaviour with yield stress.

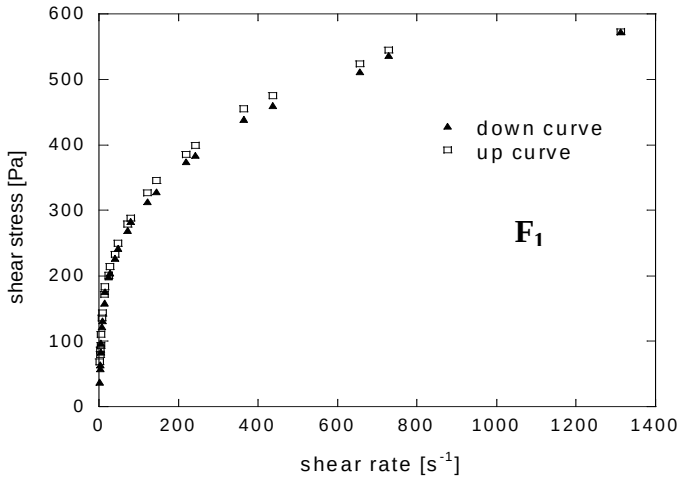

Fig. 1. Flow curve of gel containing 0,5% Carbopol 940 (F_1 according to Table 1)

Figures 1-4 show the flow curves of the formulations with psudoplastic behaviour: F1- Carbopol 940 0.5%, F7 – 0.5% Carbopol 940 - 1.5% NaCMC and plastic behaviour: F3-Carbopol 940 1.5% and F6 - 1.5% Carbopol 940 - 0.5% NaCMC.

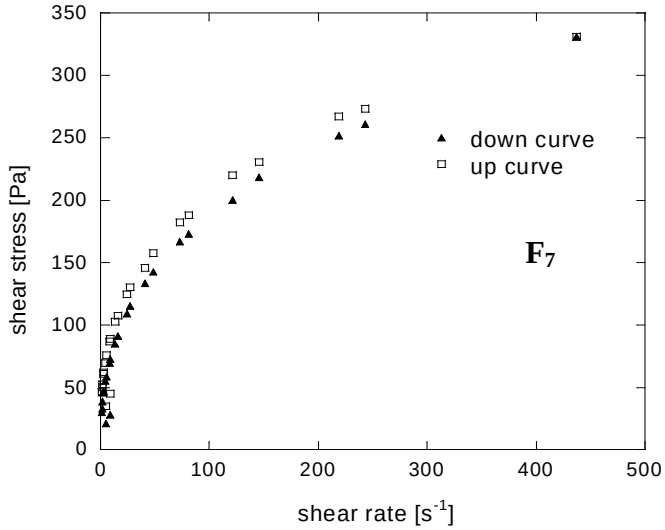

Fig. 2. Flow curve of gel containing 0,5% Carbopol 940 and 1,5% NaCMC (F_7 according Table 1)

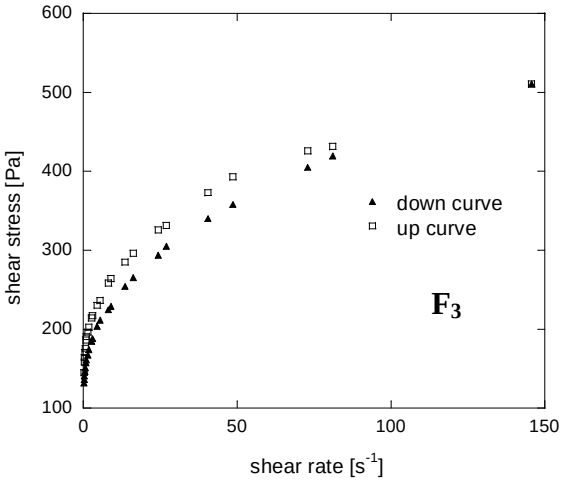

Fig. 3. Flow curve of gel containing 1,5% Carbopol 940 (F_3 according to Table 1)

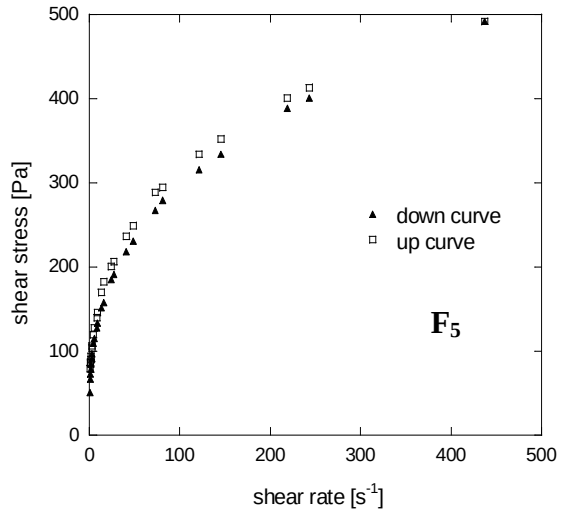

Fig. 4. Flow curve of gel containing 1% Carbopol 940 and 1% NaCMC (F_5 according to Table 1)

Fig. 5 shows the variation of the yield stress of the studied gels presenting plastic behaviour.

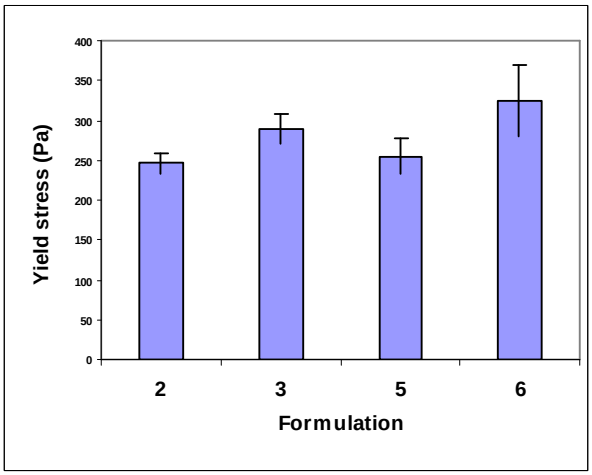

Fig. 5. Influence of the formulation (see table I) on the yield stress of the plastic gels containing Carbopol 940 and NaCMC.

It was found that the yield stress used as an indicator of the plastic character of the gels increases with the rise of the polymer ratio in the simple gels (formulation 2 and 3). Comparison of the simple gels with the mixed ones containing the same concentration of Carbopol 940 to wich NaCMC is added to a total concentration of 2% revealed that the yield stress increased in the mixed gels with higher polymer concentrations: gel 5 (255±22 Pa) as against gel 2 (247±13.3 Pa), and gel 6 (325±42.3 Pa) as against gel 3 (289±19.89 Pa). In the mixed gels containing the same total polymer concentration the yield stress increased with the rise of Carbopol 940 ratio (from 255±22 Pa in gel 5, to 325±42.3 Pa in gel 6).

The presence of the histeresis loop correspond to the transformation of gel in fluids, with an additional loose in viscosity. The tixotropy index (T_{his}) was also calculated with the formula:

$$T_{his} = \left[\frac{(S_{\ up\ curve} - S_{\ down\ curve})}{S_{\ up\ curve}} \right] \cdot 100$$

Where, $S_{\ up\ curve}$ is area of surface under up curve and $S_{\ down\ curve}$ is area of surface under down curve (11).

For the T_{his} greater than 5, the system can be considered tixotropic. All the studied gels presented tixotropic behaviour. This characteristic is very important during the preparation of the gel and for its application on the mucosa (11).

Table II shows the values of the histeresis loop area, tixotropic index and of the highest penetration degree of the studied buccal bioadhesive gels.

Table II.

Values of some rheological characteristics of the studied bioadhesive buccal gels based on Carbopol 940 and NaCMC (according to the Table I).

Formulation (according to Table I)	Area of the histeresis surface (Pa/s) media±S.D.	Tixotropic index media±S.D.	Penetration degree (mm) media±S.D.
1	11845±350	9.17±0.5	42±1.32
2	2680±121	5.5±0.12	39.5±2.78
3	2420±118	14.9±2.23	34±0.86
4	7510±235	15±1.25	42.3±2.04
5	5141±244	9.2±0.75	38.5±1.13
6	3032±85	5.9±0.33	31.5±3.27
7	4820±88	11.7±1.65	39±0.91

In simple Carbopol 940 gels (formulation 1-3) the area of the histeresis loop decreased with the rise of Carbopol 940 concentration varying in the order: F1>F2>F3.

In the mixed gels tixotropy is higher in the gel containing Carbopol 940 and NaCMC in equal ratios (formulation 5), followed by the gel containing a higher NaCMC ratio (formulation 7) and then by gel 6 containing highest ratio of Carbopol 940.

b. Evaluation of the consistency of the buccal bioadhesive gels

Analysis of the results obtained revealed a decrease of the penetration degree due to the greater consistency of the gels simultaneously with the rise of the ratio of the polyacrylic acid in the simple gels. This behaviour can be explained by the increasing of the entanglement degree of the polymeric matrix. Thus, the penetration degree decreases in the order F1>F2>F3 ($P_{F1/F3}<0.05$; $P_{F2/F3}<0.05$).

The gel with 3% NaCMC showed the lowest consistency.

The consistency of the mixed gels based on Carbopol 940 and NaCMC increases in the same manner simultaneously with the rise of the ratio of the polyacrylic acid, although the total polimer concentration in the gel is the same, 2%. Thus, the value of the maximum penetration degree decreases in the order F7>F5>F6($P_{F5/F6}<0.05$).

The consistency of the gels also rises with the increase of the total polymer ratio. Comparing the simple gels with the mixed ones in wich similar Carbopol 940 concentrations were associated with NaCMC to the total concentration of 2% a lowering of the penetration, therefore, an increase of the consistency was noted.

The penetrometric studies provide information on the consistency of the gels. The lower the penetration degree in the gel, the higher is its the consistency, wich depending on the nature of the gel forming polymer can determine an increase of the adhesive capacity and the lowering of the rate of the drug release. Some studies have shown that NaCMC and Carbopol 940 association determined the decrease of in vitro adhesion and the increase of the release rate of the drug. This is due to the faster dispersion of NaCMC in water wich induces an easier desintegration of the gel (13,14).

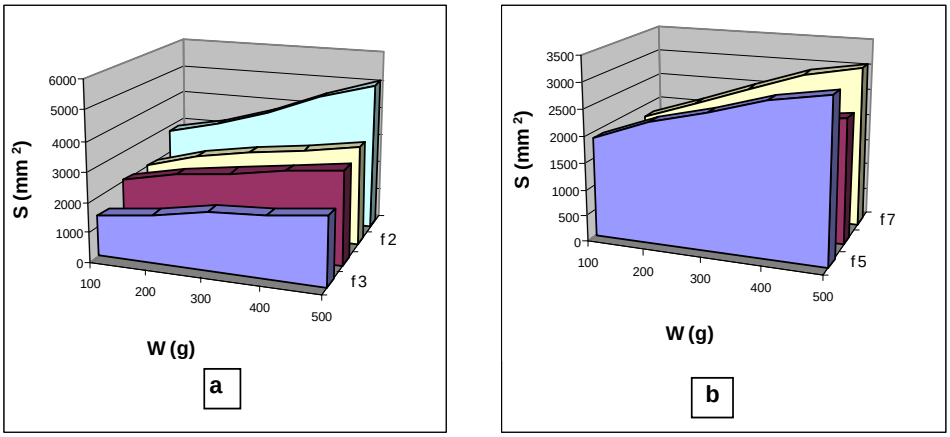

Fig. 6. Spreading capacity of the simple (a) and mixed gels (b), based on Carbopol 940 and NaCMC (formulations 1-7, see table I).

c. Evaluation of the gel spreading capacity

Fig. 6a. shows the extensometric curves of the simple gels based on Carbopol 940 and NaCMC and Fig. 6.b. those of the mixed gels based on Carbopol 940-NaCMC. Analysis of the extensometric curves revealed a decrease of the spreading capacity with the rise of Carbopol 940 concentration in the simple gels (fig.6 a, F1>F2>F3).

The 3% NaCMC gel (formulation 4) showed an intermediate spreading capacity between the 1% Carbopol 940 gel (formulation 2) and the 1.5% Carbopol 940 (formulation 3).

In the mixed gels the spreading surface at the application of a weight of 500g varies within a narrow range from 3066 mm^2 in the gel containing 0.5% Carbopol 940 associated with NaCMC in a ratio of 1.5% (formulation 7) to 2375 mm^2 in the gel containing 1.5% Carbopol 940 associated with 0.5% NaCMC 0.5% (formulation 6); the gel containing the two polymers associated in equal ratios (formulation 5) presented an intermediate value (3045 mm^2).

The extensometric determinations showed greater spreading capacity in gels with a lower consistency. In was found that the rise of Carbopol 940 ratio in the studied gels determined a decrease of the spreading capacity due to a greater consistency.

4. Conclusions

The buccal bioadhesive gels based on Carbopol 940 and NaCMC presented a pseudoplastic or plastic flow with tixotropic behaviour. Carbopol 940 forms plastic gels at concentrations equal or higher than 1%. NaCMC does not form plastic gels at concentration of 3%.

In the simple gels based on Carbopol 940 the rise of Carbopol 940 concentration determined the increase of the yield stress, the decrease of the histeresis surface and of the penetration degree as well as the reduction of the spreading capacity due to an increased consistency of the gels.

The 3% NaCMC gel showed the lowest consistency and an intermediate spreading capacity between 1% and 1.5% Carbopol gels.

Comparison of the simple gels with the mixed ones containing higher polymer concentrations revealed that the studied rheologic parameters also vary with the rise of the total polymer concentrations. Thus, the increase of the polymer ratio determined the rise of the yield stress, the decrease of the penetration degree and the reduction of the spreading capacity.

Carbopol 940 played a predominent role in the determination of the consistency of the studied gels both in the simple and mixed formulations.

The results of the present investigation suggest the possibility of using some of these gels as bioadhesive drug systems with ensuring a prolonged release folowing their application on the buccal mucosa.

REFERENCES

1. Needleman Ian G., Smales C. Frederick, In vitro assessment of bioadhesion for periodontal and buccal drug delivery, Biomaterials 16 (1995) 617-624
2. Munasur A.P., Pillay V., Chetty D.J., Govender T., Statistical optimisation of the mucoadhesivity and characterization of multipolymeric propranolol matrices for buccal therapy, Int. J. Pharm. 323 (2006) 43-51
3. Bromerg L.E., Buxton D.K., Friedman P.M., Novel periodontal drug delivery system for treatment of periodontitis, J. Control. Rel. 71 (2001) 251-289
4. Ponchel G., Touchard F., Wouessidjewe D., Duchêne D., Peppas N., Bioadhesive analysis of controlled-release systems. III. Bioadhesive and release behavior of metronidazole-containing poly(acrylic acid)-hydroxypropyl methylcellulose systems, Int. J. Pharm., 1987, 38, 65-70.
5. Smid-Korbar J., Kristl J., Cop L., Groselj D., Formulation and evaluation of oral mucoadhesive films containing metronidazole, Acta Pharm. Jugosl., 1991, 41, 251-258.
6. Hoffman A., Hydrogels for biomedical applications, Adv. Drug Deliv. Rev. 43 (2002) 3-12.
7. Nagai T., Machida Y., Buccal delivery systems using hydrogels, Adv. Drug Del. Rev. 11 (1993) 179-191.
8. Yajaman Sudhakar, Ketousetuo Kuotsu, A.K. Bandyopadhyay, Buccal bioadhesive drug delivery – A promising option for orraly less efficient drugs, J. Control. Rel., 114 (2006) 15-40.

9. Nechifor M., Terapia antibacteriană, antifungică şi antivirală în stomatologie, Editura Glissando, Iaşi, 2002.
10. Ramachandran S., Chen S., Etzler F., Rheological characterization of hyroxypropyl-cellulose gels, Drug Dev. Ind. Pharm. 25 (2) (1999) 153-161.
11. Popovici A., Tökes B., Papp I., Suciu G., Reologia formelor farmaceutice, Editura Medicală, Bucureşti, 1985.
12. Fizica polimerilor, M. Todica, Editura Univ. Babes-Bolyai, Fac. de Fizica, Cluj-Napoca, 1996.
13. Elena Dinte, S.E. Leucuta, Studiul cedării in vitro a metronidazolului din hidrogeluri bioadezive pe bază de Carbopol 940 şi carboximetilceluloză sodică, Farmacia, Vol. LII (5) (2004) 13-19
14. Elena Dinte, S.E. Leucuta, Studiul proprietăţilor de adeziune in vitro ale unor geluri pe bază de Carbopol 940 şi carboximetilceluloză sodică, Revista de Medicină şi Farmacie-Orvosi es Gyogyszereszeti Szemle, 50, Supl.II (2004) 80-82

STUDIA UNIVERSITATIS BABEŞ-BOLYAI, PHYSICA, LIII, 1, 2008

METAL-CHELATING COMPOUND INVESTIGATED BY RAMAN SPECTROSCOPY

L. SZABÓ, I. B. COZAR, N. LEOPOLD, A. PIRNĂU, V. CHIŞ*

ABSTRACT. Raman and SERS spectra of 4-(2-pyridylazo) resorcinol (PAR) molecule and its metal (Zn(II), Cu(II), Mn(II)) complexes were recorded using a hydroxylamine reduced silver colloid. Complete assignments of experimental spectra were made by using the B3LYP/6-31G(d) theoretical results. The calculated molecular electrostatic potential (MEP) for PAR molecule shows that the most negative regions are associated with the two oxygen and three nitrogen atoms. Differentiation between PAR complexes with Cu(II), Zn(II), Mn(II) is shown by the SERS spectral features of each complex.

Keywords. Raman spectroscopy, SERS spectra, Molecular potential

1. Introduction

An interesting class of molecules with cationic recognition properties, like deferoxamine (DFO), ethylenediaminetetraacetic acid (EDTA), dimercaptosuccinic acid (DMSA), 2,3-dimercapto-1-propanesulfonic acid (DMPS) or alpha lipoic acid (ALA) are used in conventional and alternative medicine for detoxing the human body of toxic metals, within the so-called *chelation therapy* [1-6]. The chelating agents contain usually donor atoms like nitrogen, oxygen or sulfur which have available electrons to form coordination compounds with a metal ion. While mobilization of the toxic metal out of the body is an important part of *chelation therapy*, the ultimate goal is a decrease in toxicity. The chelate (chelating agent – metal ion complex), has often different properties with respect the chelating agent itself, or the metal ion alone, being usually without toxicity. Chelation therapy consists in the administration of chelating agents to remove heavy metals from the body. The chelating agents bond the metallic ions present in excess in the human body, being afterwards eliminated. Thus, deferoxamine (DFO) shows highest affinity for Fe(III) ions, but it is used also in detoxing processes with Al(III) [3, 7, 8]. EDTA forms stable compounds with bivalent and trivalent ions like Cu(II), Cd(II), Pb(II), Mn(II), Fe(III) and Co(II) [9-12].

In this work, experimental and theoretical investigations on 4-(2-pyridylazo) resorcinol (PAR) are presented. This compound is a widely used metal indicator and recently, a sensor approach for Cu(II) detection in urine [13]. The determination of copper in urine is of particular interest in clinical chemistry for purposes of diagnosis, for monitoring Wilson's patients under chelation therapy, for detection of environmental or occupational exposure, and for nutritional studies. Also, an optical sensor for analysis of Zn(II) in pharmaceuticals was developed using PAR as chelating agent [14].

* *Babeş-Bolyai University, Faculty of Physics, Kogălniceanu 1, 400084 Cluj-Napoca, Romania*

2. Experimental

4-(2-pyridylazo) resorcinol monosodium salt monohydrate (PAR) of the highest commercially available purity were obtained from Merck Romania. Zn(II), Mn(II) and Cu(II) complexes were prepared by adding 0.6 M $ZnCl_2$, $MnCl_2$ and $CuSO_4$ solution aliquots to 0.02 M PAR solutions, obtaining the 1:1 ligand:metal ion stoichiometric ratios.

The FT-Raman spectrum of PAR in solid state was recorded in backscattering geometry with a FRA 106/S (Bruker) Raman accessory equipped with nitrogen cooled Ge detector. The 1064nm Nd:YAG laser was used as excitation source, and the laser power was set at 300mW. The FT-Raman spectrum was recorded with a resolution of ~4cm^{-1} by co-adding 32 scans.

For SERS measurements, 5 µl of analyte were added to 0.5 ml silver colloid. The silver colloidal SERS substrate was prepared reducing silver with hydroxylamine [15]. Briefly, 0.017 g silver nitrate were solved in 90 ml distilled water. In a separate recipient, 0.017 g of hydroxylamine hydrochloride were solved in 10 ml water, followed by the addition of 0.17 ml sodium hydroxide solution 2 mol/l. The hydroxylamine/sodium hydroxide solution was then added rapidly to the silver nitrate solution under vigorous stirring. After a few seconds a grey brown colloidal solution resulted, with pH value 8.5, and was further stirred for 10 minutes. SERS spectra were recorded with a Raman Micro spectrometer LabRam HR800 (Jobin Yvon) equipped with a coupled charge detector (CCD) and a HeNe laser emitting at 632.8 nm with power set to 14.5 mW. All SERS spectra were recorded with a spectral resolution of about 4 cm^{-1}.

3. Computational detail

The molecular geometry optimizations, vibrational spectra and molecular electrostatic potential calculations were performed with the Gaussian 98W software package [16] by using Density Functional Theory (DFT) methods with B3LYP hybrid exchange-correlation functional [17] and the standard 6-31G(d) basis set. The geometries were fully optimized without any constraint with the help of analytical gradient procedure implemented within Gaussian 98W program.

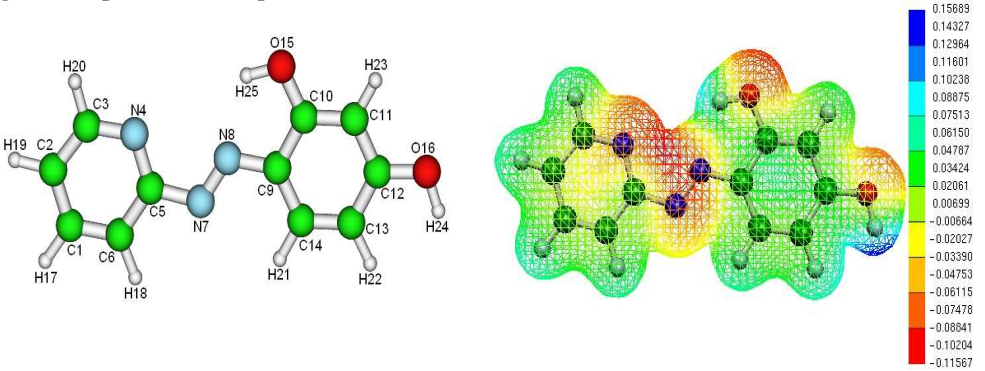

Figure 1. Optimized geometry and the calculated 3D molecular electrostatic potential for PAR.

The vibrational frequencies were computed at the optimized geometry to ensure that no imaginary frequencies were obtained, confirming that it corresponds to a local minimum on the potential energy surface. Vibrational mode assignments were made by visual inspection of modes animated by using the Molekel program [18].

4. Results and discussion

The optimized geometry and the 3D molecular electrostatic potential (MEP) contour map for PAR molecule is shown in Figure 1. The MEP is widely used as such a reactivity map displaying most probable regions for the electrophilic attack and in studies of biological recognition and hydrogen bonding interactions [19]. As can be seen in the MEP distribution, negative V(r) values are associated with N4, N7, N8, O15 and O16 atoms. Also, it must be considered that, when added to the silver colloidal solution, the chlorine anions chemisorbed onto the colloidal surface induce positively Ag charged particles, and thus, the adsorption of the molecules to the silver surface is supposed to occure through atoms with high negative charges. In addition, the adsorption through the ring π-electrons is not sustained by the MEP distribution.

After the optimization of the molecular geometry, the normal vibrational modes of the PAR molecule was calculated and some selected bands are collected in Table 1. The calculated wave numbers were scaled with the 0.9614 factor, corresponding to the B3LYP / 6-31G(d) method.

Table 1.

The assignment of Raman bands for PAR

Mode	Experimental wavenumbers (cm^{-1})	Calculated wavenumbers (cm^{-1})	Assignments
1	222	217	γ(rg2)+γ(NN)
2	532	530	i.p. rg2 def.
3	636	633	i.p. rg1 def.
4	862	855	τ(CH)
5	995	1007	δ(CCC rg1)+δ(CNC rg1)
6	1053	1030	δ(CCC rg1)
7	1126	1132	δ(CH rg1)
8	1190	1186	δ(OH)+δ(CH)+ν(CN)
9	1265	1249	ν(CC)+ν(CN)+δ(CH)
10	1390	1417	δ(CH)+ν(CC)
11	1446	1435	ν(NN)+ν(CC)+δ(CH)
12	1479	1486	υ(NN)+δ(CH)
13	1560	1567	ν(CC)+ν(CN)+δ(CH)
14	1597	1579	υ(CC)+δ(CH)
15	1618	1618	υ(CC)+δ(CH)

ν-stretching, δ-in plane bending, τ-twisting, γ-out of plane bending, rg1- C1-C2-C3-N4-C5-C6, rg2-C9-C10-C11-C12-C13-C14

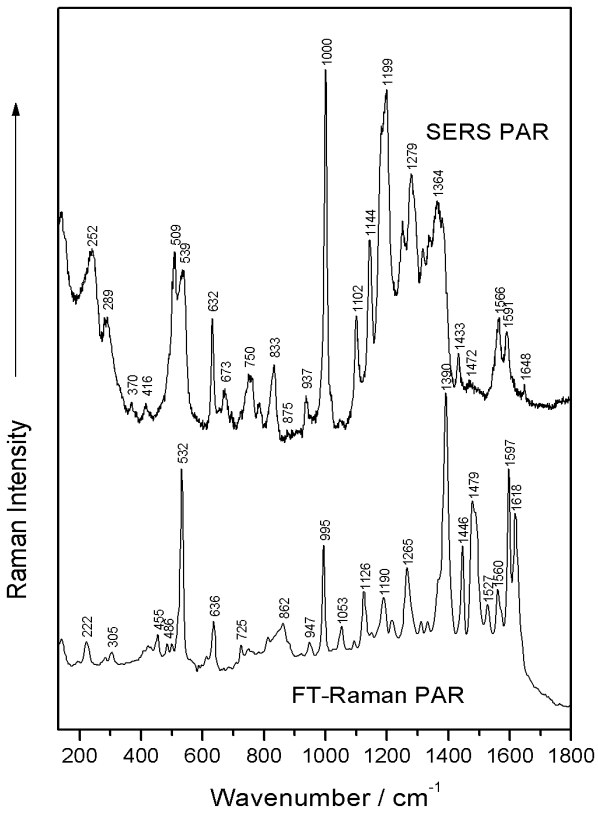

Figure 2. FT-Raman and SERS spectra of PAR.

As mentioned previously, the DFT calculated molecular electrostatic potential predicts the highest electronic density around the nitrogen and oxygen nuclei. Therefore, the adsorption of the PAR molecule to the Ag colloidal particles surface is possible by these atoms.

Comparing the Raman and SERS spectra (Fig.2), it can be noticed that the position and the relative intensity modification of several bands, indicate the existence of an interaction between the PAR molecule and the Ag particles. The most intense SERS bands are those around the values 509, 632, 1000, 1199 and 1364 cm^{-1}, while in the Raman spectrum the most intense bands appear around the values of 532, 995, 1390, 1479, 1597 and 1618 cm^{-1}. Taking into account the optimized geometry of the PAR molecule, we consider that the adsorption through the N7 and N8 atoms is less probable due to sterical (geometrical) reasons. The adsorption through the N7 and N8 atoms is also improbable, because in the case of the existence of this bonding type, the vibration of the NN bond should appear amplified in the SERS spectrum, but in reality this band (1479 cm^{-1}) is very weak. Therefore, the most probable way of PAR adsorption to the Ag surface is through the N4 atom, the spectral modifications which appear in the SERS spectrum, compared to the Raman spectrum, confirming this way of adsorption.

The enhancement of the PAR SERS bands at 539 cm^{-1} and 632 cm^{-1} assigned to in plane deformation vibrations of the two rings, sustain the hypothesis of adsorption of PAR through the N4 atom. Also, the bands at 1199 cm^{-1} and 1364 cm^{-1}, which are enhanced in the SERS spectrum of PAR, assigned to in plane deformation modes of the molecule (Table 1.), confirm this supposition.

Taking in account the SERS selection rules and the amplification of the vibrations due to several stretching or deforming vibrations in the molecule plane, it can be concluded that the adsorbed PAR molecule is orientated rather perpendicular on the metallic surface.

In general, the bands attributed to the total symmetrical vibrations of the aromatic rings appear in the Raman spectra as bands of medium or high intensity being, normally, very narrow. For PAR molecule, the total symmetric vibrations of the two aromatic rings can be seen in Raman spectrum at 532 and 995 cm^{-1}, respectively.

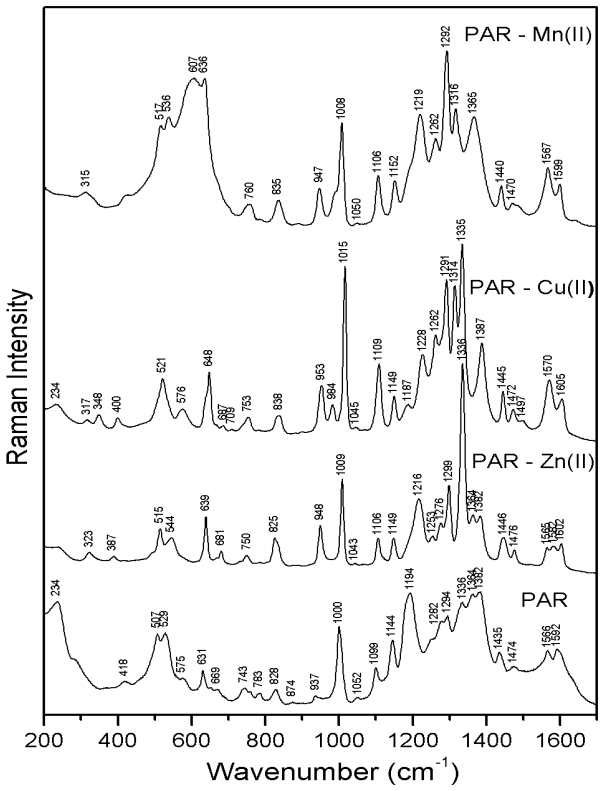

Figure 3 SERS spectra of PAR- Zn(II), Cu(II) and Mn(II) complexes, prepared at PAR: metal salt 1:1 molar ratio.

The corresponding bands appear amplified in the SERS spectrum at 539 and 1000 cm^{-1}, respectively. Therefore a tilted orientation on the metallic Ag surface is expected for PAR molecule.

The chelation mode of PAR with some metal ions was reported by Greay *et al.* [20]. At pH values above 5.0, PAR forms 2:1 complexes with Zn(II) and Cu(II) [13], the atoms involved in the coordination being the pyridine nitrogen (N4), the azo nitrogen farthest from the heterocyclic ring (N8), and the O-hydroxyl group (O15) [21-23].

As seen in Fig.3 where the SERS spectra of PAR-Zn(II), Cu(II) and Mn(II) complexes are given, PAR-metal complexes can be differentiated by their SERS spectral features. Thus, shifts of band positions and changes in relative intensities in the SERS spectra suggest structural modifications due to the complexation of the Zn(II), Mn(II) and Cu(II) ions with PAR ligand. Each PAR-metal complex SERS spectrum in Fig. 3 shows a characteristic spectral fingerprint. Thus, several SERS bands are representative for each PAR-metal complex: 648, 1015, 1291, 1314 and 1387 cm^{-1} for PAR-Cu(II) and 515, 639, 1009, 1216 and 1336 cm^{-1} for PAR-Zn(II) and 636, 1008, 1219, 1292, 1365 cm^{-1} for the Mn(II) complex of PAR.

5. Conclusions

Optimized geometries, molecular electrostatic potential and normal modes of PAR molecule were calculated by theoretical DFT methods. The assignment of the experimental vibrational bands of this molecule was done on the basis of B3LYP/6-31G(d) theoretical results.

Comparing the Raman and SERS spectra, the atoms involved in the adsorption to the Ag surface were derived. The PAR molecule is adsorbed in a predominant perpendicular orientation on the Ag surface through the N4 atom.

PAR- Zn(II), Cu(II) and Mn(II) complexes can be differentiated by their SERS spectral features, each PAR-metal complex SERS spectrum showing a characteristic spectral fingerprint.

Acknowledgment

Financial support from the Romanian National Authority for Scientific Research is highly acknowledged (grant ID 501).

REFERENCES

1. D.F. Thompson, E.D.Callen, Ann. Pharmacother., **38**, 1509 (2004).
2. M. Blanuşa, V.M. Varnai, M.Piasek, K.Kostial, Current Medicinal Chemistry, **12**, 2771 (2005).
3. O.Cozar, N.Leopold, C.Jelic, V.Chiş, L.David, A.Mocanu, M.Tomoia-Cotisel, J.Molec. Structure, **1**, 788 (2006).
4. J.F.Risher, S.N.Amler, Neurotoxicology, **26(4)**, 691 (2005).
5. J.S.Shrihari, A.Roy, D.Prabhakaran, K.S.Reddy, Natl. Med. J. India, **19(1)**, 24 (2006).
6. D.M. Seely. P.Wu, E.J.Mills, BMC Cardiovascular Disorders, **5(32)**, (2005).
7. S.Dhunganga, P.S. White, A.L. Crumbliss, J.Biol. Inorg. Chem., **6**, 810 (2001).
8. B.Borgias, A. D. Hugi, K.N. Raymond, Inorg Chem., **28**, 3538 (1989).
9. J.S.Shrihari, A.Roy, D.Prabhakaran, K.S.Reddy, Natl. Med. J. India, **19(1)**, 24 (2006).
10. C.D.Klaasen, The Pharmacological Basis of Therapeutics. 11th Ed.; McGraw – Hill: New York, 2006.
11. C.L.Seaton, J.Lasman, D.R. Smith, Toxicol. Appl. Pharmacol, **153**, 159 (1999).
12. D.F.Thompon, E.D.Callen, Ann. Pharmacother., **38**, 1509 (2004).
13. P.C.A. Jeronimo, A.N. Araujo, M.C.B.S.M. Montenegro, C. Pasquini, I.M. Raimundo Jr, Anal. Bioanal. Chem., **108**, 380 (2004).
14. P.C.A. Jeronimo, A.N. Araujo, M. Conceicao, B.S.M. Montenegro, Sens. Actuators B **103**, 169 (2004).
15. N. Leopold, B. Lendl, J. Phys. Chem. B, **107**, 5723 (2003)

16. M.J. Frisch, G.W. Trucks, H.B. Schlegel, G.E. Scuseria, M.A. Robb, J.R. Cheeseman, V.G. Zakrewski, J.A. Montgomery Jr., R.E. Stratmann, J.C. Burant, S. Dapprich, J.M. Millam, A.D. Daniels, K.N. Kudin, M.C. Strain, O.Farkas, J. Tomasi, V. Barone, M. Cossi, R. Cammi, B. Mennucci, C. Pomelli, C. Adamo, S. Clifford, J. Ochterski, G.A. Petersson, P.Y. Ayala, Q. Cui, K. Morokuma, D.K. Malik, A.D. Rabuck, K.Raghavachari, J.B. Foresman, J. Cioslowski, J.V. Ortiz, A.G. Baboul, B.B. Stefanov, G. Liu, A. Liashenko, P.Piskorz, I. Komaromi, R. Gomperts, R.L. Martin, D.J. Fox, T. Keith, M.A. Al-Laham, C.Y. Peng, A. Nanayakkara, C. Gonzalez, M. Challacombe, P.M.W. Gill, B. Johnson, W. Chen, M.W. Wong, J.L. Andres, C. Gonzalez, M. Head-Gordon, E.S. Replogle, J.A. Pople, Gaussian 98, Revision A.7, Gaussian, Inc., Pittsburg, PA, 1998
17. R.G. Parr, W. Yang, Density-Functional Theory of Atoms and Molecules, Oxford University Press, New York, 1989
18. P. Flukiger, H.P. Luhti, S. Portmann, J. Weber, MOLEKEL 4.2, Swiss Center for Scientific Computing, Manno (Switzerland), 2000–2002; S. Portmann, H.P. Luhti, Chimia, **54**, 766 (2000).
19. P. Politzer, D.G. Truhlar, (Eds.), Chemical Application of Atomic and Molecular Electrostatic Potentials, Plenum, New York, 1981.
20. W.J. Greay, G. Nickless, F.H. Pollard, Anal. Chim. Acta, **27**, 71 (1962)
21. J. Ghasemi, H. Peyman, M. Meloun, J. Chem. Eng. Data, **52**, 1171 (2007)
22. Z.T. Jiang, J.C. Yu, H.Y. Liu, Anal. Sci., **21**, 851 (2005)
23. F. Karipcin, E. Kabalcilar, Acta Chim. Slov., **54**, 242 (2007).

STUDIA UNIVERSITATIS BABEŞ-BOLYAI, PHYSICA, LIII, 1, 2008

PRODUCTION OF THE MEDICAL RADIOISOTOPE ^{64}CU AT A CYCLOTRON BY DEUTERON INDUCED REACTIONS ON ENRICHED ^{64}NI TARGETS

LAURA DARABAN, O. COZAR, L. DARABAN*

ABSTRACT. The production of ^{64}Cu, a radioisotope of considerable interest for the application in nuclear medicine for PET imaging and radioimmunotheraphy, was investigated by deuteron bombardment of enriched ^{64}Ni target up to E_d = 20.5 MeV. The experimental excitation function for the reaction ^{64}Ni(d,2n)^{64}Cu was measured using the stacked foil irradiation technique followed by HPGe γ-ray analysis at 1345 keV and is compared with earlier literature values.

Keywords: excitation function, deuteron reaction, medical radionuclide, ^{64}Cu production, γ-ray spectrometry**.**

Introduction

Over the several past years, there has been a growing interest in the use of radiopharmaceuticals labeled with metallic radionuclides, especially the isotopes of copper. Among them ^{64}Cu ($T_{1/2}$ = 12.7 h) has a branched decay (β^-: 38.5 %, β^+: 18 %; EC: 61.5 %) that ensures the potential to serve a dual role in the development of molecular agents in positron emission tomography (PET) and radioimmunotheraphy drugs in oncology [1- 3]. The behavior of some ^{64}Cu labeled compounds such as ^{64}Cu -PTSM and ^{64}Cu -ATSM have been successfully investigated in cell cultures, rats and humans [4].

Several ^{64}Cu production methods have been studied by numerous groups [5- 10]. A high specific activity for ^{64}Cu, suitable for radiolabeling of insoluble complexes and monoclonal antibodies, can be achieved via de ^{64}Ni(p,n)^{64}Cu reaction.

From previous comparisons of yields of (p,n) and (d,2n) reactions [11], leading to the same residual radioisotope for targets in the medium mass region, it was observed that in most of the cases the deuteron induced channel is to be preferred. Cross section data for the (d,2n) process were hence requested by an IAEA coordinated research project on the production of therapeutic radioisotopes in 2004. In order to obtain cross section data for the production of ^{64}Cu with reduced uncertainties and based on better counting statistics, we performed a new series of experiments using enriched ^{64}Ni as target material.

* *Department of Biomedical Physics, University Babes-Bolyai, RO-400084 Cluj-Napoca, Romania*

Material and methods

Nickel is an important structural and surface coating material, frequently used in accelerator and nuclear technology. The cross-sections for the reaction ^{64}Ni(d,2n)^{64}Cu were studied using the stack foil technique. Two stacks each containing 8 foils of enriched ^{64}Ni (96.1 % abundance, impurities: ^{58}Ni 1.95 %, ^{60}Ni 1.31 %, ^{61}Ni 0.13 %, ^{62}Ni 0.51 %, obtained from Isoflex USA) were irradiated with deuterons up to 20.5 MeV in the external beam of the VUB-Cyclotron CGR-560 in Brussels, Belgium for around one hour.

The nickel targets were prepared in 2 series by electrodeposition of enriched ^{64}Ni on Au backing (99.95 %) and were respectively 23.57 μm and 24 μm thick. Monitor foils (12 μm thick ^{nat}Ti , 99 % purity) were interleaved with the targets and one 100 μm thick Al degrader foil was inserted in front of the first Ni foil in the second stack. The foils were stacked together in the Faraday-cup target holder, equipped with a collimator (effective beam diameter on target is 5 mm) and a secondary electron suppresser and the total charge on target was initially derived from the Faraday cup using a digital integrator.

Production of ^{64}Cu was assessed shortly after the end of bombardment (EOB), based on the weak γ-line of 1345.84 keV with an intensity of 0.473 %, using an HPGe detector coupled with the acquisition/analysis software GENIE 2000 (CANBERRA, USA). The samples were measured several times from shortly after the end of the bombardment up to two days, to allow the decay of some Co and Ni contaminants. The source to detector distance was varied from 45 cm, right after the end of bombardment, down to 25 cm for the last measurements series in order to keep dead-times below 10 %. The HPGe detector efficiency curves were determined in the experimental geometry with a standard calibrated ^{152}Eu source. The activities of the irradiated samples were measured without chemical separation.

Results and discussion

The initial beam parameters were estimated from the accelerator settings and from current beam measurements. By taking into account the remeasured cross section for the monitor reaction ^{nat}Ti(p,n)^{48}V over the whole energy range and comparison with the recommended data in the IAEA-TECDOC [12] corrections were introduced. An effective current of 0.153 μA was deduced (Fig.1) and a downshift of 0.3 MeV in the incident particle energy was also necessary, so that the measured monitor reactions and the references values show a good agreement.

The energy degradation in each foil of the stack was calculated with the help of the SRIM 2006 code [13]. The decay and spectrometric characteristics were taken from the NUDAT2 data base [16]. The median beam energy on the first Ni foil was estimated to be about 19.6 MeV with an uncertainty of ± 0.3 MeV. Due to possible variations and inhomogeneity in thickness (5 %), energy spread and straggling, the uncertainties for the energy is increasing throughout the stack and reaches a maximum of 0.7 MeV in the last Ni foil.

The uncertainty on each cross-section was estimated in the standard way [14] by taking the square root of the sum of all individual contributions into quadrature: absolute abundance of the γ-ray taken from NUDAT2 (5 %), determination of the peak areas including statistical errors (5-10 %), the number of target nuclei including non-uniformity (5 %), detector efficiency (5 %) and incident particle intensity (5 %). The total uncertainty of the cross-section values was evaluated to approximately 10-12 %.

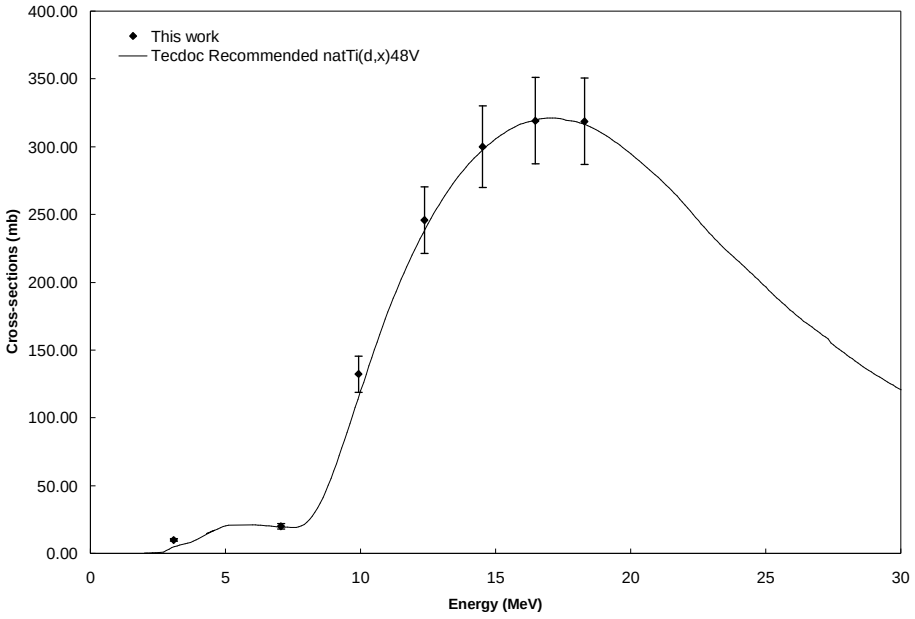

Fig.1. Monitoring of the beam energy and intensity with the $^{nat}Ti(p,x)^{48}V$ reaction and comparison with the recommended values [12]

The measured cross sections for the $^{64}Ni(d,2n)^{64}Cu$ reaction are presented in Fig.2 as a single data set of two irradiations. The excitation function is compared with previous data from literature [5, 15]. The numerical values of the total cross-sections and their uncertainties are presented in Table 1.

The excitation function shows a single peaked shape representing the $^{64}Ni(d,2n)^{64}Cu$ reaction with a practical threshold of about 5 MeV that corresponds well with the calculated one (4.8 MeV). The excitation function has a maximum around 14 MeV of 955 mb in good agreement with the data of Hermanne et al [15]. The cross sections values published by Zweit et al. [5], were multiplied by a factor of 117.3, taking into account the natural abundance of ^{64}Ni and the ratio of the β^+ decay branching used by Zweit et al., (19 %) and the one presently recommended by NUDAT2 (17.6 %) . Our values seem to be 10 % lower than the data of Zweit et al. and also show a downward shift in energy of about 1.3 MeV.

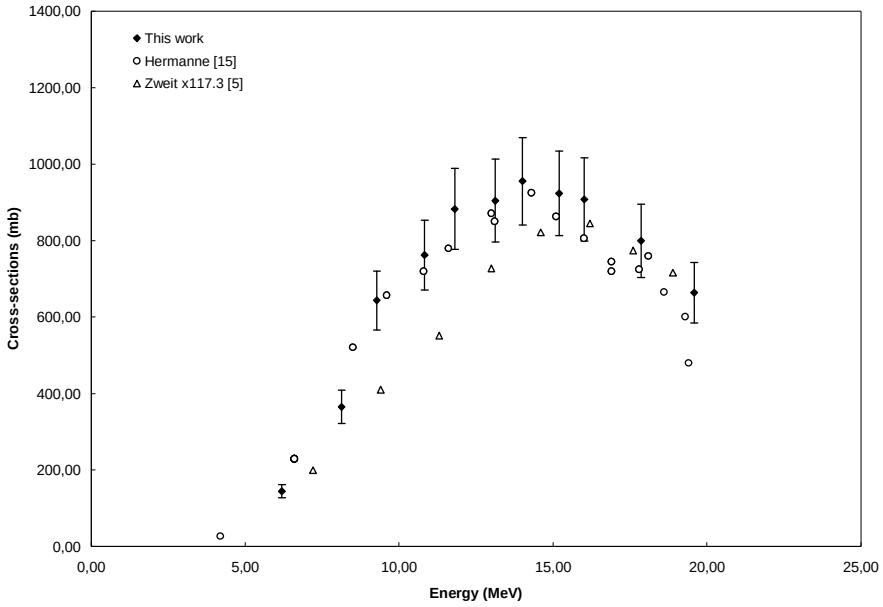

Fig. 2. Excitation function for the $^{64}Ni(d,2n)^{64}Cu$ reaction, comparison with literature values

Table. 1.

Measured cross-sections (mb) and their uncertainties for the $^{64}Ni(d,2n)^{64}Cu$ and $^{64}Ni(d,p)^{65}Ni$ reactions

E_d (MeV)	**$^{64}Ni(d,2n)^{64}Cu$ σ (mb)**	**$^{64}Ni(d,p)^{65}Ni$ σ (mb)**
19.6 ± 0.3	664 ± 66.3	86 ± 8.6
17.8 ± 0.3	800 ± 80.7	102 ± 10.3
16.02 ± 0.3	908 ± 91.7	120 ± 12.1
15.2 ± 0.4	923 ± 93.2	134 ± 13.6
14.02 ± 0.4	955 ± 97.4	128 ± 13
13.1 ± 0.4	905 ± 91.3	164 ± 16.5
11.8 ± 0.5	883 ± 90	173 ± 17.5
10.8 ± 0.5	762 ± 76.9	206 ± 20.8
9.2 ± 0.6	644 ± 65.4	222 ± 22.4
8.1 ± 0.6	365 ± 36.8	231 ± 23.3
6.2 ± 0.8	145 ± 14.7	68 ± 6.8
4.7 ± 1.1		64 ± 6.5

Direct production on ^{64}Ni of ^{61,62}Cu by (d,4n) and (d,5n) is not possible as thresholds are respectively 24 MeV and 33.3 MeV. Traces of contaminating radionuclides of ^{55,56,57,58}Co, ^{56}Ni were detected and could be produced by different reactions on ^{58,60,61,62}Ni impurities present in the target material. As statistics for the activity assessment are low, multiple pathways are possible and exact knowledge of the number of target nuclei for the different routes is missing, no attempt to determine cross sections was undertaken.

Conclusions

In this work, we studied the activation cross-sections for the reaction ^{64}Ni(d,2n)^{64}Cu leading to the formation of ^{64}Cu, by irradiation with deuterons in the range of 5- 20.5 MeV. The values were calculated by assessing the only γ-line of 1346 keV and show a reasonable agreement with previous works [5, 15]. A maximal cross section of more than 955 mb at 14 MeV was found. Only above 18 MeV incident deuteron energy the (d,2n) reaction could be more interesting than the (p,n) reaction at the same energy. As commercially available (E_p = 30 MeV) production accelerators can only reach up to E_d = 15 MeV, the deuteron based production is not competitive for these machines.

A contamination with ^{55,56,57,58}Co, ^{56}Ni produced by (d,xn) and (d,pxn) reactions on the ^{58,60,61,62}Ni impurities of the target could also present. Ni and Co contaminants could be removed by chemical separation, in any case necessary for recovery of the expensive target material.

Acknowledgments

The authors would like to thank Prof. Alex Hermanne from the VUB Cyclotron department in Brussels, Belgium for the help in performing irradiations and useful discussions and to the IBA Company, Radioisotopes department, for providing the enriched material for these experiments.

REFERENCES

1. G. W. Philpott, S. W. Schwarz, , C. J. Anderson, J. M. Connett, K. R. Zinn, M. J. Welch, B. A. Siegel, J. Nucl. Med. **36**, 1818 (1995).
2. J. M Connett, C. J. Anderson, L. W. Guo, K. R. Zinn, B. E. Rogers, G. W. Philpott, M. J. Welch, Proc. Nat. Acad. Sci. USA, 6814 (1993).
3. P. J. Blower, J. S. Lewis, J. Zweit, Nucl. Med. Biol. **23**, 957 (1996).
4. X. Sun, C. J. Anderson, Methods in enzymology Vol. **386**, 237 (2004).
5. J. Zweit, A.M. Smith, S. Downey, H.L. Sharma, Appl. Radiat. Isotopes **42**, 193 (1991).
6. L. Daraban, K. Abbas, F. Simonelli, R. Adam Rebeles, N. Gibson, App. Radiat. Isotopes **66**, 261-264 (2008).

7. M. L. Bonardi, F. Groppi, C. Birattari, L. Gini, C. Mainardi, A. Ghioni, E. Menapace, K. Abbas, U. Holzwarth, M. F. Stroosnijder, J. Radioanal. Nucl. Chemistry, Vol. **257**. No.1, 229-241 (2003).
8. F. Szelecsenyi, G. Blessing, S. M. Qaim, Appl. Radiat. Isotopes **44**, 575 (1993).
9. D. C. Williams, J. W. Irvine, Phys. Rev. **130**, 265 (1963).
10. R. Adam Rebeles, Private communication, 2008. Manuscript submitted to Nucl. Instr. and Meth. B 2008.
11. A. Hermanne, F. Tarkanyi, S. Takacs, Proceedings of the International Conference on Nuclear Data for Science Technology, April 22-27, pp. 1355- 1358, 2007, Nice, France.
12. F. Tarkanyi, S. Takacs, K. Gul, A. Hermanne, M. G. Mustafa, M. Nortier, P. Oblozinsky, S. M. Qaim, B. Scholten, Yu. N. Shubin, Z. Youxiang,
1. IAEA-TECDOC-1211, Co-ordinated Research Project, IAEA, Vienna, p. 77-80 2001. Updated Version January, 2007. Available from http://www-nds.iaea.org/medical.
13. Ziegler J.F., SRIM code (2006). Available from www.srim.org.
14. Guide to expression of uncertainty in measurements, ISO Geneva, ISBN 92-10188-9, 1993.
15. A. Hermanne, F. Tarkanyi, S. Takacs, F. Kovalev, A. Ignatyuk, Nucl. Intrum. And Meth. B **258**, 308- 312 (2007).
16. NUDAT2, Levels and Gamma, National Nuclear Data Center, Brookhaven National Laboratory. Available from http://www.nndc.bnl.gov/nudat2.

STUDIA UNIVERSITATIS BABEŞ-BOLYAI, PHYSICA, LIII, 1, 2008

A RAPID, STRAIGHTFORWARD METHOD FOR SYNTHESIS OF BIO-COMPATIBLE GOLD NANOPARTICLES

MONICA POTARA, DANA MANIU, COSMIN FARCAU, SIMION ASTILEAN*

ABSTRACT. In this study we present a clean, non toxic, environmentally friendly procedure for both the synthesis of gold nanoparticles and their surface modification for biological applications. We use chitosan, a biocompatible, biodegradable, natural polymer as a reducing and protecting agent, due to its unique structural and physicochemical characteristics. The produced hybrid nanoparticles were characterized by UV-vis absorption spectroscopy and transmission electron microscopy (TEM).

Keywords. Nanoparticles, Synthesis, Biological applications

1. Introduction

In the past few years, the synthesis of gold nanoparticles has attracted much attention due to their unusual chemical, electronic and optical properties, compared to bulk metals and potential application in a variety of biomedical areas [1]. Several studies have been focused on developing controllable and reproducible methods to generate various size, shape and self-organized nanoparticles [2]. Among the conventional techniques for aqueous synthesis of gold nanoparticles, probably the most popular method to prepare gold nanospheres dispersed in water is the reduction of $HAuCl_4$ with sodium citrate at high temperature, which was introduced by Turkevitch and later refined by Frens [1, 2]. Another popular procedure to prepare gold nanoparticles has been developed by Brust –Schriffrin [1, 2]. This method combines borohydride reduction with the use of thiol or amine as steric stabilizers, by means of two-phase reaction [1, 2].

However, some disadvantages may be associated with the methods mentioned above. One of these disadvantages is that the chemical agents used are highly reactive and may pose potential biological risks. In the case of organic solvents, it was demonstrated the fact that they make the nanoparticles unsuitable for applications in biosensors [4]. An important condition to use metal nanoparticles in biomedical applications is that they must be non-toxic and biocompatible to both in vitro and in vivo environments. Another requirement is that nanoparticles should be coated with a protective layer to prevent aggregation and to be able to easily attach different biologically relevant molecules on their surface [3, 4]. In this context, new approaches are constantly being developed for both the synthesis of inorganic nanomaterials and their surface modification for biological applications. Insofar as surface modification of

* *Nanobiophotonics Laboratory, Institute for Interdisciplinary Experimental Research and Faculty of Physics, Babes-Bolyai University, M. Kogalniceanu 1, 400084 Cluj-Napoca, Romania*

gold nanoparticles is concerned, the use of microorganisms [5, 6] and biomolecules [7], such as proteins, bacteria and polymers [8, 9], to produce different types of hybrid gold nanoparticles seems to be a relatively new and exciting area of research with a great potential for biomedical applications. In the last years many groups have used biodegradable polymers to generate, stabilize and template gold nanoparticles [10]. In these composite nanoparticles a polymer layer may be physically or chemically bound to the gold core. These polymers are either natural such as polyamino acids, polysaccharide and synthetic such as polyesters, polyamides [10]. Chitosan is attracting increasingly more attention recently for such approach due to its inherent biological and physicochemical characteristics. Chitosan is the (β-1, 4)-linked D-glucosamine, N-deacetylated derivative of chitin, the most abundant natural polymer after cellulose, constituting the exoskeleton of arthropods and cell walls of fungi and yeast [11]. Its chemistry is determined by the presence of largely free amino and hydroxyl groups in its chains [11]. It has unique structural and physicochemical characteristics that differ considerably from typical synthetic polymers. Specifically, chitosan is an inexpensive, biocompatible, antibacterial and environmentally friendly polyelectrolyte, thus lending itself in a variety of applications including biomedical devices, microcapsule implants for controlled release in drug delivery, biodegradable films, wastewater treatment, additives for cosmetics, textile treatment for antimicrobial activity and food science [12]. Its biodegradation leads to the release of aminosugars which can be incorporated into the metabolic pathways for glycosaminoglycans and glycoproteins, or excreted [13]. While chitin is insoluble in most solvents, chitosan is readily soluble in acidic solutions and is thus more suitable for biological applications [11]. In slightly acidic solution its amino groups become protonated, making chitosan a soluble polyelectrolyte with positive charge. This gives chitosan the ability to form complexes with oppositely charged materials [11].

In the synthesis of gold nanoparticles chitosan has been used by Esumi *et. al* as a stabilizing agent [14]. Later, Huang *et al.* found that chitosan is more than a protecting agent and the gold salt can be reduced to zerovalent gold nanoparticles by chitosan itself without any additional reducing agent [15]. Recently, Wei *et al.* have been developed a facile approach to prepare silver nanoparticles using chitosan as a reducing and protecting agent [16].

In this paper, we have been pursuing the possibility of using amine chemistry for surface modification of gold nanoparticles. For this purpose, we used chitosan as a reducing to obtain stable aqueous solutions of gold nanoparticles. We found indeed that chitosan is not only an effective reducing agent but the polymeric macromolecule wraps around the nanoparticles, isolating them from each other and, thus preventing the agglomeration. The advantages of using chitosan chemistry for surface modification of nanogold are many, the possibility of complexing a large variety of biomolecules such as proteins and saccharides being one of the most important. Chitosan will not introduce any environmental toxicity in the reduction and stabilization process of gold nanoparticles.

2. Experimental section

Chitosan flakes (> 75% deacetylated) were purchased from Aldrich. $HAuCl_4$ was obtained from Aldrich and used without further purification. Glacial acetic acid (99.8 %) was procured to Sigma-Aldrich and was diluted to 1% aqueous solution before use. Solutions were prepared using deionized water. All other reagents employed for substrate and solutions preparation were of analytical grade. All glassware used was cleaned with aqua regia solution ($HCl:NO_3$ 3:1) and then rinsed thoroughly with deionized water.

Before the experiment, a stock solution of 1 mg/mL chitosan was prepared by dissolving a certain amount of the polymer in 1% acetic acid solution. Due to the poor solubility of chitosan molecule, the mixture was kept overnight until a clear solution was obtained. An aqueous solution of $HAuCl_4$ (3 ml, 10^{-3} M) was mixted with chitosan solution (18 ml, 0,1 mg/ml) and the mixture was heated at 70^0 C under magnetic stirring until a red solution was obtained.

A JEOL JEM 1010 transmission electron microscope was used to image and determine the size of gold nanoparticles. Uranyl acetate dihydrate was used as the negative contrast agent.

The size distribution histogram of gold nanoparticles was determined by digital processing of transmission electron microscopy images using image processing software Image J.

Absorption measurements were performed on a Jasco V-530 UV-VIS spectrophotometer.

3. Results and discussion

The gold colloidal suspension was prepared by the following procedure: 3 ml of 10^{-3} M $HAuCl_4$ were added to18 ml of 0.1 mg/ml chitosan solution, and then the mixture was heated to 70^0C and kept at this temperature under magnetic stirring. After several minutes, the light yellow solution turned colorless, light pink, mauve and then red, indicating the formation of gold nanoparticles. The reaction time was prolonged to 2 h. The heat source was then removed and the solution was allowed to cool at room temperature while stirring. The resulting aqueous nanoparticles solution is stable and no evidence of flocculation after four months of storage at 4^0C was observed.

Chitosan has been used to directly reduce hydrogen tetrachloroaurate ($HAuCl_4$), producing gold nanoparticles formed within the polymer matrix. The obtained sample in aqueous suspension was then characterized by UV-vis surface plasmon absorption spectroscopy. The UV-vis absorption spectrum recorded for the resulting solution, in Figure 1 b, shows a sharp peak centered at 525 nm, which is a typical surface plasmon band (SPB) of spherical gold nanoparticles with 20-30 nm size range. For comparison, in Figure 1 the UV-vis spectrum of gold nanoparticles synthesized following Turkevich-Frens method is inserted.

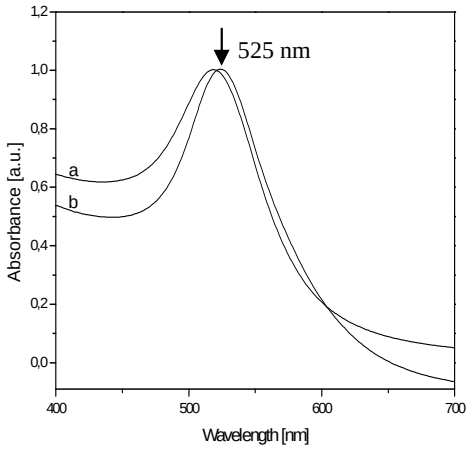

Figure 1. Normalized UV-vis absorption spectra of gold nanoparticles synthesized by: a) citrate-assisted reduction and stabilization and b) chitosan reduction and stabilization

To have a clear view about the shape and size distribution of the prepared sample, the transmission electron microscopy (TEM) images of the colloidal solution were analyzed, as well. Figure 2 A shows a representative TEM picture of as synthesized gold nanoparticles. A careful analysis of the TEM images reveals that the product as prepared is mainly composed of spherical gold nanoparticles, dispersed in solution, together with a few triangular particles. Figure 3 presents a histogram of gold particle size distribution with the mean particle diameter D_n = 27 nm and standard deviation SD = 11 nm. These results were obtained by analyzing a number of 100 nanoparticles.

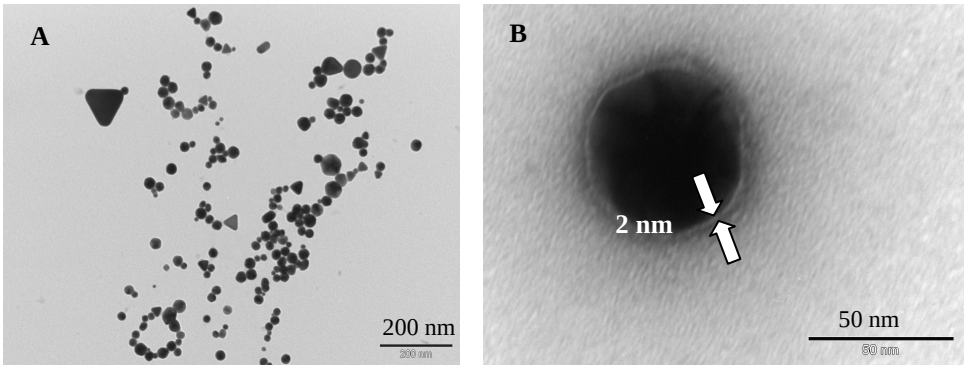

Figure 2. A) TEM image of gold-chitosan nanocomposites, B) negative contrast TEM image of a single gold spherical nanoparticle coated by chitosan

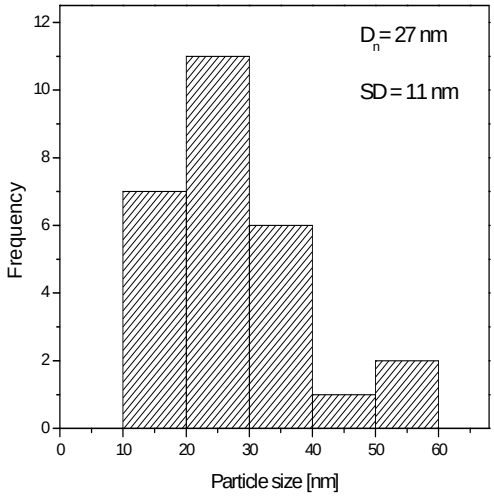

Figure 3. The histogram for the size distribution of as synthesized gold nanoparticles

The reduction of $AuCl^-_4$ ions to neutral atoms is due to charge transfer from the functional groups normally present in chitosan. Furthermore, the polyelectrolytic character of chitosan permits the stabilization of the gold nanoparticles and control of particle growth, acting as a biotemplate. Thus, when $HAuCl_4$ was mixed with chitosan solution the electrostatic interactions between chitosan macromolecules due to its amino groups and $AuCl^-_4$ ions act as an effective driving force in the generation and stabilization of gold nanocomposites. Hence, the polymeric molecules are adsorbed on the surface of produced nanospheres and keep them segregated for longer time. C. Sun et al. [17] found that the chitosan chain was broken during the preparation of chitosan stabilized gold nanoparticles. This fact allows the restructuring of chitosan chain in the synthesis of gold nanocomposites. Thus, a possible explanation for the size variation of as obtained sample is that not all the particles formed are immediately covered by chitosan. In this way, parts of the smaller gold nanoparticles clustered to form bigger ones during the reaction time. The presence of some triangular nanoparticles can be attributed to the selectivity of polysaccharide in covering the nanoparticles surface, resulted from the specificity of the interaction between polymeric molecules and different crystallographic planes. Thus, the amino groups in chitosan adsorb only to particular faces, inhibiting the growth of these faces by lowering their surface energy and leading to the preferential orientation and growth of other faces.

The binding sites in the chitosan chain hold the nanoparticles keeping them away from one another and thus providing stability to nanoparticles. Figure 2 B illustrates a negative contrast TEM picture of a single gold nanoparticle coated by polymeric chitosan which appears as a white ring around the particle. This result demonstrates the formation of gold particles inside the nanoscopic polysaccharide

templates. The charge on the gold nanoparticles surface is determined by the molecule that coats the particles. In our case, of chitosan stabilized nanocomposites the electric charge could be positive due to the polycationic character of the soluble biopolymer.

4. Conclusions

The preparation of environmentally and possibly biologically friendly gold nanoparticles embedded in polymers is easily and rapidly accessible with this methodology. The use of polymeric chitosan for the formation and matrix incorporation of gold nanoparticles offers an avenue to biocompatible polymer–gold particle composites. The obtained composites combine the unique optical properties of gold nanoparticles with the chitosan versatility to easy attach different biological entities on its surface and make them good candidates for biosensing applications.

Acknowledgments

Financial support from the Romanian National Authority for Scientific Research in the frame of the CEEX program (Project No. 71/2006) is gratefully acknowledged.

REFERENCES

1. M.C. Daniel, D. Astruc, *Gold nanoparticles: Assembly,supramolecular chemistry, quantum-size-related properties and applications toward biology, catalysis and nanotechnology* Chem. Rev. 104, 2004, 293
2. I. P.-Santos, J. P.-Juste,L. M. Liz-Marzan, *Preparation of noble metal colloids and selected structures* Topics in Fluerescence Spectroscopy 8, 2005
3. T. Gacoin, *Nanoparticles: Functionalization and elaboration of materials,* Nanostructured and Advanced Materials,2005, 217–227
4. E. Katz, A. N. Shipway, I. Willner, *Chemically Functionalized Metal Nanoparticle:, Synthesis, Properties and Applications*
5. P.Mohanpuria, N.K.Rana, S.K.Yadav, *Biosynthesis of nanoparticles: technological concepts and future applications*, J.Nanopart.Res. 10, 2008, 507-517
6. D. Mandal, M. E. Bolander, D. Mukhopadhyay, G. Sarkar, P. Mukherje, *The use of microorganisms for the formation of metal nanoparticles and their application,* Appl. Microbiol. Biotechnol., 2006, 485
7. M.M. Tomczak, J.M. Slocik, M.O. Stone, R.R. Naik, *Bio-based approaches to inorganic material Synthesis,* Biochemical Society Transactions, 35, 2007, 512-515
8. H.Yi, L.Q.Wu, W.E.Bentley, R.Ghodssi, G.W.Rubloff, J.N.Culver, G.P.Payne, *Biofabrication with Chitosan*, Biomacromolecules 6, 2005, 2881-2894
9. S.-H. Yu H. Colfen, *Bio-inspired crystal morphogenesis by hydrophilic polymers,* Journal of Materials Chemistry, 14, 2004, 2124-2147
10. A. Huczko, *Template-based synthesis of nanomaterials*, Appl. Phys. A 70**,** 2000, 365–376

11. M. Rinaudo, *Chitin and chitosan: Properties and applications*, Prog. Polym. Sci. 31, 2006, 603
12. M.N.V.Ravi Kumar, R.A.A.Muzzarelli, C.Muzzarelli, H.Sashiwa, A.J.Domb, *Chitosan Chemistry and Pharmaceutical Perspectives*, Chem.Rev. 104**,** 2004, 6017- 6084
13. L. Balau, G. Lisa, M.I. Popa, V. Tura, V. Melnig, *Physico–chemical properties of Chitosan films* Central European Science Journal of Chemistry, 2, 2004**,** 638-647
14. D. Wei, W. Qian, Yi Shi, S. Ding,Y. Xia, *Mass synthesis of single-crystal gold nanosheets based on chitosan*, Carbohydrate Research 342, 2007, 2494–2499
15. H. Huang, X. Yang, *Synthesis of Chitosan-Stabilized Gold Nanoparticles in the Absence/Presence of Tripolyphosphate*, Biomacromolecules, 5, 2004, 2340-2346
16. D. Wei, W. Qian, *Facile synthesis of Ag and Au nanoparticles utilizing chitosan as a mediator agent*, Colloids and Surfaces B: Biointerfaces, 2007
17. C. Sun, R. Qu, H. Chen, C. Ji, C. Wang, Y. Sun, B. Wang, *Degradation behavior of chitosan chain in the green' synthesis of gold nanopartilces*, Carbohydrate Research, 2008

STUDIA UNIVERSITATIS BABEŞ-BOLYAI, PHYSICA, LIII, 1, 2008

COLORIMETRIC DETECTION OF SINGLE - AND DOUBLE-STRANDED DNA ON GOLD NANOPARTICLES

S. BOCA[1], I. LUPAN[2], O. POPESCU[2], S. ASTILEAN[1]

ABSTRACT. In this work we report the use of gold nanoparticles (AuNPs) for optical detection of single and double-stranded DNA. The linkage of DNA sequences to gold nanoparticles was demonstrated by the modification of spectral position and intensity of plasmon resonance band and the chemical stabilization that DNA confers to gold particles against a standard aggregation test.

Keywords. Gold nanoparticles, Optical detection, Plasma resonance in DNA

Introduction

The use of colorimetric tests on various (bio)molecular detection methods has became increasingly important in fields like medical research and diagnosics, or in food and drug monitoring [1], [2]. With respect to the DNA detection, many schemes that exploit the color conferred by plasmon resonance to oligonucleotide functionalized gold nanoparticles have been developed [3], [4]. Even that these detection schemes have the simplicity of a colorimetric readout, they got the significant disadvantages that they require the functionalization of nanoparticle surface or of DNA sequence with specific chemical groups as sulfhydryl (SH) or amine (NH_2).

Due to their different conformational and electrostatic properties, single-stranded DNA (ssDNA) and double-stranded DNA (dsDNA) have the propensity to preferentially adsorb on negatively charged gold nanoparticles in aqueous solution. It has already been demonstrated that under certain conditions, ssDNA attaches to gold nanoparticles, whreas dsDNA does not [5]. The binding of oligonucleotides to gold surface can be attributed not only to the electrostatic interactions but also to the presence of the functional groups (amines, carbonyls) presented in nucleosides [6].

The successful linking of oligonucleotides to gold nanoparticles changes the immediate environment which leads to a modification of the position and aspect of the plasmon resonance band. Based on this idea, we studied the binding affinity of single stranded and hybridized 31-mers DNA on 20 nm gold nanoparticles using a colorimetric assay. As demonstrated in previous studies, the color modification is due to the aggregation of colloidal gold particles [7]. For the investigation of the interaction between DNA and gold nanoparticles, UV-Vis absorption spectroscopy was employed. Two parameters were taken into account: the interaction time and the analyte concentration. In both cases a 2-3 nm red-shifting of the surface plasmon band has

[1] *Nanobiophotonics Laboratory, Institute for Interdisciplinary Experimental Research, Babes-Bolyai University, T. Laurian 42, 400271 Cluj-Napoca, Romania*

[2] *Molecular Biology Center, Institute for Interdisciplinary Experimental Research, Babes-Bolyai University, T. Laurian 42, 400271 Cluj-Napoca, Romania*

been noticed and when increasing the DNA concentration a diminution of the absorbance intensity has also been observed. Moreover we have shown that the adsorption of ssDNA stabilizes the nanoparticles at concentrations of salt that usually screens the negative charges presented on their surface.

Experimental

Spherical gold (Au) nanopaticles of approximately 20 nm were synthesized by a chemical method which uses the reduction of chloroauric acid ($HAuCl_4$) with sodium citrate ($C_6H_5Na_3O_7$) [8]. The single stranded DNA (abbreviated ssDNA) with the following sequence: 5'-GGA CTC GAG TTA CTC TTT TAT GTT CCA CTTC-3' and its complementary sequence (denoted ssDNAc) were brought to the 60 µM molar concentration. The hybridization of the two complementary sequences was realized by mixing equal quantities of the as obtained solutions, resulting double stranded DNA (dsDNA).

The stabilization of Au nanoparticles was made by adding 5 µL ssDNA solution to 500 µL gold colloid. The mixuture was then aged for 10 minute. For aggregation tests, 200 µL of a solution of 0.2 M NaCl was introduced in the cuvettes containing the mixtures of gold colloids and the oligomers. Same procedures were followed for ssDNAc and dsDNA. UV-Visible spectroscopic measurements were carried out on a Jasco V-530 UV-Vis spectrophotometer before and after the addition of salt. In the second experiment, the interaction time was increased at 3 days. The second parameter that has been taken into account was the oligonucleotide concentration. For this reason, ten samples were prepared for both ssDNA and ssDNAc, by increasing the molar concentration, from 10 µM to 100 µM. The prepared solutions were kept at room temperature for three days and after this period, optical absorbance measurements were employed.

Results and Discussion

As already mentioned, in normal conditions, Au nanoparticles are stable in aqueous solution due to the electrostatic repulsion conferred by the presence of citrate ions on their surface [9]. Therefore, the sodium citrate is used not only as a reducing agent but also as a stabilizer. If strong acids, bases or salts are introduced in a gold colloid, the negative charges are screened and the nanoparticles start to aggregate. This aggregation process is clearly seen by the color modification of the colloid which is also reflected in a change of the aspect and position of plasmon resonance band [10].

The stabilization of gold nanoparticles through binding various (bio)molecules (and from this class DNA) on their surface has been largely studied [11]. One of the drawbacks of using molecules to stabilize gold nanoparticles is that they have to be functionalized with certain chemical groups to bind on nanoparticles. In our experiments instead, we used simple, non-functionalized oligonucleotides for attaching on gold nanoparticles. To test their binding affinity, we took aggregation tests using NaCl solution that was introduced in the samples with gold nanoparticles and DNA sequences. The salt was used for that it weakens the electrostatic interaction between the oligonucleotides and the negatively charged nanoparticles. We observed that for the

samples aged for three days the color of the solutions turned blue immediately after the NaCl solution was introduced. This denotes that all the solutions aggregated, which means that there was no DNA molecules presented on the nanoparticles surface. This is well illustrated both in photographic images from Figure 3 and in the measured spectra shown in Figure 1, by a dramatic decrease of the absorbance and mostly by the appearance of a second plasmonic band at higher wavelength, which is specific to aggregates of nanoparticles.

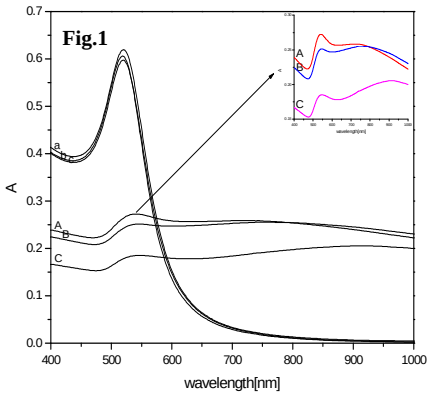

Fig. 1. Absorbance spectra of gold colloids mixed with: a- ssDNA; A-ssDNA with NaCl solution; b-ssDNAc; B- ssDNAc with NaCl; c- dsDNA; C- dsDNA with NaCl; the solutions were aged for 10 minutes.

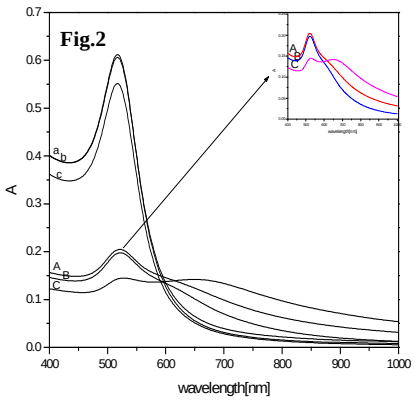

Fig. 2. Absorbance spectra of gold colloids mixed with: a ssDNA; A-ssDNA with NaCl solution; b-ssDNAc; B- ssDNAc with NaCl; c- dsDNA; C- dsDNA with NaCl; the solutions were aged for 3 days.

Fig. 3. Photographic image of gold colloid mixtures with (from left to right): ssDNA, ssDNAc and dsDNA in which NaCl solution was introduced.

In the next experiment, time parameter was modified from ten minutes to three days. Same experiment procedures were carried out. In this case, after the aggregation test was taken, the maintainance of the color of the colloidal solutions was observed for the samples containing ssDNA. For the sample in which dsDNA was introduced, the solution changed its color from red to blue after the adding of NaCl, which denotes the fact that the aggregation phenomena took place. Figure 2 presents optical absorption spectra of colloidal solutions with DNA sequences, before and after the aggregation test.

We observe that the spectra of the colloidal solutions with single-stranded DNA present only one resonance plasmonic band shifted with 3-4 nm after the aggregation agent was added. This shifting is a confirmation of the fact that DNA sequences bound to gold nanoparticles, therefore modifying the environment around them. On the contrary, the spectrum of the colloidal solution with dsDNA shows two distinct bands, one specific to isolated particles and another one, which corresponds to agglomerates of nanoparticles. Therefore, in the first case, ssDNA attached to gold nanoparticles and conferred them stability, while dsDNA, due to its rigid geometry didn't.

The second parameter that has been taken into account was the oligonucleotides concentration. Ten samples have been prepared for ssDNA and ssDNAc. Samples were aged for three days and then absorbance spectroscopy measurements were employed, taking gold colloidal solution without DNA as reference. For all samples, the spectra present a 2-3 nm shifting of plasmon resonance band from that of 520 nm, specific to standard colloid (Figures 4 and 5). Another interesting observation is that the absorbance is higher for small DNA concentrations, while it decreases as the DNA concentrations is augumented.

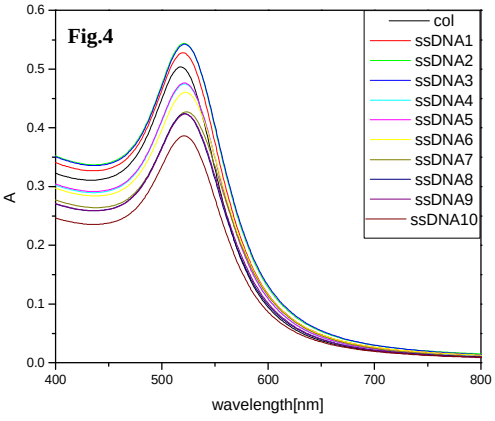

Fig. 4. Absorbance spectra of gold colloids mixed with various molar concentrations of ssDNA (from 10 µM (ssDNA 1) to 100 µM (ssDNA 10).

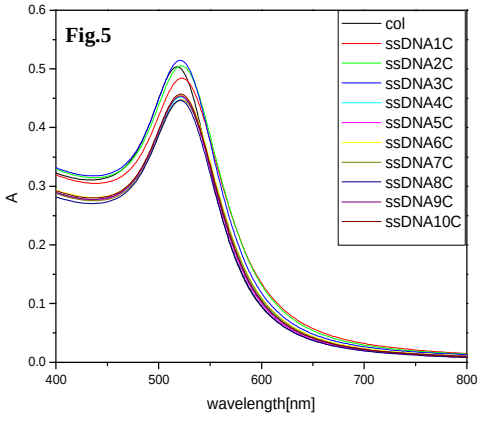

Fig. 5. Absorbance spectra of gold colloids mixed with various molar concentrations of ssDNAc (from 10 µM (ssDNA 1C) to 100 µM (ssDNA 10C).

From the DNA samples and that of complementary sequences, same quantity was taken and then the two sequences were mixed. In this way, the hybridization of the complementary DNA sequences in the colloidal solution was accomplished. The obtained samples were kept at room temperature another three days, and then absorbance spectra were measured. The spectra illustrated in Figure 6 present a 2-3 nm shifting of the plasmon resonance band from that of standard colloid and an increase of the absorbance for small DNA concentrations. As the DNA concentration is increased the decrease of the absorbance was observed.

The aggregation test was made for the solution with the biggest and smallest DNA concentration. The standard colloidal solution was taken as reference. The color modification of the colloidal solution without DNA and that of the solution with the smallest concentration is observed (Figure 7), while the solution which contains a bigger oligonucleotide concentration kept its red, initial color.

Conclusions

In our study we demonstrated that there is a clear dependence on the type of the DNA sequence, whether it is single or double-stranded, on their binding affinity for the surface of gold nanoparticles. The different ability of oligonucleotides to attach on gold particles allows us to design an assay to determine whether a given sample contains single or double-stranded DNA. By aggregation tests we demonstrated that the DNA stabilizes the particles at salt concentrations that usually screens the negative charges presented on their surface.

Acknowledgement

This work was supported by CEEX project No.71/2006.

REFERENCES

1. S. Chah, M. R. Hammond, R. N. Zare, *Chemistry & Biology*, Vol. 12 (2005), 323.
2. D. G. Thompson, A. Enright, K. Faulds, W. E. Smith, D.Graham, *Anal. Chem*., 80 (2008), 2805.
3. R. Elghanian, JJ Storhoff, RC Mucic, RL Letsinger, CA Mirkin, *Science*, 277 (1997), 1078.
4. R. J. Heaton, A. W. Peterson, R. M. Georgiadis, *Proc. Natl. Acad. Sci. USA*, 98 (2001) 3701.
5. H. Li, E. Nelson, A. Pentland, J. Van Buskirk and L. Rothberg, *Plasmonics*, 2 (2007), 1557.
6. L. M. Demers, C. A. Mirkin, R. C. Mucic, R. A. Reynolds, R. L. Letsinger, R. Elghanian, G. Viswanadham, *G. Anal. Chem*, 72 (2000), 5535.
7. H. Li, L. Rothberg, *Proc. Natl. Acad. Sci. USA*, 101 (2004), 14036.
8. G. Frens, *Nat. Phys. Sci*., 20 (1973), 241.
9. M.-C. Daniel, D. Astruc, *Chem. Rev*. 104 (2004), 293.
10. P. K. Jain, X. Huang, I. H. El-Sayed, M. A. El-Sayed, *Plasmonics*, 2 (2007), 107.
11. J. J. Storhoff, R. Elghanian, C. A. Mirkin, R. L. Letsinger, *Langmuir* 18 (2002), 6666.

STUDIA UNIVERSITATIS BABEŞ-BOLYAI, PHYSICA, LIII, 1, 2008

DETECTION OF Zn^{2+} IONS IN WATER BY LOCAL SURFACE PLASMON RESONANCE (LSPR) SENSORS

D. S. TIRA[1], M. POTARA[1], F. TODERAS[1], S. ULINICI[2], S. ASTILEAN[1]

ABSTRACT. In this work we develop sensitive and specific sensors for Zn^{2+} ions detection, based on local surface plasmon resonance (LSPR) of gold nanoparticles, without using any chelating ligands.

Keywords. Sensors, Ion detection, Surface plasmon resonance

1. Introduction

Environmental pollution has become a serious problem for the last decades since human activity has produced huge amounts of contaminants every second. Heavy metals are known as widespread and dangerous pollutants, released mostly as a result of industrial activity. Mercury, lead and plutonium are considered the most toxic elements[1]. Exposure to high Hg levels, for instance, causes irreversible changes of heart, brain or immune system activity.[2] Zinc is notably used in the automobile industry or in metallurgy to prevent rust and corrosion of steel. It is also used as parts of the containers of batteries, in contemporary pipe organs as a substitute of lead, as white pigment in water-colours or paints (zinc oxide) and also as a deodorant (zinc chloride). Zinc have beneficial effects in very small amounts as essential nutrients of human body, therefore it is included as a daily vitamin and mineral supplement. It posses anti-oxidant properties and speed up the healing process after an injury. Yet, Zn ions may cause health problems in high levels due to the high solubility in the acid of stomach. Excessive absorption of Zn ions may also suppress copper and iron absorption or even kill aquatic plants and fishes[3]. Therefore, the detection of heavy metals became of great botanical, nutritional and environmental interest due to their accumulation in various organisms and their high toxicity.[1] Many studies have been focused on developing selective and sensitive sensors for reliable screenings of these analytes in water, air or soil. Most of them rely on special NP properties, such as fluorescence[2], nonlinear optical properties (NLO)[1,4] or surface plasmon resonance[5,6]. Fluorescence has proved its efficiency for the last 50 years in investigation of aromatic organic compounds in water[7] and became lately a reliable tool for Hg^{2+} ions detection[2]. Several recent studies focused on using NLO of gold NPs in order to screen the presence of

[1] *Nanobiophotonics Laboratory, Institute for Interdisciplinary Experimental Research and Faculty of Physics, Babes-Bolyai University, Cluj-Napoca, Romania*
[2] *ICPE, Bistrita, Romania*

different metal ions (Hg^{2+}, Pb^{2+}, Fe^{2+}, Cd^{2+}, Zn^{2+}, Cu^{2+} etc.) in aqueous systems. [1,4]. Experimental data demonstrate the ultrasensitivity of this method but also its cross-sensitivity towards different types of metal ions, providing excellent results only for Hg^{2+} ions[4]. A reliable, rapid and sensitive tool for detecting heavy-metal ions relies on localized surface plasmon resonance (LSPR) of gold or silver NPs. Previous studies, based on this property, focused on detection of Pb^{2+}, Cu^{2+} and Zn^{2+} ions, which have been screened using chelating ligands, such as 2,6-pyridinedicarboxylic acid (PDCA)[4], 11-mercaptoundecaionic acid (MUA)[1], chitosan[6] or DNA[8].Use of chelating ligands make the study more expensive but still LSPR remains an ideal candidate that provide low limits of detection. In this work we develop sensitive and specific sensors for Zn^{2+} ions detection, based on local surface plasmon resonance (LSPR) of gold nanoparticles, without using any chelating ligands.

2. Theory

Localized surface plasmon resonance (LSPR) is based on an unique optical property of noble metals nanoparticles to exhibit a strong UV-vis absorption band into the visible part of the electromagnetic spectrum. This phenomenon occurs when the nanoparticles interact with the electromagnetic field of the incoming light.

The electric field induces a polarization of the conduction electrons with respect of the ionic core. The charge difference acts as a restoring force and produces oscillations of the electrons which execute a coherent motion. If the frequency of the electromagnetic component of light is resonant with the electrons motion, a strong absorption will appear, yielding the surface plasmon band (SPB).[9].

Garnet Mie was the first who explained theoretically the surface plasmon resonance by solving Maxwell's equations. According to his theory, the total cross section composed of the SP absorption and scattering is given as a summation over all electric and magnetic oscillations. He considered spherical particles having the same dielectric constant as the bulk metal and obtained, in the dipole approximation, for the extinction cross section the following expression:

$$\sigma_{ext} = \frac{9V\varepsilon_m^{3/2}}{c} \cdot \frac{\omega\varepsilon_2(\omega)}{[\varepsilon_1(\omega)+2\varepsilon_m]^2+\varepsilon_2(\omega)^2}$$

where ω represents the angular frequency of the exciting light, V is the particle volume, c is the speed of light, ε_m represents the dielectric function of the surrounding medium, while $\varepsilon = \varepsilon_1(\omega)+ \varepsilon_2(\omega)$ is the dielectric function of the metal.

The resonance condition is based on the equality $\varepsilon_1(\omega)= -2\ \varepsilon_m$, considering ε_2 weakly dependent on ω or very small[10].

SPB has been extensively studied and provides information on particle size and shape, local dielectric constant, temperature and interparticle distance.[11] The main characteristics of the SPB of gold nanoparticles are: 1) its position around 520 nm; 2) its sharp decrease with decreasing core size, when the diameter of the

core is 1,4-3,2 nm; 3) steplike spectral structures for nanoparticles with core diameters between 1,1 and 1,9 nm. SPB is absent for gold nanoparticles with core diameter less than 2 nm, as well as for bulk gold. The SPB maximum decrease when the mean diameter of nanoparticles decreases. The refractive index of the solvent induces a shift of the SPB. The ligand shell alters the refractive index and causes either a red or a blue shift. SPB is shifted to higher wavelength as the spacing between particles is reduced[9]. These properties are fundamental for optical bio/chemosensing as small amounts of analytes, placed near the NPs surface can be detected directly by a change in the absorption spectrum[12]. The presence of different substances induces a shift of the SPB that can be used to detect molecule-induced changes surrounding the nanoparticles. There are four different mechanisms that cause changes in the LSPR: a) resonant Rayleigh scattering; b) nanoparticles aggregation; c) charge-transfer interactions at nanoparticles surfaces and d) local refractive index changes.[13].One of the methods of detection that rely on monitoring the changes in the position of the LSPR is UV-vis spectroscopy.

3. Experimental

3.1. Colloids and samples preparation

Gold colloid was prepared following Turkevitch-Frens method, as was described elsewhere [14]: 500ml of 1mM $HAuCl_4$ (Aldrich) was brought to boil on a magnetic stirring hot plate, with vigorous stirring. 10ml of 38,8mM Na_3 citrate (Aldrich) was all at once added to the solution, stirring continuously. Stirring and boiling has been continued for 10-15 min after the solution colour became deep-red burgundy. The solution was removed from heat and kept stirring until got cold. Then the volume was adjusted to 500 ml adding ultrapure water.

TEM samples were prepared by drying small drops of samples on a carbon-coated copper grid, followed by drying at room temperature.

All glassware and magnetic stir bars were cleaned in aqua regia (one part of concentrated HNO_3 mixed with three parts of concentrated HCl of the same volume) and rinsed with deionized water. Deionized water was also used for preparation of colloids and all the other samples.

3.2. Experimental measurements

Absorption spectra of the colloids and solutions obtained by mixing the colloids with different concentrations of Zn^{2+} were investigated using a Jasco V-530 UV-VIS spectrophotometer.

The images of nanoparticles and structures obtained after interaction with metal ions were recorded with a JEOL JEM transmission electron microscopy.

4. Results and discussion

The gold colloid prepared as described in Section 3, was investigated using the UV-vis spectroscopy and TEM (Fig.1 and Fig.2):

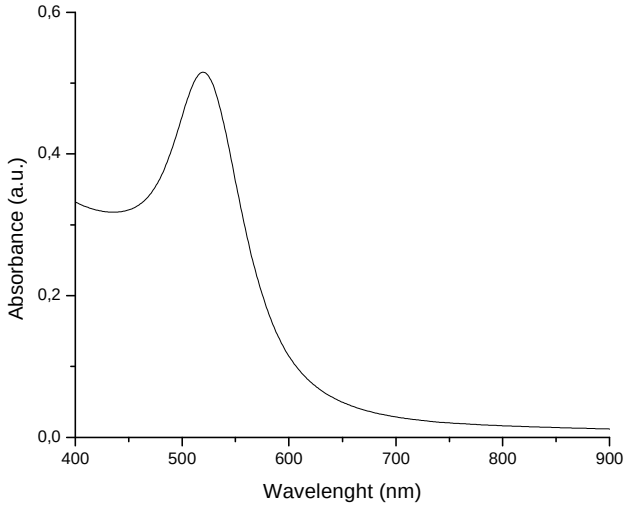

Fig.1. UV-vis absorption spectrum of colloidal suspension of gold nanoparticles

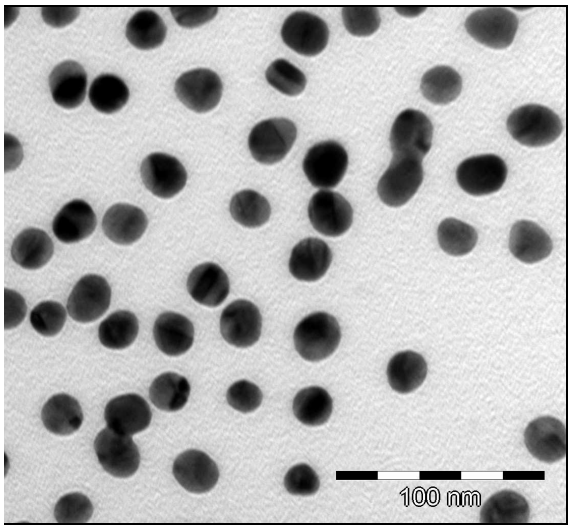

Fig.2. TEM micrograph of the obtained gold nanoparticles

Gold nanoparticles show an LSPR band with λ_{max} = 520 nm, corresponding to a diameter ranging from 10 to 20 nm[6]. TEM image confirms that the nanoparticles are approximately 20 nm in diameter and have spherical shape.

The effect of addition of different concentrations of Zn2+ ions was investigated by observing the colour change of the colloid (Fig.3) and the changes in the absorbance of the LSPR peak (Fig.4). The limit of detection (LOD) obtained following this method was $1,25*10^{-6}$ M concentration of Zn^{2+} ions, therefore we consider this method very sensitive.

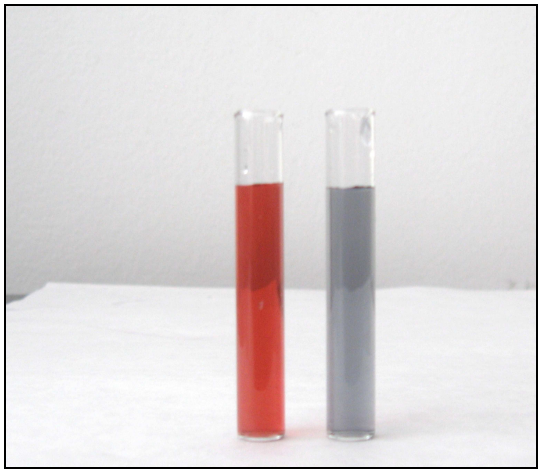

Fig.3. Photographic image of gold colloid before (left) and after addition of $(C_2H_3O_2)_2Zn$, 30 mM (right). The real colour of the gold colloid is red, while the real colour of the mixture is blue.

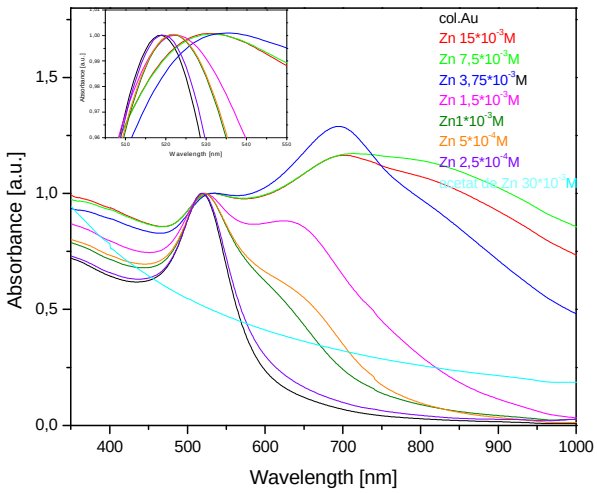

Fig.4. Series of UV-vis absorption spectra obtained by exposing the gold colloid to different concentrations of Zn^{2+} ions.

The series of absorption spectra in Fig.4 show a broad and redshifted second band that appears at the highest concentrations of Zn^{2+} ions used during our experiment. To understand the nature of interaction of gold nanoparticles with the metal ions, we also performed TEM studies of the sample obtained after addition of zinc acetate solution, 7,5mM (Fig.5):

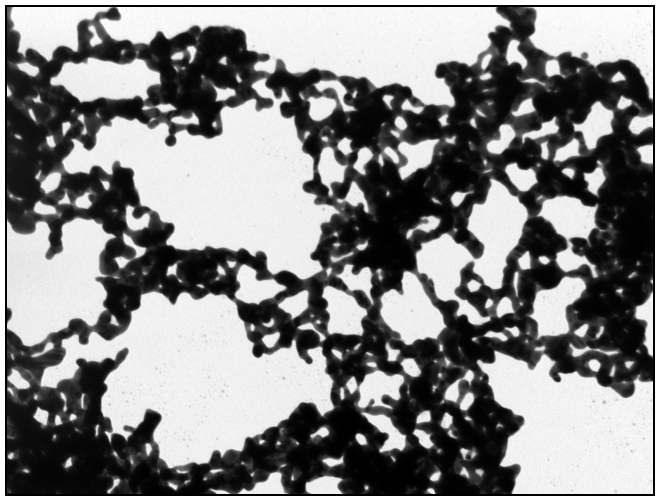

Fig.5. TEM micrograph of the sample obtained by mixing gold colloid with zinc acetate, 7,5mM

Fig.4 shows an image of the structures obtained after the interaction of the gold nanoparticles with Zn^{2+} ions. Careful examination of the micrograph revealed the formation of gold network-like nanowires. Formation of this network-like nanowires may be explained if we consider that the gold nanoparticles become thermodynamically unstable after mixing with the zinc acetate solution. Previous researches found two ways to reduce the high surface energy of unstable nanoparticles: 1) rapid growth of the particles through permanent addition of Au atoms or 2) assembly and fusion of the unstable nanoparticles into larger aggregates[15]. Different investigations[16,17] revealed that unstable nanoparticles have shown more tendency to undergo fusion towards stable assembly formation. Therefore we suppose that gold nanoparticles stabilized more likely through assembly way. The way the network-like nanowires were setted up is under current investigation and further work is in progress.

5. Conclusions

Our study demonstrates that gold nanoparticles exhibit clear recognition and sensitive attributes for detection of heavy-metal ions in aqueous solution. Zn^{2+} ions could be detected using gold colloid, with a limit of detection (LOD) of $1,25*10^{-4}$ M. This method has several advantages, such as:

1) the colour change provides one of the most rapid visual sensing of the ions;

2) UV-vis spectroscopy remains one of the most simple, reliable and sensitive tool to detect small amounts of analytes;

3) the low-cost of this method, which relies also on the absence of any chelating ligand.

Though we have demonstrated the sensitivity of our method only for Zn^{2+} ions in water, we believe that our work remains a good starting point for environmental studies.

Aknowledgements

The authors gratefully aknowledge support from the Romanian National Authority for Research in the frame of CEEX program (Project No. 71/2006 / Nanobiospec / Matnatech).

REFERENCES

1. Y. Kim, R. C. Johnson, J. T. Hupp, Nano Letters, 1, 2001, 165-167.
2. G. K. Darbha, A. Ray, P. C. Ray, Acsnano, 1, 2007, 208-214.
3. EPA guidelines, http://oasp.epa.gov.
4. G. K. Darbha, A. K. Singh, U. S. Rai, E. Yu, H. Yu, P. C. Ray, J. Am. Chem. Soc.,130, 2008, 8038-8043.
5. A. J. Haes, R. P. Van Duyne, SPIE, 5221, 2003, 47-58.
6. A. Sugunan, C. Thanachayanont, J. Dutta, J. G. Hilborn, Sci. and Tech. of Adv. Mat., 6, 2005, 335-340.
7. N. Hudson, A. Baker, D. Reynolds, River. Res. Applic. 23, 2007, 631-649.
8. J. Liu, Y. Lu, J. Am. Chem. Soc., 125, 2003, 6642-6643.
9. M.-C. Daniel, D. Astruc, Chem. Rev., 104, 2003, 293-346.
10. S. Link, M. A. El-Sayed, Annu. Rev. Phys. Chem. 54, 2003, 331-366.
11. P. K. Jain, X. Huang, I. H. El-Sayed, M. A. El-Sayed, Plasmonics, 2, 2007, 107-118.
12. K. A. Willets, R.P.Van Duyne, Annu. Rev. Phys. Chem., 58, 2007, 267-297.
13. A. J. Haes, R. P. Van Duyne, Anal. and Bioanal. Chem.,10.1007/s00216-004-2708-9.
14. M. Baia, F. Toderas, L. Baia, J. Popp, S. Astilean, Chem. Physics Letters, 422, 2006, 127-132.
15. C. J. Kiely, J.Fink, M. Brust, D. Bethell, D.J. Schiffrin, Nature, 396, 1998, 444-446.
16. T. Yonezawa, S. Onoue, N. Kimizuka, Chem. Lett., 12, 2002, 1172-1173.
17. C. Fang, Y. Fan, J. M. Kong, Z.Q. Gao, N. Balasubramanian, Appl. Physics Letters, 92, 2008, 263108-1-3.

STUDIA UNIVERSITATIS BABEŞ-BOLYAI, PHYSICA, LIII, 1, 2008

FT – IR SPECTROSCOPIC STUDY OF $xAg_2O\cdot(100-x)[3B_2O_3\cdot As_2O_3]$ GLASS SYSTEM

S. C. BAIDOC[1], I. ARDELEAN[*]

ABSTRACT. Structural analysis of $xAg_2O(100-x)[3B_2O_3\cdot As_2O_3]$ glass system, with $0 \leq x \leq 10$ mol%, was performed by means of FT – IR spectroscopy. The purpose of this work is to investigate the structural changes that appear in the $3B_2O_3\cdot As_2O_3$ glass matrix with the addition and increasing of silver ions content. Pyro-, ortho-, di-, tri-, tetra-, penta-borate groups and structural units characteristic to As_2O_3 were found in the structure of the studied glasses. At small silver oxide content the predominant structural units are those in which boron is three-fold coordinated. For higher silver oxide concentrations ($x \geq 5$ mol%) the number of four-fold coordinated boron units is increasing. The changes in the $A_r = A_4/A_3$ (A_4 and A_3 reflect the relative amount of tetrahedral (BO_4 and $B\emptyset_4^-$) and triangular ($B\emptyset_3$ and $B\emptyset_2O^-$) borate species) ratio also shows the fact that silver oxide influence the boron coordination number.

Keywords. FT-IR spectroscopy, Structure, Glass systems

1. Introduction

B_2O_3 based glasses have been widely studied over the past decades due to their technological applications and for understanding the structural particularities as the occurrence of boron anomaly. Today, borates are important materials for insulation (glass wool) and textile (continuous filament) fiberglass [1]. Borate glasses are host of widespread optical, electrical, magnetic and other technologically interesting properties [2].

Pure boron oxide B_2O_3 in glass state consists of three coordinated boron atoms, which can be associated to form six-member boroxol rings [3].

As_2O_3 is also a network former in which we encounter AsO_3 pyramidal units and its glasses were identified as low loss materials for long distance optical transmission because of the exceptionally high transmission potential in the far infrared region [4, 5].

Silver borate glasses in particular have attracted a lot of attention because of their high ionic conductivity, especially when mixed with AgI. This property makes a basis for their applications in electrochemistry as solid electrolytes [6]. The optimization of such properties requires a good knowledge of the microscopic glass structure. In particular, a deeper knowledge of the local environment of the moving ions is highly desirable [7].

The purpose of this study is to investigate the structural changes which occur in $xAg_2O(100-x)[3B_2O_3\text{-}As_2O_3]$ glasses, with $0 \leq x \leq 10$ mol %, by means of FT – IR spectroscopy.

[1] *Corresponding author: codiab@yahoo.com*
[*] *Faculty of Physics, Babes-Bolyai University, 400084 Cluj Napoca, Romania*

2. Experimental

The $xAg_2O\cdot(100-x)[3B_2O_3\text{-}As_2O_3]$ glass system, with $0 \leq x \leq 10$ mol %, was prepared by mixing components of reagent grade purity as: $AgNO_3$, H_3BO_3 and As_2O_3. The mixtures were melted in sintered corundum crucibles, in an electric furnace directly at 1250 °C for 30 minutes. The melts were quickly cooled at room temperature by pouring onto stainless steel plates.

The FT-IR absorption spectra of the glasses in the 400 - 4000 cm^{-1} spectral range were obtained with an Equinox 55 Bruker spectrometer. Because the studied glasses presents IR absorption in the 400 – 2000 cm^{-1} spectral range, the spectra will be analyzed within this spectral range. The spectral resolution was about 0.5 cm^{-1}. The IR absorption measurements were done using the KBr pellet technique.

3. Results and discussion

The experimental FT – IR spectra of the $xAg_2O\cdot(100-x)[3B_2O_3\text{-}As_2O_3]$, with $0 \leq x \leq 10$ mol % glasses are presented in figure 1. The vibrational assignments of the bands for the glasses spectra were made using the method given by Condrate [8] and Tarte [9], by comparing the experimental data of glasses with those of related crystalline compounds.

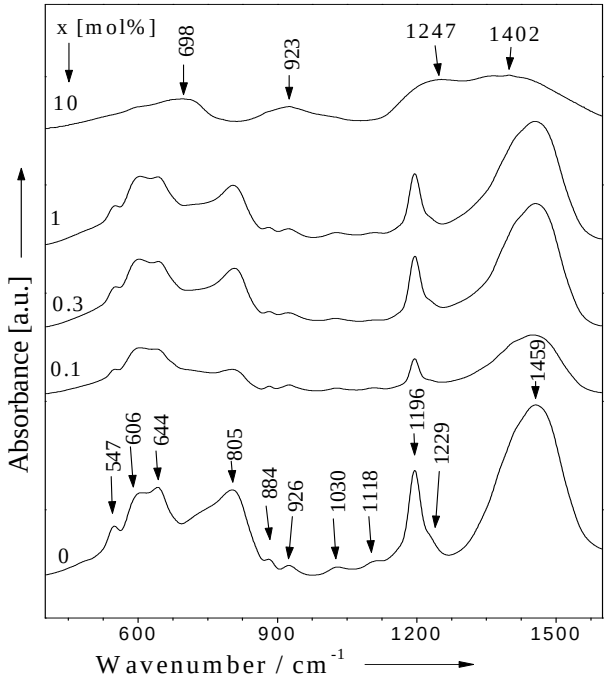

Fig.1. FT – IR spectra of $xAg_2O\cdot(1-x)[3B_2O_3\text{-}As_2O_3]$ glasses with $0 \leq x \leq 10$ mol %

In general, the IR absorptions of borate glasses occur in three regions:

- 600 - 800 cm^{-1} – due to B-O-B bending vibrations;
- 800 - 1150 cm^{-1} - due to boron in tetrahedral oxygen coordination (BO_4);
- 1200 -1500 cm^{-1} – due to borate units in which boron atom is coordinated with three oxygen (both bridging and nonbridging types) [10 - 13];

The glass matrix $3B_2O_3$-As_2O_3 presents the following FT - IR bands at: ~ 547 cm^{1}, ~ 606 cm^{-1}, ~ 644 cm^{-1}, ~ 805 cm^{-1}, ~ 884 cm^{-1}, ~ 926 cm^{-1}, ~ 1030 cm^{-1}, ~ 1118 cm^{-1}, ~ 1196 $cm^{-}1$, ~ 1229 cm^{-1} and ~ 1459 cm^{-1}. Their structural assignments are presented in Table 1.

In the first region there are three FT-IR bands. The band from ~ 547 cm^{-1} is assigned to B-O-B bonds bending vibrations involving oxygen atoms outside borate rings [14]. The band from ~ 606 cm^{-1} is due to symmetric bending vibrations of As – O bonds [4]. The band from ~ 644 cm^{-1} is assigned to O–B–O bonds bending vibrations. With the addition of 0.1 mol% Ag_2O, the intensities of these bands decrease, then increase with the increase of silver ions content up to 1 mol%. For the sample with x = 10 mol% it can be observed that these bands are covered by a broad band with a maximum at ~ 698 cm^{-1}.

In the second region there are five FT-IR bands. The band from ~ 805 cm^{-1} belongs to doubly degenerate stretching vibrations given by As-O bonds [4]. With the addition of 0.1 mol% Ag_2O, the intensity of the band is decreasing and, with the increase of silver oxide content its intensity is progressively increasing up to 1 mol%. For the sample with x = 10 mol%, it disappears. The bands from ~ 884 cm^{-1} and from ~ 926 cm^{-1} belongs to B-O bonds stretching vibrations in BO_4^- units from tri-, tetra- and penta-borate groups and B-O bonds stretching vibrations in BO_4 units from diborate groups, respectively. The band from ~ 1030 cm^{-1} is due to B-O bonds stretching vibrations in BO_4^- units from tri-, tetra- and penta-borate units and the band from ~ 1118 cm^{-1} is due to asymmetric stretching vibrations of B-O bonds from BO_4 units. With the increase of Ag_2O content, the bands from ~ 884 cm^{-1}, ~ 926 cm^{-1}, ~ 1030 cm^{-1} and ~ 1118 cm^{-1} remains approximately the same up to 1 mol %. For the sample with x = 10 mol%, these bands are covered by a broad band centered at ~ 923 cm^{-1}.

In the last region there are only three FT-IR bands. The first one, from ~ 1196 cm^{-1} is given by the asymmetric stretching vibrations of B-Ø and/or $B\text{-}O^-$ bonds in borate triangular units (BO_3 and BO_2O^-) from pyro- and ortho-borate groups. The second band, from ~ 1229 cm^{-1} is given by the asymmetric stretching vibrations of B-O bonds from orthoborate groups and the third band is due to B-O bonds stretching vibrations of BO_3 units from various borate groups. With the addition of 0.1 mol% of Ag_2O, the intensities of these bands are decreasing and, with the increase of silver oxide content, the intensities of the bands from ~ 1196 cm^{-1} and ~ 1459 cm^{-1} are progressively increasing up to 1 mol%. The shoulder from ~ 1229 cm^{-1} remains the same up to 1 mol%. For the sample with x = 10 mol% there are only two broad bands with maxima at ~ 1247 cm^{-1} and at ~ 1402 cm^{-1}, respectively.

Table 1.

Wavenumbers and band assignments of $xAg_2O\cdot(1-x)[3B_2O_3\text{-}As_2O_3]$ glasses

FT-IR assignments	
~ 547	B–O–B bonds bending vibrations involving oxygen atoms outside borate rings
~ 606	Symmetric bending vibrations of As – O bonds
~ 644	O–B–O bonds bending vibrations
~ 805	Doubly degenerate stretching vibrations of As-O bonds
~ 884 ~ 1030	B-O bonds stretching vibrations in BO_4^- units from tri-, tetra- and penta-borate groups
~ 926	B-O bonds stretching vibrations in BO_4 units from diborate groups
~ 1118	Asymmetric stretching vibrations of B-O bonds from BO_4 units
~ 1196	Asymmetric stretching vibrations of B-Ø and / or B-O^- bonds in borate triungular units (BO_3 and BO_2O^-) from pyro- and ortho-borate groups
~ 1229	Asymmetric stretching vibrations of B-O bonds from ortho-borate groups
~ 1459	B-O bonds stretching vibrations in BO_3 units from various borate groups

∅ - Oxygen atom bridging two boron atoms

The structure proposed for $3B_2O_3\text{-}As_2O_3$ glass matrix from FT-IR measurements is formed from tri- ($B_3O_5^-$), tetra- ($B_8O_{13}^{2-}$), penta- ($B_5O_8^-$), di- ($B_4O_7^{2-}$), pyro- ($B_2O_5^{4-}$) and ortho-borate (BO_3^{3-}) groups and from structural units characteristic to As_2O_3. With the addition of silver ions the proportion of these structural units is modified. The broadening of some bands with the increase of Ag_2O content is due to a depolymerization of the structure and an increasing of the disorder degree of studied glasses.

To quantify the silver ions effect to the changes in the relative population of triangular and tetrahedral borate units we have calculated the integrated intensity of the absorption envelopes 800-1150 cm^{-1} and 1200 - 1500 cm^{-1} denoted by A_4 and A_3 respectively [15]. A_4 and A_3 approximate the relative number of BO_4 and BO_3 units, respectively. The relative integrated intensity, $A_r = A_4/A_3$, is plotted in figure 2 versus Ag_2O content.

It can be observed that $A_r < 1$, which means that the predominant structural units in the studied glasses are BO_3 units. The increase of A_r ratio with the increase of silver ions content indicates a progressively change of boron coordination from three to four.

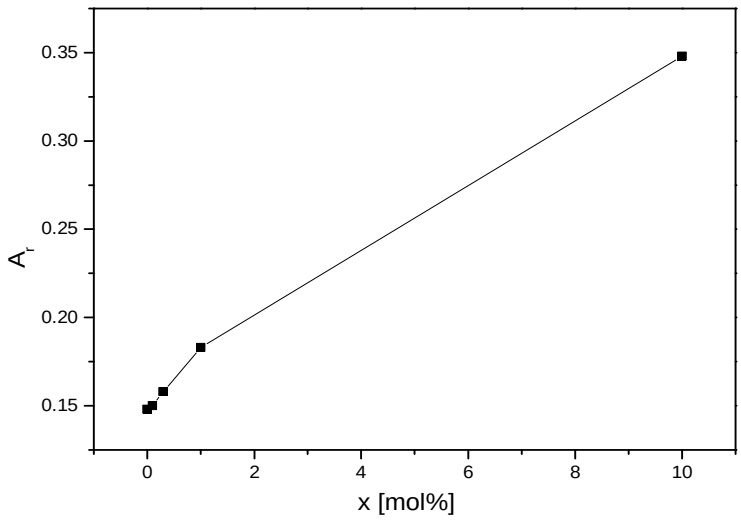

Fig. 2. A_r ratio as a function of Ag_2O content in $xAg_2O\cdot(100-x)[3B_2O_3\text{-}As_2O_3]$ glasses

4. Conclusions

From FT-IR spectra it can be observed that the network structure of $xAg_2O\cdot(1-x)[3B_2O_3\text{-}As_2O_3]$ glasses consist of randomly connected BO_3, BO_4 structural units and also from characteristic structural units of As_2O_3. The infrared measurements reveal the presence of borate structural units (di-, tri-, tetra-, penta-, pyro- and ortho- borate) and pyramidal units specific to As_2O_3. Boron atoms are present in the structure in both, three and four coordination states. The A_r ratio is lower than the unity, so the number of tetracoordinated boron atoms is smaller than the number of tricoordinated boron atoms. With the increasing of Ag_2O content, the boron-oxygen network is modifying by changing the coordination number of some of the boron atoms from three to four. The broadening of the FT-IR bands with the increase of Ag_2O content is due to a depolymerization of the structure and an increasing of the disorder degree.

REFERENCES

1. Ryiuichi Akagai, Norikazu Ohtori, Norimasa Umesaki, J. Non-Cryst. Solids 293, 471, (2001)
2. S.A. Feller, Phys. Chem. Glasses 41, 211, (2000)
3. M. Massot, S. Souto, M. Balkanski, J. Non-Cryst. Solids 182, 49, (1995)

4. G. Srinivisarao, N. Veeraiah, J. Alloys, Compounds 327, 52, (2001)
5. R. Ciceo Lucacel, I. Ardelean, J. Optoelectron. Adv. Mat. 8, (3), 1124, (2006)
6. T. Minami, J. Non-Cryst. Solids 73, 273, (1975)
7. G. Calas, L. Cormier, L. Galoisy, P. Jollivet, C.R. Acad. Sci., Ser. IIc: Chim. 5, 831, (2002)
8. R. A. Condrate, J. Non-Cryst. Solids 84, 26 (1986)
9. P. Tarte, Physics of Non Crystalline Solids 549 (1964)
10. U. Selvara, K. J. Rao, Spectrochim. Acta A, 40, 1081 (1984)
11. E. I. Kamitsos, M. A. Karakassides, G. D. Chryssikos, Phys. Chem. Glasses 28, 203 (1987)
12. E. I. Kamitsos, M. A. Karakassides, G. D. Chryssikos, J. Phys. Chem. 91, 1073 (1987)
13. E. I. Kamitsos, A. P. Patsis, M. A. Karakassides, G. D. Chryssikos, J. Non-Cryst. Solids 126, 52 (1990)
14. J. F. Ducel, J. J. Videau, M. Couzi, Phys. Chem. Glasses 34, 5 (1993)
15. Y. D. Yiannopoulos, G. D. Chryssikos, E. I. Kamitsos, Phys. Chem. Glasses 42, 164 (2001)